Università degli Studi di Padova

Dipartimento di Fisica e Astronomia Galileo Galilei
Università degli Studi di Padova

Department of Physics and Astronomy "Galileo Galilei"
Master Thesis in Physics

# Commissioning and first data analysis of the JUNO detector


Master Candidate

**Lorenzo Vincenzo D'Auria**

**Student ID 2122147**

Supervisor

**Dr. Andrea Serafini**

**University of Padova**

Co-supervisor

**Prof. Alberto Garfagnini**

**University of Padova**


Academic Year
2024/2025

**Abstract**

Neutrinos, among the most abundant yet elusive constituents of the Standard Model (SM) of particle physics, were postulated by Pauli in 1930 to preserve energy conservation in beta decay. Although massless in the original SM formulation, the experimentally observed phenomenon of neutrino oscillations—the periodic transformation among neutrino flavors during propagation—requires that neutrinos have mass and that flavor eigenstates ($\nu_e, \nu_\mu, \nu_\tau$) are non-trivial superpositions of mass eigenstates ($\nu_1, \nu_2, \nu_3$). This mixing is described by the Pontecorvo-Maki-Nakagawa-Sakata (PMNS) matrix and governed by three mixing angles ($\theta_{12}, \theta_{23}, \theta_{13}$), two mass-squared differences ($\Delta m^2_{21}, \Delta m^2_{31}$), and a CP-violating phase $\delta_{CP}$. Oscillation experiments have conclusively demonstrated that at least two neutrino mass eigenstates are non-zero and that $m_1 < m_2$. However, a key question remains unanswered: whether the mass hierarchy follows the Normal Ordering (NO), $m_1 < m_2 < m_3$, or the Inverted Ordering (IO), $m_3 < m_1 < m_2$.

Jiangmen Underground Neutrino Observatory (JUNO) is a multipurpose experiment designed to unveil fundamental neutrino properties, explore their astrophysical and terrestrial origins, and search for physics beyond the SM. Its Central Detector (CD) comprises 20 kilotons of Liquid Scintillator (LS), enclosed in a 35-meter-diameter acrylic sphere supported by 591 stainless steel rods and located 680 meters underground in Guangdong, China. The scintillator is optically monitored by 17,612 20-inch and 25,600 3-inch Photomultiplier Tubes (PMT), forming the Large-PMT (LPMT) and Small-PMT (sPMT) systems, and is submerged in instrumented ultra-pure Water Pool (WP) for shielding froom external radiation and muon veto purposes. In December 2024, JUNO has entered the commissioning phase and begun filling the CD—initially with water, which is gradually being replaced with LS. Located 53 km from the Yangjiang and Taishan nuclear power plants, JUNO is optimized for determining the Neutrino Mass Ordering (NMO) by detecting reactor $\bar{\nu}_e$ via the Inverse Beta Decay (IBD) reaction:

$$\bar{\nu}_e + p \rightarrow e^+ + n$$

The positron deposits its energy in the LS and annihilates into two 0.511 MeV photons, producing a prompt signal. The neutron is then captured on hydrogen or carbon, emitting a delayed gamma of 2.22 or 4.95 MeV, respectively. This correlation serves as an experimental handle that, if properly exploited, allows the isolation of these rare events from the overwhelming background. JUNO expects to record approximately 60 IBD events per day. To achieve its ambitious physics goals, JUNO requires both sufficient statistics and excellent energy resolution.

The first requirement, given a fixed exposure, is intrinsically linked to the ability to effectively select IBD candidate events. This thesis focuses on the development of an event selection algorithm capable of identifying temporally and spatially correlated events of various types with high efficiency and purity (presented in Chapter 4). The algorithm has been validated and used to conduct two parallel analyses: one on the radiopurity of the LS, and another on spallation neutrons. The monitor of radiopurity is crucial during the filling phase: It is challenging to quantitatively demonstrate that the LS can be purified to the extremely low levels required by the collaboration's radiopurity goals - namely,

the concentration of U/Th has to be below $1 \cdot 10^{-15}$ g/g for reactor neutrino studies and $1 \cdot 10^{-17}$ g/g for solar neutrino studies - solely based on the specifications of the purification systems; so the only viable approach is to monitor the radiopurity before and during the injection of LS into the CD using real data. A fast coincidence, experimentally and topologically very similar to an IBD event, between the $\beta$-decay of $^{214}$Bi and the subsequent $\alpha$-decay of $^{214}$Po was tagged using the developed algorithm, enabling hourly monitoring of $^{222}$Rn contamination and extraction of the $^{238}$U contamination level, which was found to be compatible with the collaboration's requirements.

The second key requirement for JUNO is its unprecedented energy resolution: $3\%$ at 1 MeV. This resolution depends on several parameters. From a calibration perspective, one of the most critical factors is the spatial variation in detector response—i.e., non-uniformity in terms of Photoelectron (PE) produced per MeV of deposited energy across different detector locations. The second part of this thesis addresses the study of such non-uniformity (Chapter 5). Using the previously selected spallation neutrons as a uniform, stable, and homogeneous calibration source throughout the detector, a vertex reconstruction algorithm was developed based on the timing response of the 17,612 LPMT. The timing behavior of the detector was studied (Chapter 3) in the context of the ongoing laser calibration campaigns during the commissioning phase. The temporal response of the PMT was parametrized, and a parallel analysis was carried out on the time synchronization procedures of the readout electronics. A numerical Time of Flight (ToF) map was constructed, accounting for optical path distortions due to refraction effects in the current hybrid water-LS configuration. Together, these elements enabled the modeling of the detector's temporal response, the construction of a time-based likelihood, and its application for interaction vertex estimation. Thanks to this reconstruction algorithm, combined with the event selection for spallation neutron tagging, a non-uniformity correction map was produced, improving the energy resolution by approximately $40\%$.

**Sommario**

I neutrini, tra i costituenti più abbondanti ma sfuggenti del Modello Standard (SM) della fisica delle particelle, furono ipotizzati da Pauli nel 1930 per garantire la conservazione dell'energia nel decadimento beta. Sebbene privi di massa nella formulazione originaria dello SM, l'osservazione sperimentale del fenomeno delle oscillazioni dei neutrini—ovvero la trasformazione periodica tra sapori durante la propagazione—richiede che i neutrini abbiano massa e che gli autostati di sapore ($\nu_e, \nu_\mu, \nu_\tau$) siano combinazioni non banali degli autostati di massa ($\nu_1, \nu_2, \nu_3$). Questo mescolamento è descritto dalla matrice di Pontecorvo–Maki–Nakagawa–Sakata (PMNS) ed è regolato da tre angoli di mescolamento ($\theta_{12}, \theta_{23}, \theta_{13}$), due differenze di massa al quadrato ($\Delta m^2_{21}, \Delta m^2_{31}$) e una fase di violazione di CP $\delta_{CP}$. Gli esperimenti di oscillazione hanno dimostrato che almeno due autostati di massa hanno massa diversa da zero e che $m_1 < m_2$. Tuttavia, rimane aperta una questione fondamentale: se la gerarchia delle masse segua lo schema normale (NO), $m_1 < m_2 < m_3$, oppure quello inverso (IO), $m_3 < m_1 < m_2$.

JUNO è un esperimento multifunzionale progettato per indagare le proprietà fondamentali dei neutrini, esplorarne le origini astrofisiche e terrestri e cercare segnali di fisica oltre lo SM. Il suo rivelatore centrale (CD) contiene 20 kiloton di scintillatore liquido (LS), racchiuso in una sfera acrilica del diametro di 35 metri, sorretta da 591 aste in acciaio inossidabile e situata a 680 metri di profondità nella provincia di Guangdong, in Cina. Lo scintillatore è monitorato otticamente da 17 612 fotomoltiplicatori da 20 pollici e 25 600 da 3 pollici (PMT), che costituiscono i sistemi LPMT e sPMT, ed è immerso in acqua ultrapura strumentata (WP) per lo schermaggio dalle radiazioni esterne e il veto dei muoni. Da dicembre 2024 JUNO è entrato nella fase di commissioning iniziando il riempimento del CD—inizialmente con acqua, progressivamente sostituita da LS. Situato a 53 km dalle centrali nucleari di Yangjiang e Taishan, JUNO è ottimizzato per determinare l'ordinamento delle masse dei neutrini (NMO) mediante la rivelazione di $\bar{\nu}_e$ da reattore attraverso la reazione di Inverse Beta Decay (IBD):

$$\bar{\nu}_e + p \rightarrow e^+ + n$$

Dove il positrone deposita la propria energia nel LS e si annichila in due fotoni da 0,511 MeV, producendo un segnale "prompt". Il neutrone viene successivamente catturato su idrogeno o carbonio, emettendo un gamma ritardato da 2,22 o 4,95 MeV rispettivamente. Questa correlazione rappresenta una caratteristica sperimentale che, se opportunamente sfruttata, consente di isolare questi eventi rari dal fondo predominante. JUNO prevede di registrare circa 60 eventi IBD al giorno. Per raggiungere i suoi ambiziosi obiettivi scientifici, JUNO richiede sia sufficiente statistica che un'eccellente risoluzione in energia.

Il primo requisito, a parità di esposizione, è legato alla capacità di selezionare efficacemente i candidati IBD. Questa tesi si concentra sullo sviluppo di un algoritmo di selezione eventi in grado di identificare con alta efficienza e purezza eventi spazialmente e temporalmente correlati di vario tipo (presentato nel Capitolo 4). L'algoritmo è stato validato e impiegato per due analisi parallele: una sulla radiopurezza dello LS e un'altra sui neutroni da spallazione. Il monitoraggio della radiopurezza è cruciale

durante la fase di riempimento: è infatti difficile dimostrare quantitativamente che il LS possa essere purificato ai livelli estremamente bassi richiesti dagli obiettivi della collaborazione—ossia concentrazioni di U/Th inferiori a $1 \cdot 10^{-15}$ g/g per gli studi sui neutrini da reattore e $1 \cdot 10^{-17}$ g/g per quelli solari—basandosi esclusivamente sulle specifiche dei sistemi di purificazione; di conseguenza, l'unica strategia efficace è monitorare la radiopurezza prima e durante l'iniezione dello LS nel CD utilizzando dati reali. Una coincidenza rapida, sperimentalmente e topologicamente molto simile a un evento IBD, tra il decadimento $\beta$ del $^{214}$Bi e il successivo decadimento $\alpha$ del $^{214}$Po è stata identificata tramite l'algoritmo sviluppato, permettendo un monitoraggio orario della contaminazione da $^{222}$Rn e l'estrazione del livello di contaminazione da $^{238}$U, risultato compatibile con i requisiti imposti dalla collaborazione.

Il secondo requisito chiave per JUNO è la sua risoluzione energetica senza precedenti: $3\%$ a 1 MeV. Tale risoluzione dipende da diversi parametri. Da un punto di vista della calibrazione, uno dei fattori più critici è la variazione spaziale della risposta del rivelatore—cioè la non uniformità in termini di fotoelettroni (PE) prodotti per MeV di energia depositata in diverse regioni del rivelatore. La seconda parte di questa tesi è dedicata allo studio di tale non uniformità (Capitolo 5). Utilizzando i neutroni da spallazione precedentemente selezionati come sorgente di calibrazione uniforme, stabile e omogenea all'interno del rivelatore, è stato sviluppato un algoritmo di ricostruzione del vertice basato sulla risposta temporale dei 17 612 LPMT. Il comportamento temporale del rivelatore è stato analizzato (Capitolo 3) nel contesto delle attuali campagne di calibrazione laser durante il commissioning. È stata effettuata una parametrizzazione della risposta temporale dei PMT, ed è stata condotta un'analisi parallela sui meccanismi di sincronizzazione temporale dell'elettronica di readout. È stata costruita una mappa numerica dei tempi di volo (ToF), tenendo conto delle distorsioni ottiche dovute alla rifrazione nella configurazione attuale ibrida acqua-LS. Questi elementi hanno permesso la modellizzazione della risposta temporale del rivelatore, la costruzione di una likelihood basata sul tempo e la sua applicazione per la stima del vertice d'interazione. Grazie a questo algoritmo di ricostruzione, combinato con la selezione degli eventi per il tagging dei neutroni di spallazione, è stata prodotta una mappa di correzione della non uniformità, che ha portato a un miglioramento della risoluzione in energia di circa il $40\%$.

# Contents


**1 Neutrino Physics** **1**

1.1 Neutrinos in the Standard Model . . . 2

1.2 Neutrino oscillations . . . 4

1.2.1 Oscillation in vacuum . . . 4

1.2.2 NMO problem . . . 6

1.2.3 Experiment at reactors . . . 6

**2 The JUNO Experiment** **9**

2.1 JUNO Location . . . 10

2.2 Detector Design . . . 11

2.2.1 The LS purification system . . . 12

2.2.2 Photon Detection System . . . 14

2.2.3 Readout Electronics . . . 15

2.2.4 Calibration System . . . 17

2.3 JUNO Physics Goals and current status . . . 19

2.3.1 NMO Strategy and sensitivity . . . 21

2.3.2 JUNO status . . . 22

**3 Electronics synchronization studies** **23**

3.1 JUNO synchronization system . . . 24

3.2 Transit Time computation . . . 27

3.2.1 Hit Time Extraction Methodology . . . 27

3.2.2 ToF map . . . 30

3.2.3 Reference time ($t_0$) extraction and JUNO laser system . . . 35

3.3 PMT timing model and synchronization performances . . . 37

3.3.1 Synchronization performances . . . 39

**4 Event Selection and radiopurity monitoring** **41**

4.1 Expected signal and background in JUNO . . . 42

4.1.1 Signal and backgrounds in JUNO . . . 42

4.1.2 Natural Radioactivity . . . 45

4.2 Event selection algorithm and LS Radiopurity Monitoring . . . 46

4.2.1 Correlation Studies with the Off-Window Technique . . . 48
4.2.2 Radiopurity Monitoring in JUNO . . . 51
4.3 Application of event selection algorithm: Spallation neutrons . . . 56

**5 Energy Resolution** **59**
5.1 Detector Energy Response . . . 60
5.1.1 Energy Resolution and Non-Uniformity . . . 61
5.2 Vertex reconstruction algorithm . . . 63
5.2.1 Charge vertex reconstruction . . . 63
5.2.2 Time vertex reconstruction . . . 65
5.2.3 Algorithm performances . . . 68
5.3 Energy Non-Uniformity Map and Energy Resolution Improvement . . . 71

**6 Conclusions** **75**

**A Detailed IBD kinematics and cross section** **77**

**B Solar neutrinos detection in JUNO** **81**

**C Radioactive decay** **85**

**List of Acronyms** **89**

**List of Figures** **93**

**List of Tables** **99**

**References** **101**

# 1

# Neutrino Physics

Neutrinos are among the most abundant particles in the Universe, yet they remain some of the most elusive within the framework of the Standard Model (SM) of particle physics. First postulated by Pauli in 1930 to account for energy conservation in beta decay, neutrinos were originally considered massless in the SM. However, the discovery of neutrino oscillations—the periodic change of neutrino flavor states during propagation—provides clear evidence that neutrinos have non-zero masses and that flavor eigenstates ($\nu_e, \nu_\mu, \nu_\tau$) are non-trivial linear combinations of mass eigenstates ($\nu_1, \nu_2, \nu_3$). This phenomenon is described by the Pontecorvo-Maki-Nakagawa-Sakata (PMNS) matrix and is characterized by three mixing angles ($\theta_{12}, \theta_{23}, \theta_{13}$), two independent mass-squared differences ($\Delta m^2_{21}, \Delta m^2_{31}$), and a CP-violating phase $\delta_{CP}$. Oscillation experiments have definitively shown that at least two neutrino mass eigenstates have non-zero mass and that $m_1 < m_2$. Nevertheless, an open question remains: whether the mass hierarchy follows the Normal Ordering (NO), $m_1 < m_2 < m_3$, or the Inverted Ordering (IO), $m_3 < m_1 < m_2$.

This chapter begins with a brief overview of neutrinos in the context of the SM, followed by a discussion of the problem of neutrino mass and the theoretical models proposed to explain its origin (Section 1.1). The concept of flavor mixing will then be introduced, focusing on the phenomenon of oscillations in the three-flavor framework (Section 1.2.1). The issue of the Neutrino Mass Ordering (NMO) will be addressed, along with the experimental determination of oscillation parameters using reactor-based neutrino experiments (Sections 1.2.2 and 1.2.3). The chapter concludes with an overview of the main physics goals of Jiangmen Underground Neutrino Observatory (JUNO), a 20 kton multi-purpose underground Liquid Scintillator (LS) detector located in southern China, which is the primary subject of this thesis.

## 1.1 Neutrinos in the Standard Model

In the SM [1], neutrinos are fermions that do not have strong nor electromagnetic interactions. Consequently, they are singlets of the subgroup $\mathrm{SU(3)_C} \times \mathrm{U(1)_{EM}}$. They are part of the lepton doublets $L_l = \begin{pmatrix} \nu_l \\ l \end{pmatrix}_L$ where $f_L$ is the left-handed component of the fermion $f$, $f_L = P_L f \equiv \frac{1-\gamma^5}{2} f$. In the SM there is one active neutrino for each charged lepton, $l = e, \mu, \tau$. $\mathrm{SU(2)_L}$ gauge invariance dictates the form of weak Charged Current (CC) interactions between the neutrinos and their corresponding charged leptons and Neutral Current (NC) interactions among themselves to be:

$$-\mathcal{L}_{CC} = \frac{g}{\sqrt{2}} \sum_l \bar{\nu}_{Ll} \gamma^\mu l_L^- W_\mu^+ + h.c. \tag{1.1}$$

$$-\mathcal{L}_{NC} = \frac{g}{2cos\theta_W} \sum_l \bar{\nu}_{Ll} \gamma^\mu \nu_{Ll} Z_\mu^0 \tag{1.2}$$

In the above equations, $g$ is the coupling constant associated with SU(2) and $\theta_W$ is the Weinberg angle. Equations 1.1 and 1.2 describe all the neutrino interactions in the SM.

### The problem of mass

In the SM, the masses of the fermions are generated via a Yukawa coupling of the scalar Higgs doublet $\phi$ with a fermion right-handed and left-handed component. The former is an $\mathrm{SU(2)_L}$ singlet, the latter is part of a doublet. For leptons, we can build such a term coupling the left-handed lepton doublets $L_L$ with the right-handed charged lepton fields $E_R$:

$$-\mathcal{L}_{Yukawa,lep} = Y_{ij}^l \bar{L}_{Li} \phi E_{Rj} + h.c. \tag{1.3}$$

After spontaneous symmetry breaking these terms lead to charged lepton masses:

$$m_{ij}^l = Y_{ij}^l \frac{v}{\sqrt{2}} \tag{1.4}$$

where $v$ is the vacuum expectation value of the Higgs field. However, since the model does not contain right-handed neutrinos, no such Yukawa interaction can be built for the neutrinos, which are consequently massless at the Lagrangian level. In principle, a neutrino mass term could be generated at loop level. With the particle content of the SM the only possible neutrino mass term that could be constructed is the bilinear $\overline{L_L} L_L^c$, where $L^c = C\overline{L}^T$ and $C$ is the charge conjugation matrix. However, this term is forbidden in the SM because it violates the total lepton number symmetry by two units and therefore it cannot be induced by loop corrections, as it breaks the accidental symmetry of the model. We conclude that it is not possible to construct a renormalizable mass term for the neutrinos with the fermionic content and gauge symmetry of the SM. The obvious consequence is that in order to introduce a neutrino mass in the theory one must extend the particle content of the model.

The first attempt is to generate a Dirac mass term by introducing a $\nu_R$. In the mass basis we obtain:

$$-\mathcal{L}_Y^l = \bar{L}_L \tilde{\phi} y_\nu \nu_R + h.c. \tag{1.5}$$

where $\tilde{\phi} = i\sigma_2 \phi^*$ and $\nu_R$ is sterile under $\mathrm{SU(2)_L} \otimes \mathrm{U(1)_Y}$ since the term $L_L \tilde{\phi}$ transforms as $(1, 0)$. The experimental bounds on the neutrino masses translate into a bound on the neutrino Yukawa coupling:

$$m_\nu \leq 0.1eV \Longrightarrow y_\nu \leq 10^{-12} \tag{1.6}$$

which is exceedingly small, especially when compared to the top Yukawa coupling $y_t \simeq 1$. This naturalness problem calls for a dynamical mechanism accounting for such small neutrino masses.
The seesaw mechanism introduces a heavy right-handed Majorana neutrino $N_R$, which is totally sterile under the SM gauge group $G_{\mathrm{SM}}$. The most general Lagrangian invariant under $G_{\mathrm{SM}}$ is:

$$-\mathcal{L}_{see-saw} = \bar{L}_L \tilde{\phi} y_\nu N_R + M_R \bar{N}_R^c N_R + h.c. = \begin{pmatrix} \bar{\chi} & \bar{\omega} \end{pmatrix} \cdot \begin{pmatrix} 0 & \frac{v y_\nu}{2\sqrt{2}} \\ \frac{v y_\nu}{2\sqrt{2}} & M_R \end{pmatrix} \cdot \begin{pmatrix} \chi \\ \omega \end{pmatrix} \tag{1.7}$$

Since we assume the right-handed neutrino to lie at the Grand Unification scale ($M_R \sim 10^{15}$ GeV), we end up with the following mass eigenstates and mass spectrum:

$$\begin{cases} \eta_1 \approx \chi = \nu_L + \nu_L^c \\ \eta_2 \approx \omega = N_R + N_R^c \end{cases} \Longrightarrow \begin{cases} m_1 \approx \frac{(v y_\nu)^2}{8 M_R} \\ m_2 \approx M_R \end{cases} \tag{1.8}$$

where we assumed the limit $v y_\nu \ll M_R$. We see that the seesaw mechanism provides a way to dynamically suppress the $\nu_L$ mass without assuming any unnatural value of the Yukawa coupling $y_\nu$.

### The PMNS matrix

Irrespectively of the nature of neutrino masses, flavor mixing effects in the leptonic sector appear, in the lepton mass basis, in charged-current interactions:

$$\mathcal{L}_{CC}^l = -\frac{g}{\sqrt{2}} \left( \bar{\nu}_L U \gamma^\mu W_\mu^+ e_L + \bar{e}_L U^\dagger W_\mu^- \gamma^\mu \nu_L \right) \tag{1.9}$$

Concerning the parametrization of the $U$ matrix, we can write:

$$U = \begin{pmatrix} 1 & 0 & 0 \\ 0 & c_{23} & s_{23} \\ 0 & -s_{23} & c_{23} \end{pmatrix} \cdot \begin{pmatrix} c_{13} & 0 & s_{13} e^{-i\delta_{CP}} \\ 0 & 1 & 0 \\ -s_{13} e^{i\delta_{CP}} & 0 & c_{13} \end{pmatrix} \cdot \begin{pmatrix} c_{12} & s_{12} & 0 \\ -s_{12} & c_{12} & 0 \\ 0 & 0 & 1 \end{pmatrix} \cdot \begin{pmatrix} e^{i\eta_1} & 0 & 0 \\ 0 & e^{i\eta_2} & 0 \\ 0 & 0 & 1 \end{pmatrix} \tag{1.10}$$

where $c_{ij} \equiv \cos\theta_{ij}$ and $s_{ij} \equiv \sin\theta_{ij}$. The angles $\theta_{ij}$ can be taken without loss of generality to lie in the first quadrant, $\theta_{ij} \in [0, \pi/2]$, and the phases $\delta_{\mathrm{CP}}$ (CP-violating phase), $\eta_i$ (Majorana phases) $\in [0, 2\pi]$. In case of three Dirac neutrinos, the Majorana phases $\eta_1$ and $\eta_2$ can be absorbed in the neutrino states, so the number of physical phases is one (similar to the Cabibbo-Kobayashi-Maskawa (CKM) matrix).

Thus we can write $U$ as:

$$U_{PMNS} = \begin{pmatrix} c_{12}c_{13} & s_{12}c_{13} & s_{13}e^{-i\delta_{CP}} \\ -s_{12}c_{23} - c_{12}s_{13}s_{23}e^{i\delta_{CP}} & c_{12}c_{23} - s_{12}s_{13}s_{23}e^{i\delta_{CP}} & c_{13}s_{23} \\ s_{12}s_{23} - c_{12}s_{13}c_{23}e^{i\delta_{CP}} & -c_{12}s_{23} - s_{12}s_{13}c_{23}e^{i\delta_{CP}} & c_{13}c_{23} \end{pmatrix} \tag{1.11}$$

This matrix is often called the PMNS mixing matrix.

## 1.2 Neutrino oscillations

If neutrinos have masses and lepton flavours are mixed in the weak CC interactions, lepton flavour is not conserved in neutrino propagation [2] [3]. This phenomenon is usually referred to as neutrino oscillations.

### 1.2.1 Oscillation in vacuum

Let us consider a source of neutrinos, which are always produced in a flavor eigenstate $\nu_\alpha$. After traveling for a distance $L$, neutrinos interact with a detector where their flavor is probed by means of another CC process involving a charged lepton of defined flavor.

We can distinguish two different kinds of neutrino oscillation experiments:

- $\alpha \neq \beta$ (Appearance experiments): These experiments measure transitions between different neutrino flavors.
- $\alpha = \beta$ (Disappearance experiments): These experiments measure the survival probability of a neutrino flavor by counting the number of interactions in the detector and comparing it with the expected one.

Let $\nu_i$ be mass eigenstates and $\nu_\alpha$ flavor eigenstates. Neutrinos are produced through CC interactions in a given flavor eigenstate that is the superposition of different mass eigenstates:

$$|\nu_\alpha\rangle = \sum_i U_{\alpha i}|\nu_i\rangle. \tag{1.12}$$

We define the oscillation probability as the following quantity:

$$P_{\alpha\beta}(t) = |\langle \nu_\alpha(0)|\nu_\beta(t)\rangle|^2, \tag{1.13}$$

that is, the probability of detecting at time $t$ a neutrino of flavor $\beta$ if at time $t = 0$ such a neutrino was of flavor $\alpha$. From now on, we will assume that neutrinos are ultrarelativistic (which is always an excellent approximation in the considered scenarios), and we will identify the distance between source and detector $L$ with the time of flight $t$ (we assume natural units where $c = 1$). We now want to compute an explicit relation for the 1.13 in the case of $N = 3$ generation of neutrinos.

Consider two flavors $l$ and $l'$, then

$$|\nu_l(0)\rangle = \sum_{i=1}^{3} U_{li}|\nu_i(0)\rangle \Longrightarrow |\nu_l(t)\rangle = \sum_{i=1}^{3} e^{-iE_i t} U_{li}|\nu_i(0)\rangle \tag{1.14}$$

Using the fact that

$$E_i = \sqrt{p^2 + m_i^2} = p\sqrt{1 + \frac{m_i^2}{p^2}} \approx p + \frac{m_i^2}{2p} \approx E + \frac{m_i^2}{2E} \tag{1.15}$$

The oscillation probability 1.13 is given by

$$\begin{aligned} P(\nu_l \to \nu_{l'}) &= \left|\langle \nu_{l'}(0)|\nu_l(t)\rangle\right|^2 = \left|\sum_{i=1}^{3} e^{-iE_i t} U^*_{l'i} U_{li}\right|^2 = \left|\sum_{i=1}^{3} e^{-iEL} e^{-i\frac{m_i}{2E}L} U^*_{l'i} U_{li}\right|^2 = \\ &= \left|\sum_{i=1}^{3} e^{-i\frac{m_i}{2E}L} U^*_{l'i} U_{li}\right|^2 = \sum_{i,k} U^*_{l'i} U_{li} U_{l'k} U^*_{lk} e^{-i\frac{\Delta m^2_{ik} L}{2E}} = \\ &= \sum_{i=k} |Ul'i|^2 |U_{li}|^2 + 2Re\left[\sum_{i>k} U^*_{l'i} U_{l'k} U_{li} U^*_{lk}\right] \end{aligned} \tag{1.16}$$

where in the last equality we have decomposed the sum with $i \neq k$ into two sums that are complex conjugate of each other (one with $i > k$ for which $\Delta m^2_{ki} > 0$ and the other with $i < k$ for which $\Delta m^2 < 0$), and then we used the property $z + z^* = 2\mathrm{Re}(z)$. Now we exploit the identities

$$\sum_{i,k} U^*_{l'i} U_{li} U_{l'k} U^*_{lk} = \begin{cases} \sum_{i=k} |U_{l'i}|^2 |U_{li}|^2 + 2Re\left\{\sum_{i>k} U^*_{l'i} U_{li} U_{l'k} U^*_{lk}\right\} \\ \left(\sum_i U^*_{l'i} U_{li}\right)\left(\sum_k U_{l'k} U^*_{lk}\right) = \delta_{ll'}\delta_{l'l} = \delta_{l'l} \end{cases} \tag{1.17}$$

where we used that $\sum_i U^*_{l'i} U_{li} = \delta_{ll'}$. Substituting Eq. 1.17 into Eq. 1.16, we find

$$\begin{aligned} P(\nu_l \to \nu_{l'}) &= \delta_{l'l} - 2\,\mathrm{Re}\left\{\sum_{i>k} U^*_{l'i} U_{li} U_{l'k} U^*_{lk}\left(1 - e^{-i\frac{\Delta m^2_{ki} L}{2E}}\right)\right\} = \\ &= \delta_{l'l} - 2\,\mathrm{Re}\left\{\sum_{i>k} U^*_{l'i} U_{li} U_{l'k} U^*_{lk}\left(1 - \cos\left(\frac{\Delta m^2_{ki} L}{2E}\right)\right)\right\} + 2\,\mathrm{Im}\left\{\sum_{i>k} U^*_{l'i} U_{li} U_{l'k} U^*_{lk} \cdot \sin\left(\frac{\Delta m^2_{ki} L}{2E}\right)\right\} \end{aligned}$$

where we exploited the identity $\mathrm{Re}(ab) = \mathrm{Re}(a)\mathrm{Re}(b) - \mathrm{Im}(a)\mathrm{Im}(b)$. Finally,

$$P(\nu_l \to \nu_{l'}) = \delta_{l'l} - 4\,\mathrm{Re}\left\{\sum_{i>k} U^*_{l'i} U_{li} U_{l'k} U^*_{lk}\right\} \cdot \sin^2\left(\frac{\Delta m^2_{ki} L}{4E}\right) + 2\,\mathrm{Im}\left\{\sum_{i>k} U^*_{l'i} U_{li} U_{l'k} U^*_{lk} \cdot \sin\left(\frac{\Delta m^2_{ki} L}{2E}\right)\right\} \tag{1.18}$$

### 1.2.2 NMO PROBLEM

As we can observe from Eq. 1.18, neutrino oscillation physics is only sensitive to the squared mass differences ($\Delta m^2_{ij} = m^2_i - m^2_j$). Historically, $\Delta m^2_{21}$ and $\Delta m^2_{31}$ are referred to as the solar and atmospheric mass splittings, respectively. Current oscillation data can be remarkably well-fitted in terms of two squared mass differences, dubbed as the solar mass splitting ($\Delta m^2_{21} \simeq 7.6 \times 10^{-5}$ eV$^2$) and the atmospheric mass splitting ($|\Delta m^2_{31}| \simeq 2.5 \times 10^{-3}$ eV$^2$) [4]. Thanks to matter effects in the Sun, we know that $\Delta m^2_{21} > 0$ [5]. Since in Eq. 1.18 the terms $\Delta m^2_{31}$ and $\Delta m^2_{32}$ appear only in even functions (i.e., $\sin^2(\Delta m^2)$), the probability is insensitive to the sign of $\Delta m^2_{31}$ (or $\Delta m^2_{32}$), which is therefore currently unknown. As a consequence, we have two possibilities for the NMO (shown in Fig. 1.1):

- **NO**: $\Delta m^2_{31} > 0$, then $m_1 < m_2 << m_3$
- **IO**: $\Delta m^2_{31} < 0$, then $m_3 << m_1 < m_2$

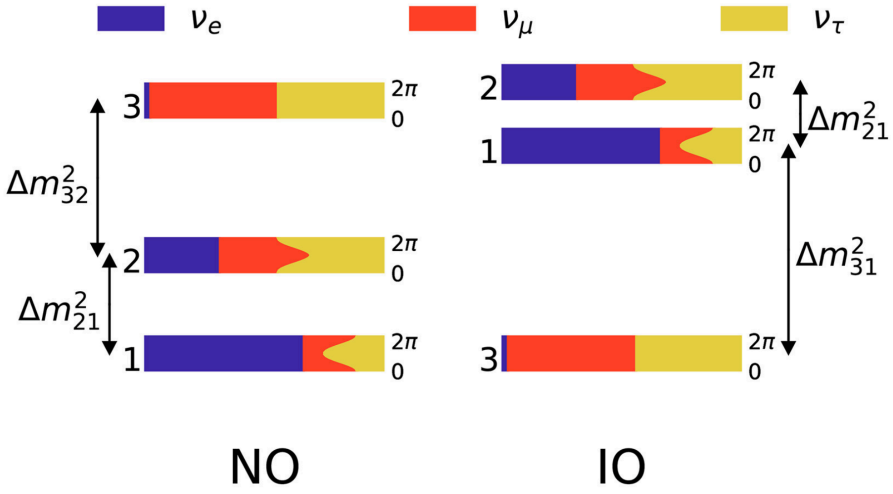


***Figure 1.1:*** *The two possible hierarchical neutrino mass scenarios with graphical representation of the neutrino flavor content of each of the neutrino mass eigenstates given the current preferred values of the oscillation parameters [4]. The precise value of the CP-violating phase in the leptonic sector remains unknown; consequently, it is varied $\delta$ within its entire CP range, ranging from 0 to $2\pi$. Inspired by [6].*

### 1.2.3 EXPERIMENT AT REACTORS

Nuclear reactors are very intense sources of $\bar{\nu}_e$'s in the MeV energy region, which are generated in nuclear fission of heavy isotopes (mainly $^{235}$U, $^{238}$U, $^{239}$Pu, and $^{241}$Pu) [1]. The $\bar{\nu}_e$ flux from a reactor can be estimated based on the thermal power output and fuel composition as a function of time. On average, about six $\bar{\nu}_e$'s are emitted, and about 200 MeV of energy is released per fission. Therefore, a 1 GW$_{\text{th}}$ reactor produces about $2 \times 10^{20}$ $\bar{\nu}_e$/s. The detailed estimate of $\bar{\nu}_e$ flux and energy spectrum can be obtained by either summing up the spectra of beta decays involved using available nuclear data information of each fission fragment and its decays, or by using measurements of cumulative electron spectra associated with the beta decays of fission fragments. Because the fission of four main fuel isotopes involves thousands of beta-decay branches, a complete *ab initio* calculation is challenging.

CC interaction cannot happen if a reactor $\bar{\nu}_e$ changes its flavour to $\bar{\nu}_\mu$ or $\bar{\nu}_\tau$, because its energy (on the order of $\approx$ 10 MeV) is not sufficient to produce heavier charged leptons. Thus, $\bar{\nu}_e$ disappearance is the only channel to study neutrino flavour change with reactor experiments. Tab. 1.1 shows a list of reactor antineutrino experiments measuring neutrino oscillations with their baselines (i.e., distance from the source).

| Category | Name | Power [$GW_{th}$] | Baseline [km] | Mass [ton] | Years | Dominant Parameters |
|---|---|---|---|---|---|---|
| Long | KamLAND | various | 180 (avg.) | 1000 | 2001–now | $\Delta m^2_{21}$, $\theta_{12}$ |
| Short | Double Chooz | $4.25 \times 2$ | 1.05 | 8.3 | 2011–2018 | $\theta_{13}$, $\lvert\Delta m^2_{31,32}\rvert$ |
| | Daya Bay | $2.9 \times 6$ | 1.65 | $20 \times 4$ | 2011–2020 | $\theta_{13}$, $\lvert\Delta m^2_{31,32}\rvert$ |
| | RENO | $2.8 \times 6$ | 1.38 | 16 | 2011–now | $\theta_{13}$, $\lvert\Delta m^2_{31,32}\rvert$ |
| Medium | JUNO | 26.6 (tot) | 53 | 20000 | 2024–now | $\Delta m^2_{21}$, $\theta_{13}$, $\lvert\Delta m^2_{31,32}\rvert$, $\theta_{12}$ |

***Table 1.1:*** *Summary of reactor neutrino experiments.*

The electronic neutrino survival probability from 1.18 can be written as

$$P(\bar{\nu}_e \rightarrow \bar{\nu}_e) = 1 - sin^2(2\theta_{13})(cos^2\theta_{12}sin^2\Delta_{31} + sin^2\theta_{12}sin^2\Delta_{32}) - cos^4\theta_{13}sin^2(2\theta_{12})sin^2\Delta_{21} \quad (1.19)$$

Where $\Delta_{ij} = \frac{(m_i^2 - m_j^2)L}{4E}$, in which L is the baseline and E is the antineutrino energy. Fig. 1.2 shows a plot of $P_{ee}$ vs $L/E$ with highlighted the two different NMO possibilities (Fig. 1.2b) and oscillation parameters (Fig. 1.2a).

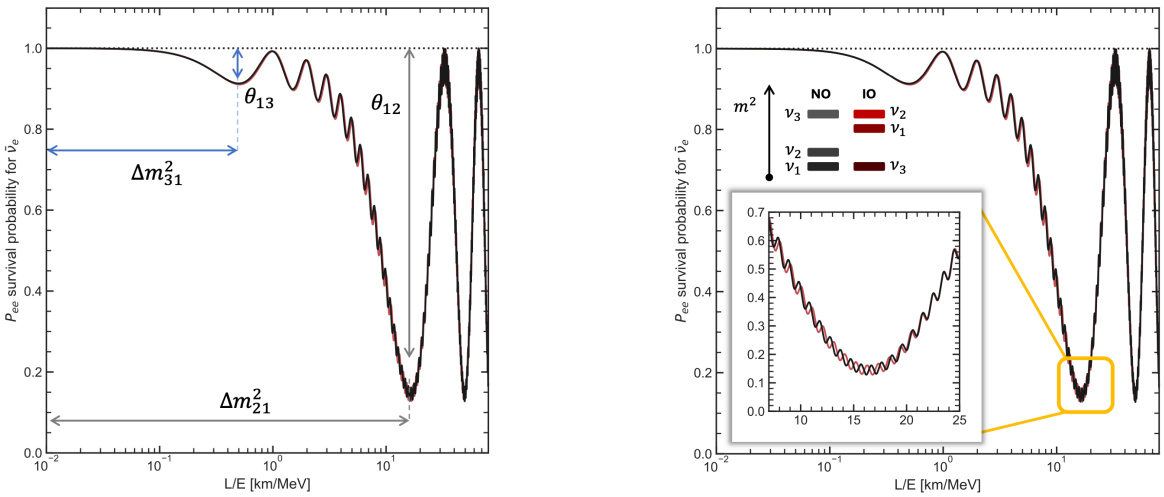


***(a)*** *$P_{ee}$ with oscillation parameter contributions.* ***(b)*** *$P_{ee}$ for Normal and Inverted Ordering.*

***Figure 1.2:*** *Electron antineutrino survival probability $P_{ee}$ as a function of $L/E$. Left: effect of individual oscillation parameters. Right: comparison between NO and IO spectrum at maximum shift.*

There are two limit cases of relation 1.19:

- Experiments with baselines of $O(100)$ km (the so-called "Long-Baseline Experiments"), sensitive to $\Delta m^2$ values in the range $10^{-5}$–$10^{-4}$ $eV^2$. These experiments measured $\Delta m^2_{21} \simeq 7.6 \times 10^{-5}$ $eV^2$.

- Experiments with baselines of approximately 1 km (the so-called "Short-Baseline Experiments"), sensitive to $\Delta m^2$ values in the range $10^{-3}$–$10^{-2}$ $\mathrm{eV}^2$. These experiments measured $|\Delta m^2_{31}| \simeq 2.5 \times 10^{-3}$ $\mathrm{eV}^2$.

As was also shown in Tab. 1.1, experiments are designed with different baselines because of the different scale of mass splittings found by neutrino experiments. A particularly advantageous baseline is approximately $L \approx 50$ km, which allows the experiment to be simultaneously sensitive to both solar and atmospheric oscillation parameters. Moreover, at this baseline, as can be seen in Fig. 1.2b, the phase shift induced by the choice of the NMO is maximal. This configuration is being exploited for the first time by the JUNO experiment, which is the focus of the present thesis. Its experimental apparatus and physics goals will be discussed in detail in the following Chapter.

# 2

# The JUNO Experiment

JUNO [7] is a multipurpose experiment designed to unveil fundamental neutrino properties, explore their astrophysical and terrestrial origins, and search for physics beyond the SM. Its Central Detector (CD) comprises 20 kilotons of LS, enclosed in a 35-meter-diameter acrylic sphere supported by 591 stainless steel rods and located 680 meters underground in Guangdong, China. The scintillator is optically monitored by 17,612 20-inch and 25,600 3-inch Photomultiplier Tubes (PMT), forming the Large-PMT (LPMT) and Small-PMT (sPMT) systems, and is submerged in ultra-pure water for shielding and muon veto purposes. As of December 2024, JUNO has entered the commissioning phase and begun filling the CD—initially with water, which is gradually being replaced with LS. Located 53 km from the Yangjiang and Taishan nuclear power plants, JUNO is optimized for determining the NMO by detecting reactor $\bar{\nu}_e$ via the Inverse Beta Decay (IBD) reaction.

This chapter is structured into three main sections. Section 2.1 provides a description of the experimental site of JUNO. Section 2.2 outlines the experimental apparatus. Following a general introduction to the detector, special attention will be given to the subsystems relevant to this thesis work: the LS purification system (related to the radiopurity analysis presented in Chapter 4), the photon detection system and the readout electronics, as well as the calibration systems, which are essential for the timing studies in Chapter 3 and for the vertex reconstruction and resolution studies discussed in Chapter 5. The chapter concludes with Section 2.3, which describes the physics goals of JUNO, the strategy to determine the NMO and the related requirements, as well as the experiment's timeline from construction to the current LS filling phase.

## 2.1 JUNO Location

The JUNO experiment [7] is located in Jinji town, 43 km southwest of Kaiping city, a county-level city in the prefecture-level city Jiangmen in Guangdong province, China. The distances to several megacities, Guangzhou, Shenzhen, and Hong Kong, are all around 200 km. Due to the absence of high mountains in the allowed area where the sensitivity to the mass ordering is optimized, the JUNO detector is deployed in an underground laboratory under the Dashi hill. As shown in Fig. 2.1, the experimental site is at equal distances of about 53 km from the Yangjiang and the Taishan Nuclear Power Plant (NPP), optimized to have the best sensitivity for determining the mass ordering.


***Figure 2.1:*** *Location of the JUNO site.*

Reactor electron antineutrino is the primary source in the JUNO detector. Yangjiang NPP has six reactor cores of 2.9 GWth each (thermal power). Taishan NPP has two cores of 4.6 GWth each in operation. The total thermal power of the Yangjiang and Taishan NPPs is 26.6 GWth. Other further NPPs contribute in smaller fractions to the overall antineutrinos flux detected in JUNO. The Daya Bay nuclear complex is 215 km away from the JUNO detector. It includes the Daya Bay NPP, the Ling Ao NPP, and the Ling Ao-II NPP in a spread of 1.1 km, each with 2 cores of 2.9 GWth. They will contribute about 6.4% of the reactor antineutrino events in the JUNO detector considering oscillation. The thermal power of all cores and the baselines (distances to the JUNO detector) are listed in Table 2.1.

| **Core** | YJ-1 | YJ-2 | YJ-3 | YJ-4 | YJ-5 | YJ-6 | TS-1 | TS-2 | DYB | HZ |
|---|---|---|---|---|---|---|---|---|---|---|
| **Power (GW)** | 2.9 | 2.9 | 2.9 | 2.9 | 2.9 | 2.9 | 4.6 | 4.6 | 17.4 | 17.4 |
| **Baseline (km)** | 52.74 | 52.82 | 52.41 | 52.49 | 52.11 | 52.19 | 52.77 | 52.64 | 215 | 265 |

***Table 2.1:*** *Summary of the thermal power and baseline to the JUNO detector for the Yangjiang (YJ) and Taishan (TS) reactor cores, as well as the remote reactors of Daya Bay (DYB) and Huizhou (HZ). Taken from [7].*

## 2.2 Detector Design

The JUNO detector system [7] includes a 20 kton LS detector (the CD), a water Cherenkov detector (the Water Pool (WP)) in which the CD is submerged, and a plastic scintillator array on top of them (the Top Tracker). A schematic view of the detector is shown in Fig. 2.2.

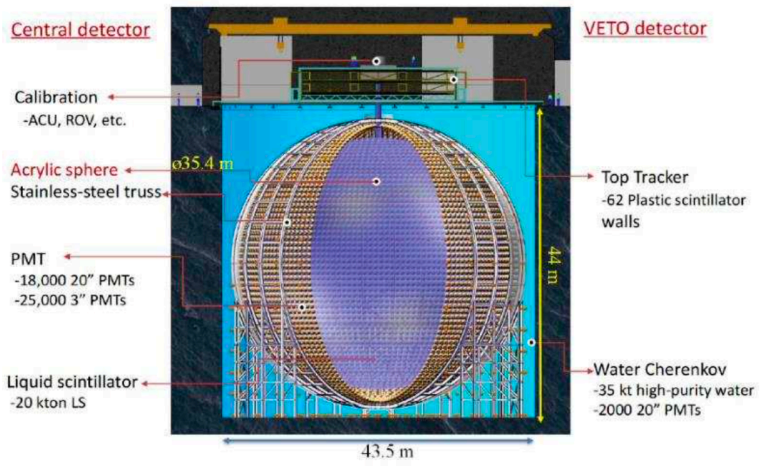


***Figure 2.2:*** *Schematic view of the JUNO detector. Taken from [8].*

The CD is one of the most challenging components of JUNO, particularly from a mechanical perspective, due to its large size and the significant mechanical stresses it must withstand. The LS is contained in a spherical Acrylic Vessel (AV) with an inner diameter of 35.4 m and a thickness of 120 mm. The AV is supported by a spherical stainless steel shell structure with an inner diameter of 40.1 m via 590 Connecting Bars. The shell structure is kept in position by 30 pairs of Supporting Legs, made of stainless steel truss structures and rooted on the concrete floor of the WP.

The light emitted by the LS is detected by 17'612 20-inch PMTs and 25'600 3-inch PMTs, which are installed on the inner surface of the stainless steel structure. The entire LS detector is submerged in a cylindrical WP. A water buffer of 1.42 m thickness between the AV and the PMT surface protects the LS from the PMT glass's radioactivity. The water buffer is connected with the outer water Cherenkov detector but is optically separated through a layer of Tyvek. A chimney for calibration operations sits on top of the AV.

The WP has a diameter of 43.5 m and a height of 44 m, providing sufficient buffer in all directions to protect the LS from the surrounding rock radioactivity. The WP is equipped with 2'400 20-inch PMTs, mounted on the Main Structure, acting as a Cherenkov detector for the cosmic muons. The muon detection efficiency is expected to be 99.8%. Compensation coils are installed on the Main Structure to protect the PMTs from the Earth magnetic field.

On top of the WP, a muon tracker will be installed to measure the muon directions. Plastic scintillator strips decommissioned from the Target Tracker of the OPERA experiment [9] have been reused

as the JUNO Top Tracker [10]. The Top Tracker is composed of 62 walls, each with a sensitive area of $6.7 \times 6.7$ m$^2$. It covers approximately 60% of the CD and intercepts about 30% of the muon flux, providing precise tracking of their direction.

In the following sections, a more accurate description of some of the detector subsystems, which are functional for the analyses presented in this thesis work, will be provided.

### 2.2.1 The LS purification system

The preparation of the LS requires high attention to meet the strict requirements set by the JUNO collaboration. The LS mixture consists of three components: Linear Alkyl Benzene (LAB), 2,5-diphenyloxazole (PPO), and 1,4-bis(2-methylstyryl)benzene (bis-MSB). The optimal composition was determined to be purified LAB with 2.5 g/L of PPO and 3 mg/L of bis-MSB [11]. Although LAB and PPO are supplied with low levels of U/Th contamination at the production stage, a combined system of purification plants [7] has been designed to further enhance the optical and radiopurity properties of the LS, as illustrated in Fig. 2.3. At the surface facility, raw LAB passes through alumina columns and a distillation plant before being mixed with PPO and bis-MSB. The resulting LS is then transferred underground via electro-polished pipelines for the final two purification stages: water extraction and stripping. After a final quality check using the Online Scintillator Internal Radioactivity Investigation System (OSIRIS) - a fully working 20-ton LS detector on its own - [12], the purified LS is delivered to the Filling, Overflow, and Circulation (FOC) system.

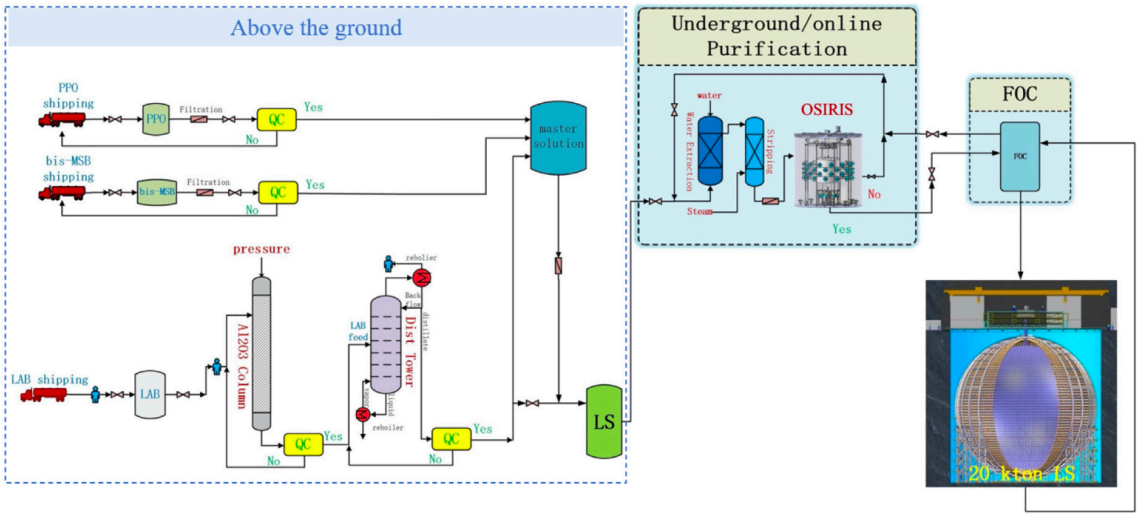


***Figure 2.3:*** *Flowchart of the liquid scintillator processing system. Taken from [12].*

More specifically, the LS processing system of JUNO is composed of:

1. **Alumina column system:** The LAB will be purified by the alumina ($Al_2O_3$) columns to improve transparency. The system consists of eight filtration columns, two alumina filling tanks, and three buffer tanks. The height of the column is 2.6 m, and the diameter is 60 cm.
2. **Distillation system:** Distillation in a partial vacuum (5 mbar) is used in the second stage of the

purification process to remove the heaviest radio-impurities ($^{238}$U, $^{232}$Th and $^{40}$K) from the LAB and to further improve its optical property in terms of absorbance and attenuation length.

3. **Mixing system:** The mixing system is located in the surface LS hall. It is responsible for dissolving PPO and bis-MSB into LAB to form LS master solution batch by batch. Acid/water washing is also performed to the master solution to purify PPO and bis-MSB at this stage. Finally, the master solution will be diluted with LAB to form LS and transported to underground facilities.

4. **Water extraction system:** The water extraction system is used to remove $^{238}$U and $^{232}$Th backgrounds from the LS, especially impurities introduced by PPO and bis-MSB.

5. **Stripping System:** The stripping plant is the final stage of the purification procedure. The main purpose of the plant is the removal of radioactive gases and gaseous impurities from the LS phase, using a gaseous stream of nitrogen and/or superheated steam in counter-current flow mode.

6. **OSIRIS:** Is a stand-alone detector to monitor the radiopurity of the LS while the JUNO CD is filled and to confirm the proper operation of the purification plants. The aim is to guarantee that the concentrations of $^{238}$U and $^{232}$Th in the LS do not exceed the given limits. OSIRIS is located in a bypass to the main LS line, permitting to sample a relevant fraction of the LS processed in the purification plants. The detector design consists of a cylindrical AV with a height and diameter of 3 m holding the LS. The AV is mounted inside a water-filled steel tank (height and diameter 9 m), which provides shielding against external radiation.

7. **FOC:** The FOC system has one storage and two overflow tanks with a volume of 50 $m^3$ each. It also includes a nitrogen flushing system, the piping connected to the chimney of the CD, and a control platform. It has three primary functions: (1) filling pure water into the AV synchronously with the filling of the WP, then replacing water with LS during this LS production period; (2) stabilizing the LS level in the AV within 20 cm when the liquid temperature varies within $(21 \pm 1.4)\,^{o}C$ during operation; (3) circulating the LS in the detector through the underground LS purification systems for the online purification.

It is challenging to quantitatively demonstrate that the LS can be purified to the extremely low levels required by the collaboration's radiopurity goals - namely, the concentration of U/Th has to be below $1 \cdot 10^{-15}$ g/g for reactor neutrino studies and $1 \cdot 10^{-17}$ g/g for solar neutrino studies - solely based on the specifications of the purification systems. The only viable approach to meet the ambitious radiopurity goals is to monitor the radiopurity both before and during the injection of LS into the CD using real data. This analysis was carried out as part of the commissioning activities and is discussed in Chapter 4.

### 2.2.2 Photon Detection System

The photon detection system identifies the scintillation light generated by interactions of particles with the LS. To achieve the target energy resolution of 3% @ 1 MeV [7], high photocathode coverage is requested, and it is provided by two independent PMT systems: the main system is the large 20-inches PMTs system (the so-called LPMT system) contributing to a 75.2% coverage; additionally, a small 3 inches PMTs system (the so-called sPMT system) is used for double calorimetry measurements providing and additional coverage of 2.7%. Concerning the LPMT, two PMT types have been selected for JUNO, baased on considerations on high detection efficiency for scintillation photons, low dark noise rate, high gain, stable, reliable and long life-time and timing properties [13]:

- The **Hamamatsu** R12860-HQE is a conventional dynode PMT developed by Hamamatsu Photonics K.K. The principle of operation of a dynode PMT is simple: first, the incoming photon is converted to an electron upon hitting the photocathode, due to photoelectric effect [14]. The electron (which is also called Photoelectron (PE)) is then accelerated through a series of dynode exploiting a High Voltage (HV) electric field; upon hitting the dynodes, more electrons are knocked out. This cascade effect multiplies exponentially the number of electrons until they are collected and measured as a current at the anode. The working principle is shown in Fig. 2.4a. The Hamamatsu PMTs feature a Quantum Efficiency (QE) at 400 nm around 30%, a Transit Time Spread (TTS) around 1.15 ns, and a dark noise rate below 50 kHz [13].

- The Micro Channel Plate (MCP) PMT, developed by **North Night Vision Technology (NNVT)**, which incorporates a MCP in place of the conventional discrete dynodes. The MCP consists in a two-dimensional array of channels with a 6-20 $\mu$m diameter bundled in parallel. Each channel acts as an independent electron multiplier. As shown in Fig. 2.4b, the PEs emitted from the photocathode enter the channels of the MCP and impinge on the inner wall, where they are multiplied by means of secondary emission. The process is repeated along the channels and finally a large number of electrons are collected by the anode as an output signal. The QE on the MCP-PMTs is about 28.9%, a TTS around 7.65 ns , and the dark noise rate below 100 kHz [13].

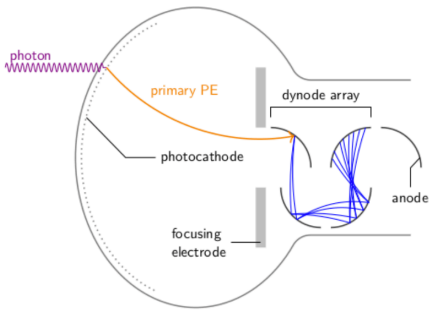


***(a)*** *Working principle of a dynode PMT. Taken from [15]*

.

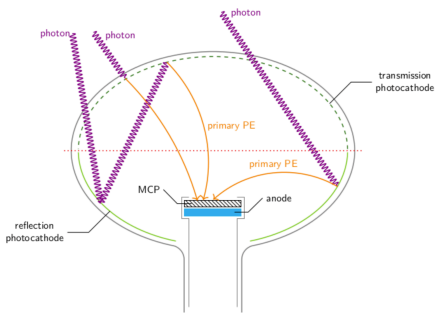


***(b)*** *Working principle of an MCP-PMT. The reflection photocathode at the bottom part of the glass bulb allows for a second photon-electron conversion chance. Taken from [15].*

***Figure 2.4:*** *Functional diagram of the types of LPMT present in JUNO.*

### 2.2.3 Readout Electronics

The JUNO readout electronics will have to process the signals from different LPMT systems. The CD features 17'612 LPMTs, which can be considered as the main system. An additional set of PMTs is installed in the WP surrounding the CD, consisting of 2,400 extra PMTs, together with 348 MCP PMTs mounted in three rings and 600 8-inch Dynode PMTs (to enhance the photon detection coverage for interactions occurring within the WP). The main task of the LPMTs readout electronics is to [16]:

- Receive and digitize the analog signals from the PMTs and transmit all the relevant information to the Data Acquisition (DAQ) without a significant loss of data quality.
- Generate local trigger requests based solely on the single-PMT waveform and transmit this information upstream in order to be evaluated globally.

A scheme of the JUNO LPMT electronics is given in Figure 2.5.

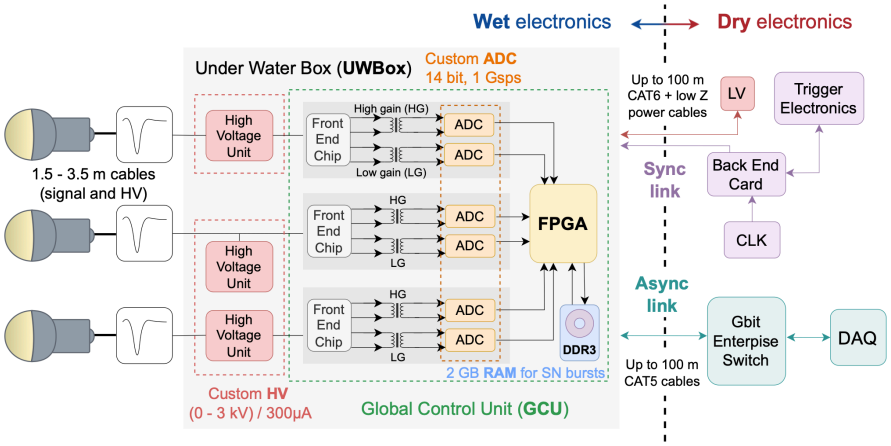


***Figure 2.5:*** *JUNO LPMT readout electronics scheme. A description of the different parts is given in the text. Figure taken from [17].*

As can be seen from Fig. 2.5, the full electronics chain is composed of two parts:

1. **The Front-End (FE) (or wet) electronics [16]:** located very close to the LPMT output, installed on the JUNO Steel Truss structure inside the JUNO WP, inside a stainless steel, water-tight box (the so-called Under Water Box (UWBox)). Three PMT output signals are fed to one UWBox which contains:

   - Three High Voltage Unit (HVU): programmable modules which provide the bias voltage to the PMT voltage divider. Each HVU independently powers one large PMT.
   - One Global Control Unit (GCU): a motherboard incorporating the FE and Readout electronics components. The three PMT signals reaching the GCU are processed through independent readout chains.

   The PMT analog signal reaching the GCU is processed by a custom Front-End Chip (FEC) which provides two outputs with a low and high gain, respectively 0.0850 and 0.5856 [18]. The signal is further converted to a digital waveform by a 14 bit, 1 GS/s, custom Flash Analog-to-Digital

Converter (FADC). The usage of two FADCs per readout channel has been driven by the design requirement of providing a wide dynamic range in terms of reconstructed PE: from 1 PE to 100 PE with a 0.1 PE resolution (high gain FADC) and from 100 PE to 1000 PE (low gain FADC) with a 1 PE resolution [19]. A Xilinx Kintex-7 Field Programmable Gate Array (FPGA) (XC7K325T) is the core of the GCU and allows to further process the digital signal and temporarily store it in a local memory buffer before sending it to the DAQ. The Kintex-7 processing unit is responsible for the onboard generation of a trigger request (referred to as local trigger) whenever the digitized signal overpass the preset threshold, the charge reconstruction and the timestamp tagging of the acquired waveforms. Besides the local memory available in the readout-board FPGA, a 2 GBytes DDR3 memory is available and used to provide a larger memory buffer in the exceptional case of a sudden increase of the input rate, which overruns the current data transfer bandwidth between the FE electronics and the DAQ.
The electronics inside the UWBox has two independent connections: a so-called Synchronous Link (S-Link), connected to the Back-End (BE) electronics, which provides the clock and synchronization signals to the boards, handles trigger primitives (details on synchronization in JUNO are given in Chapter 3), and transmits the trigger signal along with other propagation signals from the GCU and register readout; and an Asynchronous Link (A-Link), which is connected to a switch and then, via optical fiber, to the DAQ server.

2. **The Dry electronics:** Installed in the electronics rooms of the JUNO underground laboratories are the BE (backend) electronics and the DAQ system. The BE electronics, whose purpose is to collect the trigger requests from the UWBox units and validate them upon fulfillment of the predefined criteria, consists of the following active components: the Back-End Card (BEC) with the Trigger and Time Interface Mezzanine (TTIM), the Reorganize and Multiplex Units (RMU), and the Central Trigger Unit (CTU).

The electronics design, in terms of both hardware and firmware, is driven by the following key-points:

- **Photon Arrival Time Reconstruction:** precise reconstruction (level of ns) of the photon detection time in the detector is essential in order to retrieve the position of the events with resolution on the order of cm. This is particularly important, since (a) the energy response of the detector is position-dependent and (b) precise space-time information of the events allow for an efficient detection and discrimination of prompt and delayed IBD events, which will support background suppression.
- **Low Dead Time and Dynamic Acquisition Rate:** the readout electronics not only has to be able to acquire neutrino events from reactor, solar, geological or atmospheric origin without inefficiency, but it has also to be designed in order to cope with short episodes of extremely high trigger rate that might be caused by neutrino bursts from a nearby galactic Supernovae (SN). Dependent on the distance, thousands of neutrino events are expected within a period of seconds.

### 2.2.4 Calibration System

The hardware design of the calibration system [20] is driven to anchor the energy scale and characterize possible non-linear effects due to quenching in the scintillator and in the readout. Such a system is capable to place a source along the central axis of the CD, on a circle at the LS-acrylic boundary, and in the region in between. To ensure the low background environment of the CD, the total requirement of introduced background from the calibration systems should be less than 0.5 Hz [21]. The corresponding hardware design consists of several independent subsystems (figure 2.6).

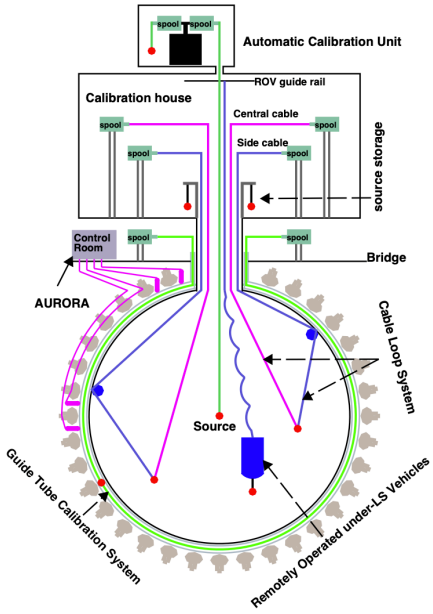


***Figure 2.6:*** *Overview of the calibration system (not to scale), including the ACU, two CLS, the GT, and the ROV. The red points represent a source assembly. The AURORA is an auxiliary laser diode system to monitor the attenuation and scattering length of the LS.*

More in detail, the various independent subsystems are:

- The **Automatic Calibration Unit (ACU)**: developed to do calibration along the central vertical axis z of the CD. The design is very similar to the ACU in the Daya Bay experiment [22], with four independent spools mounted on a turntable. Each spool is capable to unwind and deliver the source via gravity through the central chimney of the CD, with a better than 1 cm positioning precision in z. To be flexible, the fourth spool will carry a replaceable source (e.g., a radioactive source or even a temperature sensor).
- The **Guide Tube (GT)**: is a tube looped outside of the acrylic sphere along a longitudinal circle similar to that used in Double Chooz [23] and CUORE [24]. Within the tube, a radioactive source with cables attached to both ends gets driven around with a positioning precision of 3 cm. The design of this system is discussed in details in Ref. [25].
- Two **Cable Loop Systems (CLS)s**: installed in the two opposite half-planes to deploy sources to off-axis positions. The design concept is inspired by those in Sudbury Neutrino Observa-

tory (SNO) [26], KamLAND [27], and Borexino [28]. For each CLS, two cables are attached to the source, which also form a loop to deliver and retract the source. Different sources can be interhanged on the CLS. The central cable goes upwards towards the north pole of the CD. The side cable winds through an anchor on the inner surface of the acrylic sphere, then also towards the north pole the CD. By adjusting the lengths of the two cables, the source could be delivered ideally within an area bounded by the vertical lines through the anchor and the central axis.

- A **Remotely Operated Vehicle (ROV)** [29]: similar to that in the SNO experiment [30], and capable of deploying a radioactive source in almost the entire LS volume.
- An **independent ultrasonic positioning system** [31]: eight ultrasonic receivers will be mounted inside the acrylic sphere, and the source deployed by the CLS or ROV will carry a miniature ultrasonic emitter. Based on tests, such a system is capable to provide a positioning precision to a level of 3 cm.

The JUNO collaboration envisions to separate the program into comprehensive (but infrequent), weekly and monthly calibrations. As a requirement, source deployments should not introduce noticeable radioimpurity such as radon. The nominal speed of the source movement is about 1 m/min. Table 2.2 summarises a reference plan for all types of calibration.

| System | Source | Energy [MeV] | Points | Time [min] |
|---|---|---|---|---|
| **Comprehensive calibration** | | | | |
| ACU-CLS-GT | Neutron (Am-C) | 2.22 | 250 | 1942 |
| ACU | Neutron (Am-Be) | 4.4 | 1 | 75 |
| ACU | Laser | / | 10 | 391 |
| ACU | $^{68}$Ge | 0.511 × 2 | 1 | 75 |
| ACU | $^{137}$Cs | 0.662 | 1 | 75 |
| ACU | $^{54}$Mn | 0.835 | 1 | 75 |
| ACU | $^{60}$Co | 1.17+1.33 | 1 | 75 |
| ACU | $^{40}$K | 1.461 | 1 | 158 |
| *Total* | | | | *48 h* |
| **Weekly calibration** | | | | |
| ACU | Neutron (Am-C) | 2.22 | 5 | 63 |
| ACU | Laser | / | 10 | 78 |
| *Total* | | | | *2.4 h* |
| **Monthly calibration** | | | | |
| ACU | Neutron (Am-C) | 2.22 | 27 | 120 |
| ACU | Laser | / | 54 | 147 |
| CLS | Neutron (Am-C) | 2.22 | 40 | 333 |
| GT | Neutron (Am-C) | 2.22 | 23 | 73 |
| *Total* | | | | *11.2 h* |

***Table 2.2:*** *A baseline plan of a comprehensive/weekly/monthly calibration (adapted from [20]).*

## 2.3 JUNO Physics Goals and current status

JUNO was proposed with the determination of the NMO as a primary physics goal. The relatively large value of $\theta_{13}$, measured by Daya Bay in 2012, has opened up the possibility to resolve the NMO in various neutrino oscillation experiments, which include a medium baseline (~50 km) reactor antineutrino $\bar{\nu}_e \rightarrow \bar{\nu}_e$ oscillation experiment (JUNO), long-baseline accelerator (anti-)neutrino $\nu_\mu \rightarrow \nu_e$ oscillation experiments (NO$\nu$A [32] and DUNE [33]), and atmospheric (anti-)neutrino oscillation experiments (INO [34], PINGU [35], ORCA [36], DUNE [33], and Hyper-K [37]). The accelerator and atmospheric experiments rely on the matter effect in neutrino oscillations (the CC interaction between (anti-)$\nu_e$ and electrons in the matter). JUNO is a unique experiment designed to identify the NMO using the oscillation interplay between $\Delta m^2_{31}$ and $\Delta m^2_{32}$ [5]. The NMO sensitivity of JUNO has no dependence on the unknown CP-violating phase and the $\theta_{23}$ octant, playing a key role when combined with other neutrino experiments. At a baseline of 53 km, JUNO will simultaneously measure oscillations driven by small mass splitting ($\Delta m^2_{21}$) and large mass splitting ($\Delta m^2_{31}$ and $\Delta m^2_{32}$), as shown in Fig. 2.7.

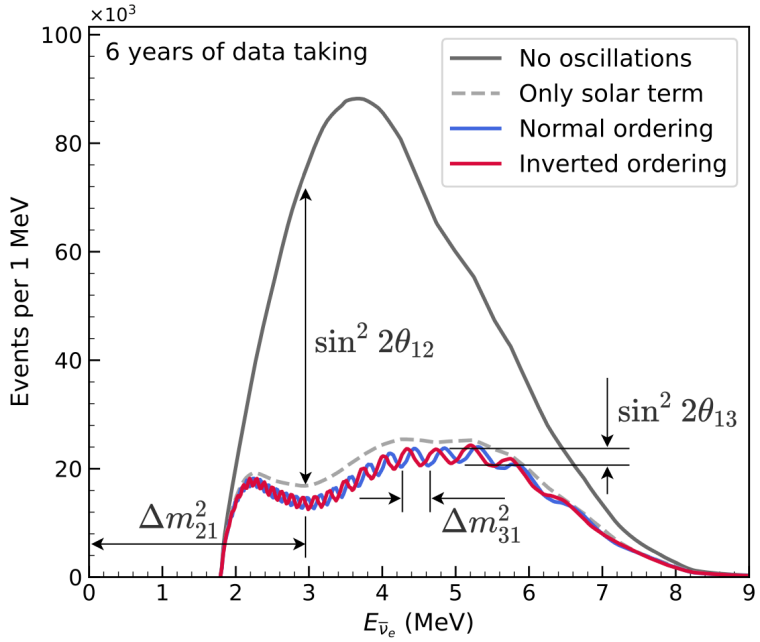


***Figure 2.7:*** *The expected antineutrino energy spectrum weighted by IBD cross-section with (grey, blue and red) and without (black) oscillation at the JUNO experiment for normal ordering (blue) and inverted (red) ordering assuming 6 years of data-taking. Dependence on the four oscillation parameters is shown.*

Precise measurement of the oscillated antineutrino spectrum is key for JUNO to determine the NMO. This requires a 20 kton LS detector with an unprecedented relative energy resolution of $\frac{\sigma_E}{E} = \frac{3\%}{\sqrt{E_{\text{vis}}}}$, with $E_{\text{vis}}$ being the visible energy in the detector (in MeV). The expected precision of $\theta_{12}$, $\Delta m^2_{21}$ and $\Delta m^2_{31}$ measurements will be better than 0.6% (see Fig. 2.8), which will play a crucial role in the future unitarity test of the PMNS matrix.

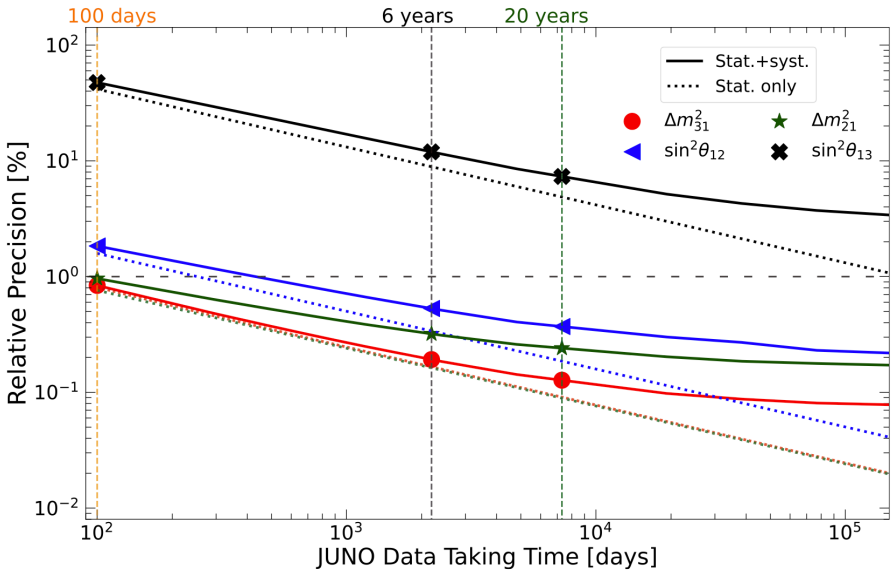


***Figure 2.8:*** *Relative precision of the oscillation parameters as a function of JUNO data taking time. The markers and vertical lines stand for 100 days, 6 years, and 20 years of data taking. The horizontal gray dashed line stands for 1% relative precision. The green dotted and red dotted lines are on top of each other since the statistical-only precision is essentially identical for the $\Delta m^2_{31}$ and $\Delta m^2_{21}$ parameters. Taken from [38].*

The JUNO detector is not limited to detecting antineutrinos from the reactors, but can also observe neutrinos/antineutrinos from terrestrial and extra-terrestrial sources, including supernova burst neutrinos, diffuse supernova neutrino background, geoneutrinos, atmospheric neutrinos, and solar neutrinos [7]:

- A neutrino burst from a typical core-collapse supernova at a distance of 10 kpc (kiloparsec) would lead to ~5000 inverse-beta-decay events and ~2000 all-flavor neutrino–proton elastic scattering events in JUNO, which are of crucial importance for understanding the mechanism of supernova explosion and for exploring novel phenomena such as collective neutrino oscillations. Detection of 1–2 neutrinos per year from all past core-collapse supernova explosions in the visible universe can further provide valuable information on the cosmic star-formation rate and the average core-collapse neutrino energy spectrum.

- Antineutrinos originating from the radioactive decay of uranium and thorium in the Earth - the so-called geoneutrinos - can be detected in JUNO with a rate of ~400 events per year, significantly improving the statistics of existing geoneutrino event samples.

- Atmospheric neutrino events collected in JUNO can provide independent inputs for determining the mass ordering and the octant of the $\theta_{23}$ mixing angle.

- Detection of the $^7$Be and $^8$B solar neutrino events at JUNO would shed new light on the solar metallicity problem and examine the spectral transition region between the vacuum and matter-dominated neutrino oscillations.

### 2.3.1 NMO Strategy and sensitivity

To obtain the NMO sensitivity, JUNO employ the least-squares method, fitting the spectrum assuming the normal ordering or inverted ordering with the chi-squared method and taking the difference of the minima as a measure of the median NMO sensitivity. The discriminator of the NMO can be defined as

$$\Delta\chi^2_{\text{min}} = \left|\chi^2_{\text{min}}(\text{NO}) - \chi^2_{\text{min}}(\text{IO})\right|, \tag{2.1}$$

where the minimization process is implemented for all the relevant nuisance parameters including oscillation parameters. With the inputs described above, JUNO obtain $\Delta\chi^2 = 10$, which shows the NMO can be determined with a significance of $3\sigma$ in 6 years of data taking [39]. Figure 2.9 shows the distribution of $\Delta\chi^2_{\text{min}}$ as a function of exposure and energy resolution.

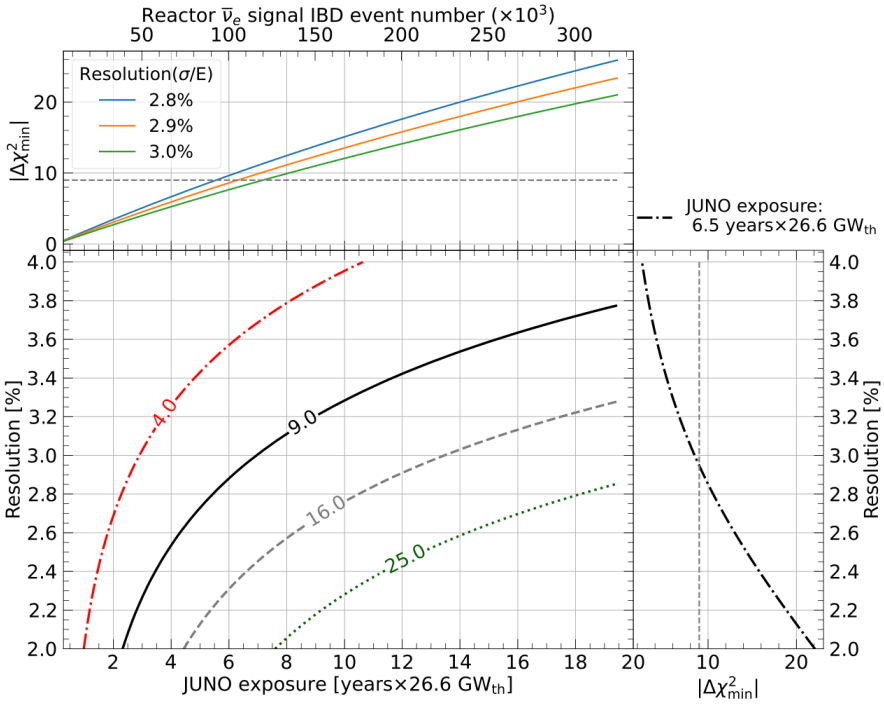


***Figure 2.9:*** *Contours of $\Delta\chi^2_{\text{min}}$ as a function of exposure and energy resolution at 1 MeV under the assumption of NO. The resolution is scanned by varying $a$ and fixing $b = 0.64 \times 10^2$, $c = 1.20 \times 10^2$ MeV. The black, gray, and green contour lines denote $3\sigma$, $4\sigma$, and $5\sigma$ significance levels, respectively. The top panel shows the time evolution of the $\Delta\chi^2_{\text{min}}$ for the energy resolution of 2.8%, 2.9%, and 3.0% at 1 MeV. The right panel shows the required energy resolution to $\Delta\chi^2_{\text{min}}$ under the JUNO exposure of 6.5 years ×26.6 GWth (data-taking time of 7.1 years with a reactor duty cycle of 11/12). Taken from [40].*

In addition, as shown in Ref. [41], electron antineutrino disappearance and muon neutrino (antineutrino) appearance experiments will prefer a different value of $\Delta m^2_{32}$ when the wrong NMO hypothesis is tested in a common statistical analysis of the oscillation data. The corresponding tension provides additional power to exclude the wrong NMO hypothesis and greatly boosts the sensitivity of the NMO measurement. As a consequence, a combined analysis between JUNO and an accelerator-based or atmospheric-based NMO experiment will reach much better sensitivity than expected from a simple sum of $\Delta\chi^2$. The boosted $\Delta\chi^2$ due to the combination effect of different types of experiments relies

on the precisions of $\Delta m^2_{31}$ (or $\Delta m^2_{32}$) from individual experiments. The determination of $\Delta m^2_{32}$ with a high precision of 0.6% or better in the JUNO experiment via reactor antineutrinos provides unique information in the NMO combined analysis.

### 2.3.2 JUNO STATUS

The civil construction and excavation of the underground laboratory began on October 1, 2015. Within the WP cavity, the installation of the stainless steel structure started on December 19, 2021, and the first panel of the acrylic vessel was installed on June 27, 2022. The installation of the LPMT system and its readout electronics was completed on October 23, 2022, and November 29, 2022, respectively, while the installation of the sPMT system took place in parallel, beginning on November 23, 2022. The bottom door of the WP was installed on December 17, 2024, followed immediately by the filling of the detector with water, which began on December 18, 2024, and was completed on February 2, 2025. The JUNO WP was fully sealed on December 30, 2024, while the installation of the first Top Tracker module commenced on November 1, 2024. After the CD and WP were completely filled with water, a new phase of LS filling began on February 8, 2025, marking the start of the Commissioning period, which is expected to be completed by August 2025. This thesis work is situated precisely within this hybrid Water–LS configuration phase, where all efforts are focused on analyses related to commissioning and the very first data collected by the detector — the culmination of a decade-long construction effort.

# 3

# Electronics synchronization studies

This chapter presents a detailed investigation of the LPMT electronics time synchronization in the JUNO detector, carried out as part of the commissioning activities. Synchronization in JUNO is crucial to achieving the experiment's design precision, including accurate vertex reconstruction and, consequently, excellent energy resolution. The latter depends, among other factors, on the corrections for detector non-uniformity, which in turn rely on precise vertex reconstruction. For further details, see Chapter 5. In JUNO, it is required that the synchronization of local clocks among the GCUs (i.e., the clock signal within individual GCUs) is maintained at the nanosecond level. However, this requirement can be challenged by phenomena such as offsets with respect to the global clock (as seen by the CTU) or clock drifts between different GCUs.

The study is based on the analysis of calibration runs employing a 420 nm laser - a wavelength selected to ensure negligible absorption by the LS - positioned at the detector's center. From these runs, the primary observable of interest, the PMT Transit Time (TT), is derived. The adopted analysis methodology involves the following steps (described in detail in Section 3.2): first, the hit time is estimated from the waveforms using the Constant Fraction Discriminator (CFD) technique; subsequently, the analytically calculated Time of Flight (ToF) is subtracted, and all timings are referenced to the Trigger Time ($t_0$) after applying corrections for jitter-induced uncertainties. The resulting TT distribution provides two critical pieces of information: (1) the TTS (i.e., the fluctuation in TT between individual pulses), which serves as a metric for the intrinsic time resolution of individual PMTs, and (2) insights into the overall system synchronization. To assess the influence of hardware operations on synchronization performance, multiple laser runs were analyzed, each preceded by distinct procedures - including GCU hard resets and Precision Time Protocol (PTP) synchronizations (i.e., a protocol for precise clock synchronization applicable to systems like JUNO that implement multicast communication model between the masters and timing nodes). This comparative approach allows for the evaluation of how such operations affect the timing alignment between GCUs in JUNO.

This chapter is organized as follows: Section 3.1 introduces the synchronization of the JUNO LPMT electronics; subsequently, the proposed method for the extraction of the TT is presented in Section 3.2. Finally, in Section 3.3, a study of the TT distribution for individual PMTs is conducted, in order to extract and discuss the distribution of TTS and to assess the stability of the time synchronization in JUNO during the commissioning phase.

## 3.1 JUNO SYNCHRONIZATION SYSTEM

The timing architecture [16] is built around the CTU, which generates and distributes the global reference time through a White Rabbit (WR) network [42] to RMU and then BEC receivers (via TTIM boards), achieving sub-nanosecond synchronization accuracy at this level. However, since the Front-end Electronics (FEE) (or "wet") operate on local clock counters that initialize asynchronously following GCU power cycles or hard-resets, each GCU develops a unique time offset relative to the global CTU reference. These offsets, which can reach several nanoseconds without correction, directly impact PMT response alignment and consequently degrade the reconstruction of essential physics observables including, vertex position, energy measurement and particle identification. To maintain system-wide coherence, JUNO implements a hierarchical synchronization scheme combining the IEEE 1588 PTP protocol [43] with WR network, establishing a complete timing chain from the CTU through BECs to individual GCUs. A schematic example of the JUNO synchronization scheme is shown in Fig. 3.1.

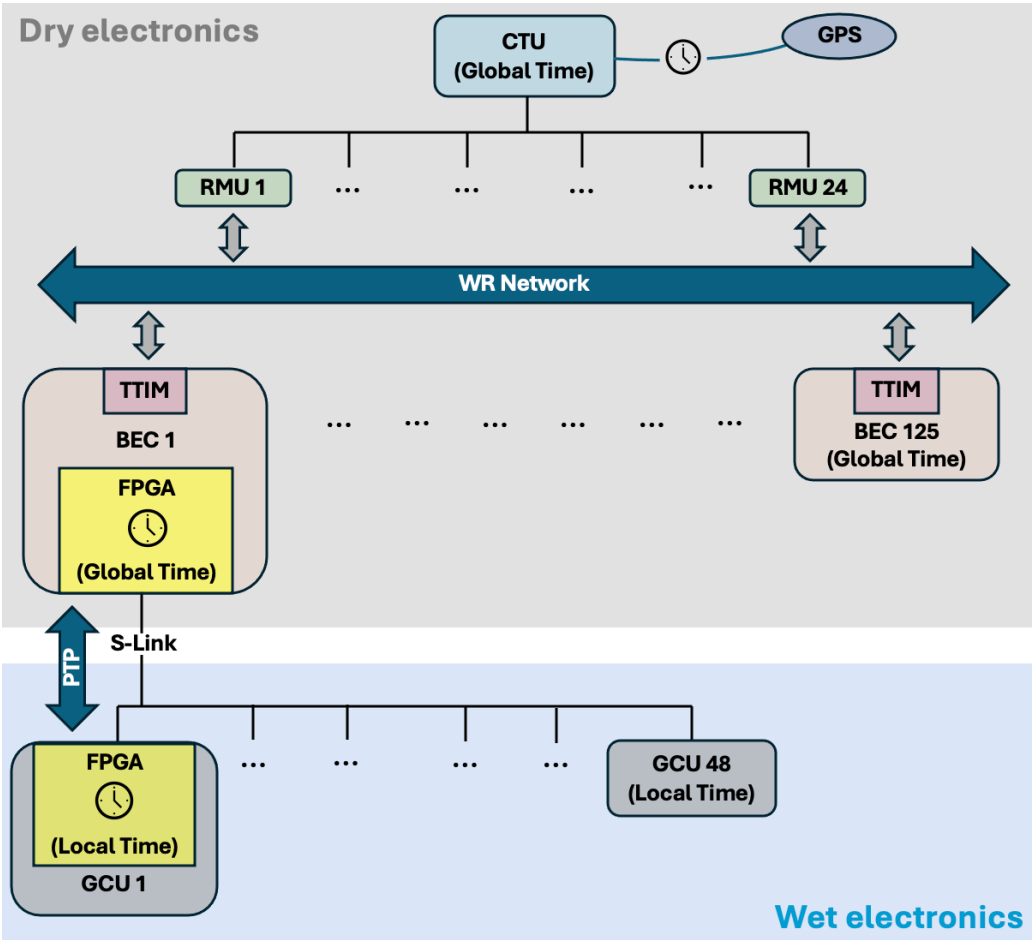


***Figure 3.1:*** *JUNO synchronization scheme overview.*

The WR system is a technology originally developed by Conseil européen pour la recherche nucléaire (*European Organization for Nuclear Research*) (CERN) and Gesellschaft für Schwerionenforschung (*Centre for Heavy Ion Research*) (GSI) for the use at accelerators. Applying WR in JUNO offers the following

advantages [43]: (i) the low-jitter recovered clock from Synchronous Ethernet (SyncE) provides a reference frequency for the electronics; (ii) sub-nanosecond phase alignment can be achieved among all nodes.
From the back-end level synchronized through the WR network, the global clock signal must be distributed to the front-end cards that count the time locally. The timing system ensures that:

- The clock signal is distributed from the CTU to all the GCU, to avoid any drifting of the local counters;
- The offset between the counters with respect to the global time counter is measured and corrected.

The synchronization procedure between the back-end and front-end layer has been based on an hardware implementation of the IEEE 1588-2008 standard [43], which theoretically guarantees the synchronization between global and local clocks inside a window of ± one clock period.

#### The IEEE 1588-2008 PTP Protocol

The IEEE 1588-2008 standard [44] defines a protocol for precise clock synchronization applicable to systems that implement a multicast communication model between the master and timing nodes. In JUNO the idea is to exploit the delay request-response mechanism measurement defined in the IEEE 1588-2008 standard to compensate for the offset error between Back-End Electronics (BEE) and FEE. Figure 3.2 shows the protocol implemented. $t_{1g} - t_{1l}$ is the clock offset to be measured and compensated. The offset measurement procedure is accomplished in eight steps:

1. The master records the current timestamp $t_{1g}$ and sends to the slave a synch message containing the timestamp $t_{1g}$;
2. The slave records the reception time $t_{2l}$ . The slave computes $t_{1g} - t_{2l} = \text{offset} - \text{delay}_{ms}$ where $\text{delay}_{ms}$ is the transmission delay from master to slave;
3. The slave sends a delay request message, without payload, to the master and records the transmission time $t_{3l}$;
4. The master records the reception time $t_{4g}$;
5. The master sends back a delay message containing $t_{4g}$ value;
6. The slave, upon receipt of the $\text{delay}_{resp}$ message computes $t_{4g} - t_{3l} = \text{offset} + \text{delay}_{sm}$;
7. Now, with the assumption that $\text{delay}_{ms} = \text{delay}_{sm}$ , the offset can be computed using:

$$\text{offset} = \frac{(t_{1g} - t_{2l}) + (t_{4g} - t_{3l})}{2} \tag{3.1}$$

8. The slave corrects its clock accordingly.

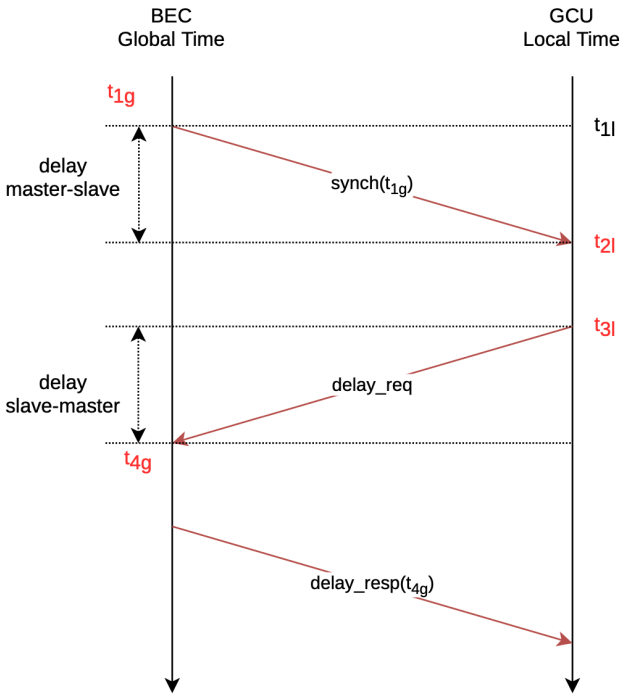


***Figure 3.2:*** *IEEE 1588 PTP offset measurement. Taken from [44].*

The master individually addresses the offset correction procedure to each slave. The procedure can be run at any time, thus ensuring clock alignment during the run of the experiment and offering the possibility to check the synchronization status of all the GCUs. Too frequent offset corrections are indicative of problems and the corresponding GCU should be brought offline for diagnosis. However, the offset correction mechanism highlights several sources of error that potentially limit the clock alignment accuracy [16]. One issue is that the protocol does not specify the clock frequency—lower clock frequencies result in reduced time resolution. Moreover, like all message-based synchronization protocols, PTP time accuracy is affected by asymmetry. Such asymmetry typically arises from the physical medium and the implementation of the data link layer. The assumption $\text{delay}_{ms} = \text{delay}_{sm}$ does not hold in the presence of asymmetry; in fact, the resulting time offset error is equal to one half of the asymmetry.

## 3.2 Transit Time computation

In this section, we address the challenge of identifying a variable derivable from raw data that can robustly characterize the timing performance of PMTs while remaining insensitive to systematic offsets. The physical scenario involves an event occurring at time $t_0$ within the CD, generating photons that propagate through the detector medium (either water or LS) until detection by a PMT. Upon photon absorption and subsequent PE production, the signal undergoes amplification - through dynode-based or MCP multiplication processes depending on the PMT type - before being recorded by the readout electronics as waveform data. To construct a PMT-specific timing variable under the assumption that readout electronics introduce neither channel-dependent nor time-varying delays (only possible uniform temporal shifts), we must consider two fundamental components:

1. The ToF (i.e., the time that the emitted photon takes to reach the PMT), which exhibits PMT-to-PMT variations due to the heterogeneous water-LS detector configuration;
2. The event initiation time $t_0$ (corresponding to the trigger timestamp).

The derived timing variable, designated as TT, is formally defined as:

$$\mathrm{TT} = \mathrm{HitTime} - \mathrm{ToF} - t_0 \tag{3.2}$$

where $\mathrm{HitTime}$ represents the waveform crossing time of the trigger threshold for the individual channel.

Subsequent sections will detail the methodologies for extracting the three constituent variables (HitTime, ToF, and $t_0$) through analysis of a 420 nm laser calibration runs. We will furthermore present a parameterized model of single-PMT response, enabling extraction of performance metrics such as the TTS as key timing resolution descriptors.

### 3.2.1 Hit Time Extraction Methodology

All physical event reconstruction in the detector originates from waveform analysis - specifically, the voltage signals recorded by individual PMTs within a 1008 ns acquisition window. These Analog to Digital Converter (ADC)-sampled signals, acquired with a time resolution of 1 ns, result in a substantial data throughput of approximately 40 Gb/s for an acquisition rate of 1 kHz. To manage this volume, an online data reduction is performed via the Online Event Classification (OEC) system—which categorizes in real time events of possible interest, storing their waveforms, while for events not tagged as of interest, only integrated charge and hit time are stored (12 bytes/hit)—and the Trigger system, which stores data based on predefined selection criteria. Through this combined online processing, the data stream is reduced to approximately 60 Mb/s, allowing for feasible storage and transfer.
Understanding the key features that can be extracted from the waveforms—referred to as time-charge (TQ) variables—is therefore essential, as these parameters are central to both the OEC-based selection and trigger generation. Figure 3.3 shows an example of these components within a representative

420 nm laser calibration waveform:

- **Baseline**: Mean voltage value recorded in the absence of events (as centroid of distribution of signal over the first ns window);
- **Trigger threshold**: The voltage value, set to $V_{\text{baseline}} - 5\sigma_V^{\text{noise}}$, below which the channel sends a trigger primitive to the GCU;
- **HitTime/Rise-Time**: Threshold crossing moments (falling/rising edges);
- **Integrated charge**: Waveform-baseline area between HitTime and Rise-Time.

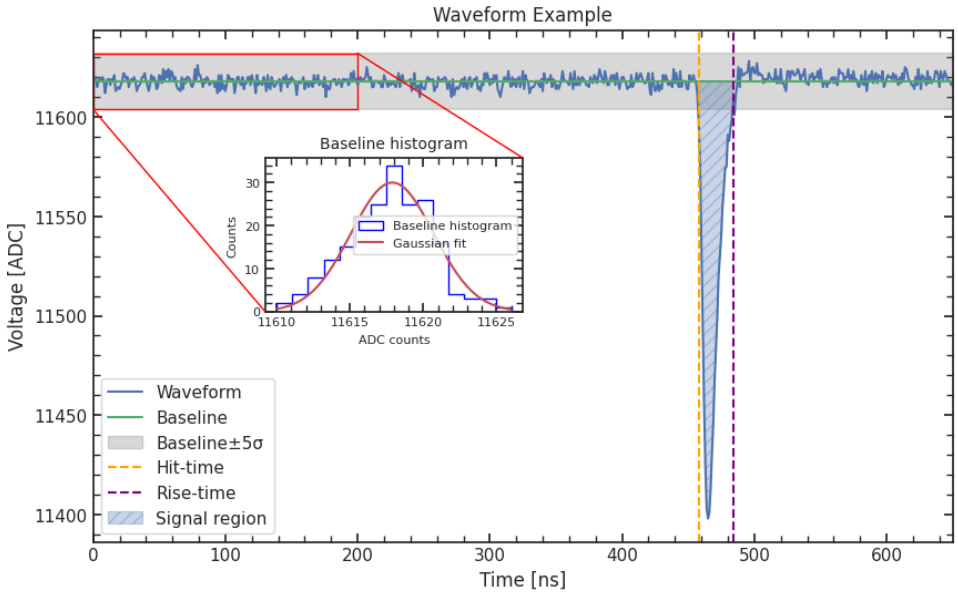


***Figure 3.3:*** *Characteristic waveform with annotated features: signal (blue), baseline (black), threshold region (gray), HitTime (yellow), Rise-Time (purple), and charge integration interval (light blue). The inset demonstrates baseline calculation from the initial 200 ns distribution. Threshold is set at* $V_{baseline} - 5\sigma_V^{noise}$ *where* $\sigma_V^{noise}$ *is the baseline standard deviation.*

The HitTime determination faces inherent precision limitations from 1 ns sampling. While the Leading-Edge Discriminator method (i.e. directly determine the threshold-crossing point from waveform) provides direct measurement, its accuracy suffers from time slewing - dependence on input signal amplitude and rise time - and jitter errors from statistical fluctuations. For Gaussian noise ($\sigma_V^{\text{noise}}$ derived from baseline), the timing uncertainty $\sigma_{jitter}$ follows [45]:

$$\sigma_{\text{jitter}} = \frac{\sigma_V^{\text{noise}}}{\left|\frac{dV}{dt}\right|_{t=T}} \tag{3.3}$$

This approximation requires linear signal behavior near threshold and optimal threshold positioning. An alternative method is the CFD technique: here, the signal is duplicated, with one component delayed by time $d$ and the other attenuated (by a fraction $0 < f < 1$) and inverted. The two components are summed, producing a bipolar signal from which the threshold-crossing time is determined (with

minimized jitter error due to the steeper slope of the CFD signal near the threshold). For a visual representation, see Figure 3.4.

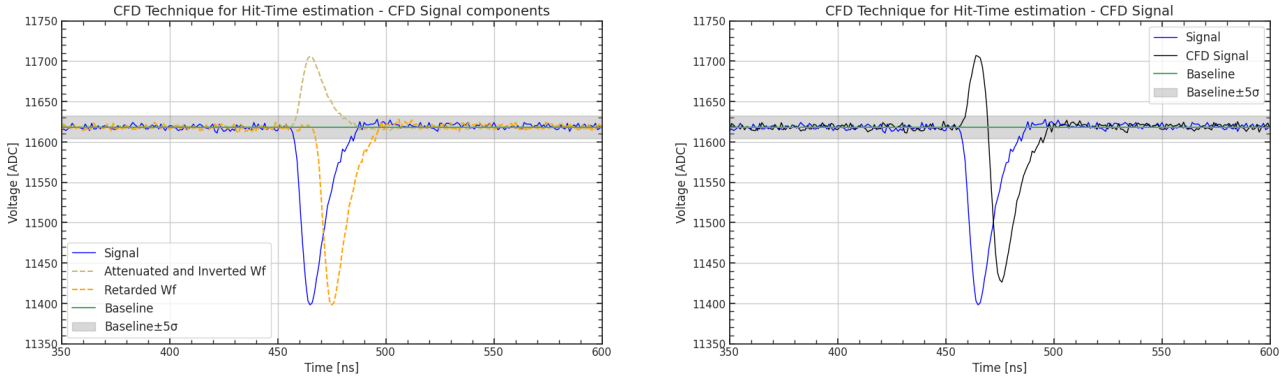


***(a)*** *Signal components: original (blue), delayed (yellow), attenuated/inverted (orange)*

***(b)*** *Resultant CFD signal (black) versus original (blue)*

***Figure 3.4:*** *CFD signal synthesis methodology*

To demonstrate the jitter error reduction and the method's efficacy, Figure 3.5 zooms in on the signal near the trigger threshold, showing voltage values in the samples immediately before and after ($\Delta t = 1ns$) threshold crossing.

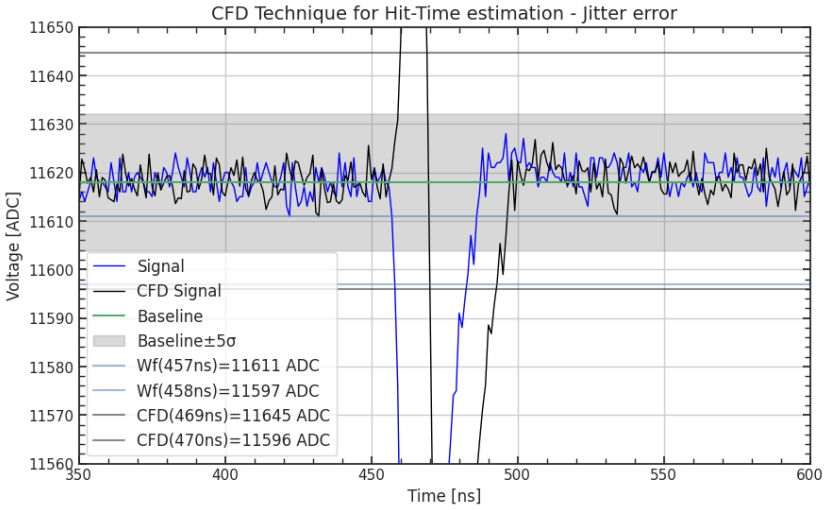


***Figure 3.5:*** *Threshold region comparison: Leading-Edge (blue) versus CFD (black) with 1 ns sampling intervals*

Numerical analysis confirms the CFD advantage:

$$\left|\frac{dV}{dt}\right|_{\text{LE}} \approx 14 \text{ ADC/ns} \quad \left|\frac{dV}{dt}\right|_{\text{CFD}} \approx 49 \text{ ADC/ns} \quad \Rightarrow \quad \sigma_{\text{jitter}}^{\text{LE}} \approx 0.21 \text{ ns} \quad \sigma_{\text{jitter}}^{\text{CFD}} \approx 0.06 \text{ ns} \tag{3.4}$$

yielding a 70% reduction in timing uncertainty through CFD processing with respect to Leading-Edge method.

### 3.2.2 ToF map

To study timing performance at the single-channel level, we must account for an additional variable that depends on the relative position of PMTs with respect to the Vertex: the ToF. In principle, for a fully filled detector with a laser source at its center, this contribution is an additive constant identical for all PMTs and, barring minor corrections, does not affect the shape of the TT distribution. In the hybrid configuration considered in this work - i.e., dynamic LS filling that varies run by run - it becomes necessary, given the different refractive indices of water and LS and therefore the different speeds of light in the two media, to compute the ToF based solely on the relative positions of PMTs and the interaction vertex, enabling the construction of a real-time ToF map independent of Monte Carlo (MC) simulations. This section provides an overview of the developed model, which accounts for light refraction phenomena from the laser source (or charged-particle interactions in the detector). This treatment will also support the development of a time-based vertex reconstruction algorithm (see Chapter 5).

A key distinction in constructing the map is whether the fired PMT and interaction vertex reside in the same medium or different media (i.e., traversing the Water-LS interface). For clarity, we define the Cartesian coordinates of the PMT as $(x_p, y_p, z_p)$ and the vertex as $(x_v, y_v, z_v)$, with the interface positioned at $z = h_{LS}$. All quantities are referenced to a Cartesian system centered on the CD. The refractive indices of LS and Water are denoted as $n_{LS}$ and $n_W$, respectively. For a schematic view of both cases and the relevant variables, see Fig. 3.6.

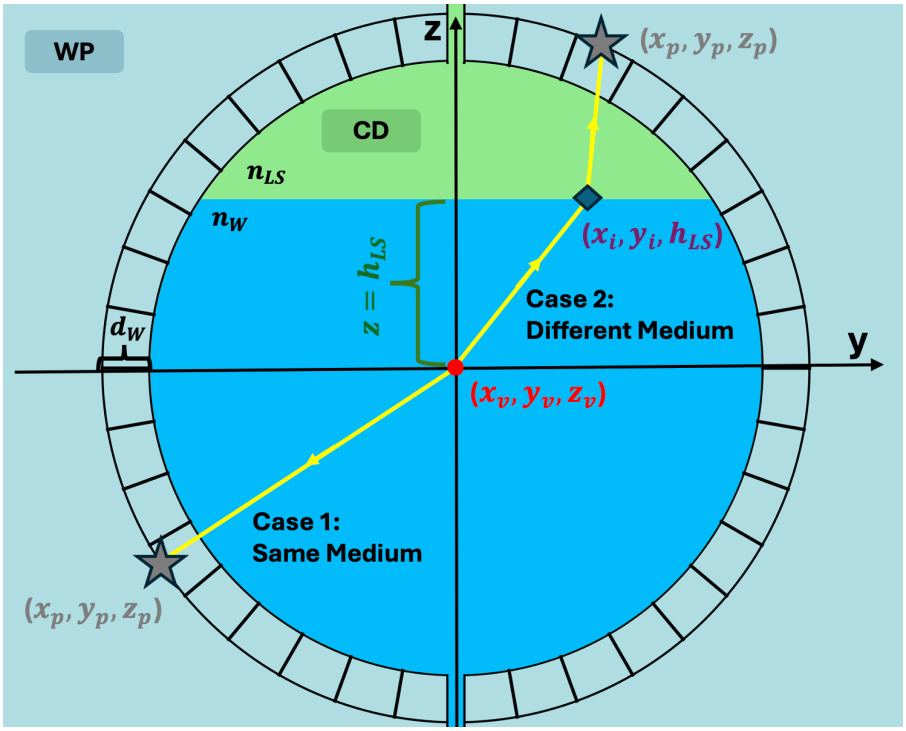


***Figure 3.6:*** *Diagram (not to scale) of the propagation of a photon from a vertex at coordinates $(x_v, y_v, z_v)$ to the PMT at coordinates $(x_p, y_p, z_p)$, with the variables of interest highlighted.*

#### Case 1: Same medium

This case occurs under two conditions:

$$\begin{cases} (z_v > h_{LS}) \ \& \ (z_p > h_{LS}) \Longrightarrow n_{medium} = n_{LS} = 1.57 \\ (z_v < h_{LS}) \ \& \ (z_p < h_{LS}) \Longrightarrow n_{medium} = n_W = 1.32 \end{cases} \tag{3.5}$$

Here, $n_{medium}$ represents the medium refractive index. The ToF is simply:

$$ToF(x_v, y_v, z_v | x_p, y_p, z_p) = \frac{\sqrt{(x_p - x_v)^2 + (y_p - y_v)^2 + (z_p - z_v)^2}}{c} \cdot n_{medium} - \Delta ToF(n_{medium}) \tag{3.6}$$

where $\Delta ToF(n)$ corrects for acrylic traversal (thickness $d_{acrylic} = 0.12\,\text{m}$, refractive index $n_{acrylic} = 1.4385$) and the water layer in front of each PMT (thickness $d_W = 1.42\,\text{m}$, refractive index $n_W$):

$$\Delta ToF(n) = \Delta ToF_{acrylic}(n) + \Delta ToF_{Water}(n) = \frac{d_{acrylic}}{c} \cdot (n - n_{acrylic}) + \frac{d_W}{c} \cdot (n - n_W) \tag{3.7}$$

Note that if the initial medium is Water, the correction reduces to acrylic traversal only.

#### Case 2: Different medium

The case involving traversal of the Water-LS interface requires a more careful treatment. It occurs when:

$$\begin{cases} (z_v < h_{LS}) \ \& \ (z_p > h_{LS}) \Longrightarrow n_1 = n_W \ , \ n_2 = n_{LS} \\ (z_v > h_{LS}) \ \& \ (z_p < h_{LS}) \Longrightarrow n_1 = n_{LS} \ , \ n_2 = n_W \end{cases} \tag{3.8}$$

To simplify subsequent relations, we introduce self-explanatory notation:

$$\begin{cases} (\Delta x_1, \Delta y_1, \Delta z_1) = (x_i - x_v, y_i - y_v, h_{LS} - z_v) \\ (\Delta x_2, \Delta y_2, \Delta z_2) = (x_p - x_i, y_p - y_i, z_p - h_{LS}) \end{cases} \Longrightarrow \begin{cases} \Delta r_1 = \sqrt{\Delta x_1^2 + \Delta y_1^2 + \Delta z_1^2} \\ \Delta r_2 = \sqrt{\Delta x_2^2 + \Delta y_2^2 + \Delta z_2^2} \end{cases} \tag{3.9}$$

Here, $(x_i, y_i)$ are the coordinates of the interface crossing point.
Due to interface traversal, the problem must account for both media, with the ToF given by:

$$ToF(x_v, y_v, z_v | x_p, y_p, z_p) = ToF_1(x_v, y_v, z_v | x_p, y_p, z_p) + ToF_2(x_v, y_v, z_v | x_p, y_p, z_p) \tag{3.10}$$

The two flight times depend not only on refractive indices but also on path lengths, which must incorporate refraction at the interface. Applying Snell's law (via Fermat's principle) to tangential components:

$$\vec{F}(x_i, y_i) = n_1 \sin(\theta_1) - n_2 \sin(\theta_2) = n_1 \cdot \frac{(\Delta x_1, \Delta y_1)}{\Delta r_1} - n_2 \cdot \frac{(\Delta x_2, \Delta y_2)}{\Delta r_2} = \begin{pmatrix} n_1 \cdot \frac{\Delta x_1}{\Delta r_1} - n_2 \cdot \frac{\Delta x_2}{\Delta r_2} \\ n_1 \cdot \frac{\Delta y_1}{\Delta r_1} - n_2 \cdot \frac{\Delta y_2}{\Delta r_2} \end{pmatrix} = \begin{pmatrix} 0 \\ 0 \end{pmatrix} \tag{3.11}$$

This system is solvable only numerically. Three solvers were implemented (Pros/cons and perfor-

mance of different methods are summarized in Table 3.1.):

- **Newton-Raphson:** This method is based on the iterative formula [46]:

$$\vec{x}^{(k+1)} = \vec{x}^{(k)} - J^{-1}(\vec{x}^{(k)}) \cdot \vec{F}(\vec{x}^{(k)}) \tag{3.12}$$

  Under the assumptions that $\vec{F} \in C^1$ in a neighborhood of the true value $\vec{x}^*$ and that the Jacobian $J(\vec{x}^*)$ is non-singular.

- **Levenberg-Marquardt:** This method is a refinement of Newton's method. The iterative formula is [47] [48]:

$$\vec{x}^{(k+1)} = \vec{x}^{(k)} - \vec{h} \tag{3.13}$$

  where $\vec{h}$ is obtained by solving the system:

$$(J^T J + \lambda I_{n\times n}) \cdot \vec{h} = -J^T \vec{F} \tag{3.14}$$

  with $\lambda$ being a damping parameter updated dynamically based on iteration success:

$$\begin{cases} \lambda^{(k+1)} = \frac{\lambda^{(k)}}{\nu} & \text{If:} \quad \|\vec{F}(\vec{x}^{(k+1)})\| < \|\vec{F}(\vec{x}^{(k)})\| \\ \lambda^{(k+1)} = \lambda^{(k)} \cdot \nu & \text{If:} \quad \|\vec{F}(\vec{x}^{(k+1)})\| > \|\vec{F}(\vec{x}^{(k)})\| \end{cases} \tag{3.15}$$

- **Broyden:** This method completely avoids analytical Jacobian computation, using instead an approximate form $B(\vec{x}^{(k)})$ starting from an initial guess (e.g., the identity matrix). The iterative formula is [49]:

$$\vec{x}^{(k+1)} = \vec{x}^{(k)} - B^{-1}(\vec{x}^{(k)}) \cdot \vec{F}(\vec{x}^{(k)}) \tag{3.16}$$

  while the approximate Jacobian update formula at each iteration is:

$$B^{(k+1)} = B^{(k)} + \frac{\left[\left(\vec{F}(\vec{x}^{(k+1)}) - \vec{F}(\vec{x}^{(k)})\right) - B^{(k)}(\vec{x}^{(k+1)} - \vec{x}^{(k)})\right] \cdot (\vec{x}^{(k+1)} - \vec{x}^{(k)})}{\|\vec{x}^{(k+1)} - \vec{x}^{(k)}\|^2} \tag{3.17}$$

| Method | Advantages | Limitations |
|---|---|---|
| **Newton-Raphson** | • Quadratic convergence near solution<br>• High precision results | • Requires Jacobian computation and inversion ($O(n^3)$ complexity)<br>• May diverge for poor starting points |
| **Levenberg-Marquardt** | • Robust performance far from solution | • Requires Jacobian computation<br>• Slower convergence than pure Newton |
| **Broyden's Method** | • Avoids explicit Jacobian calculations<br>• Lower computational cost per iteration | • Superlinear convergence<br>• Initial approximation $B^{(0)}$ affects performance |

***Table 3.1:*** *Comparative analysis of nonlinear system solution methods, highlighting computational characteristics and convergence properties.*

All methods require an initial guess for the crossing point, obtained as $(x_{guess}, y_{guess})$ along the vertex-PMT segment at the interface:

$$\begin{cases} x_{guess} = x_v + \frac{z_v - h_{LS}}{z_p - z_v} \cdot (x_p - x_v) \\ y_{guess} = y_v + \frac{z_v - h_{LS}}{z_p - z_v} \cdot (y_p - y_v) \end{cases} \tag{3.18}$$

For Newton-Raphson and Levenberg-Marquardt, the Jacobian estimate is:

$$J = \begin{pmatrix} J_{00} & J_{01} \\ J_{10} & J_{11} \end{pmatrix} = \begin{pmatrix} n_1 \cdot \frac{\Delta y_1^2 + \Delta z_1^2}{\Delta r_1^3} + n_2 \cdot \frac{\Delta y_2^2 + \Delta z_2^2}{\Delta r_2^3} & -n_1 \cdot \frac{\Delta x_1 + \Delta y_1}{\Delta r_1^3} - n_2 \cdot \frac{\Delta x_2 + \Delta y_2}{\Delta r_2^3} \\ -n_1 \cdot \frac{\Delta x_1 + \Delta y_1}{\Delta r_1^3} - n_2 \cdot \frac{\Delta x_2 + \Delta y_2}{\Delta r_2^3} & n_1 \cdot \frac{\Delta x_1^2 + \Delta z_1^2}{\Delta r_1^3} + n_2 \cdot \frac{\Delta x_2^2 + \Delta z_2^2}{\Delta r_2^3} \end{pmatrix} \tag{3.19}$$

After numerical resolution of the system (with defined tolerance and max iterations), the optimal $(x_i, y_i)$ yields the ToF:

$$ToF(x_v, y_v, z_v | x_p, y_p, z_p) = \frac{\Delta r_1}{c} \cdot n_1 + \frac{\Delta r_2}{c} \cdot n_2 - \Delta ToF(n_2) \tag{3.20}$$

where $\Delta ToF(n_2)$ follows Eq. 3.7.

### Method validation and MC comparison

In summary, for a Cartesian system centered on the CD, given a vertex at $(x_v, y_v, z_v)$, a PMT at $(x_p, y_p, z_p)$, and interface height $h_{LS}$, the ToF map is:

$$\begin{cases} \frac{\sqrt{(x_p-x_v)^2+(y_p-y_v)^2+(z_p-z_v)^2}}{c} \cdot n_{medium} - \Delta ToF(n_{medium}) & \text{If: } \begin{cases} (z_v > h_{LS}) \;\&\; (z_p > h_{LS}) \Longrightarrow n_{medium} = n_{LS} \\ (z_v < h_{LS}) \;\&\; (z_p < h_{LS}) \Longrightarrow n_{medium} = n_W \end{cases} \\ \frac{\Delta r_1}{c} \cdot n_1 + \frac{\Delta r_2}{c} \cdot n_2 - \Delta ToF(n_2) & \text{If: } \begin{cases} (z_v < h_{LS}) \;\&\; (z_p > h_{LS}) \Longrightarrow n_1 = n_W \;,\; n_2 = n_{LS} \\ (z_v > h_{LS}) \;\&\; (z_p < h_{LS}) \Longrightarrow n_1 = n_{LS} \;,\; n_2 = n_W \end{cases} \end{cases} \tag{3.21}$$

with $(x_i, y_i)$ estimated numerically and $\Delta ToF(n)$ from Eq. 3.7.
Figure 3.7 shows ToF maps for vertices in two positions: LS (Fig. 3.7a) and Water (Fig. 3.7b).

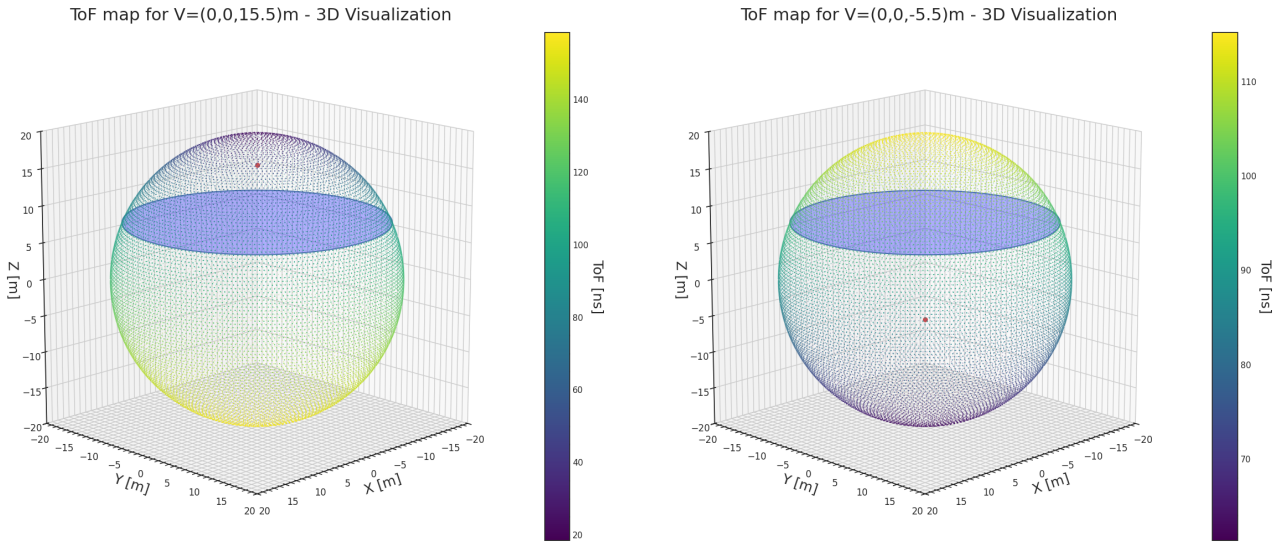


***(a)*** *Three-dimensional distribution of the ToF map obtained through numerical computation. The interaction vertex is shown in red (at $z = 15.5\,m$), and the Water-LS interface is shown in blue.*

***(b)*** *Three-dimensional distribution of the ToF map obtained through numerical computation. The interaction vertex is shown in red (at $z = -5.5\,m$), and the Water-LS interface is shown in blue.*

***Figure 3.7:*** *Numerically computed ToF maps for two different interaction vertex positions.*

To validate the model, JUNO MC simulations were used, with a vertex at the origin (matching laser runs). Figure 3.8 compares numerical and MC ToF values in 3D (Fig. 3.8a) and angular projections (Fig. 3.8b).

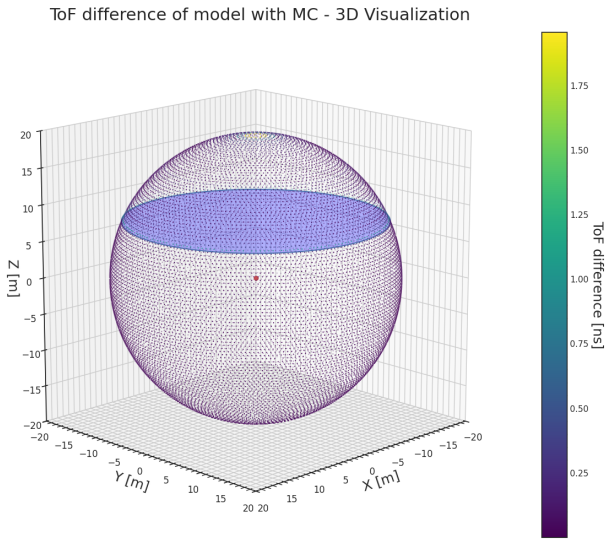


***(a)*** *Three-dimensional distribution of the absolute difference in ToF values obtained, PMT by PMT, from MC simulation and numerical computation. The interaction vertex is shown in red (center of the detector), and the Water-LS interface is shown in blue.*

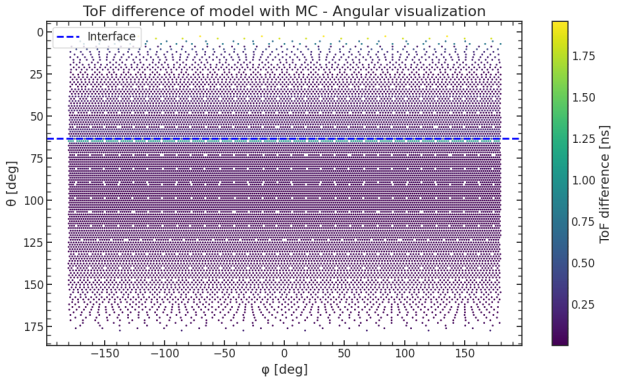


***(b)*** *Two-dimensional angular distribution $(\theta, \phi)$ of the absolute difference in ToF values obtained, PMT by PMT, from MC simulation and numerical computation. The Water-LS interface is shown in blue.*

***Figure 3.8:*** *Comparison between MC-simulated and numerically computed ToF values.*

The best agreement is achieved with the combination $(n_{LS}, n_W)$=(1.57, 1.32), consistent with values reported in literature [50]. A small number of outliers (i.e., PMTs whose ToF disagrees with MC) are localized in two regions: (i) near the Water-LS interface and (ii) the ring closest to the sphere's north pole. The former results from non-convergence of numerical methods for PMTs near the interface, while the latter is due to the different radial position of PMTs close to the north pole. Nevertheless, the model agrees with MC within 1 ns for interface PMTs and within 2 ns for north pole PMTs. This numerical method will be used hereafter for constructing ToF maps.

### 3.2.3 Reference time ($t_0$) extraction and JUNO laser system

Before delving into the extraction of the reference time $t_0$, it is necessary to introduce a brief section describing the laser system in JUNO.

#### JUNO Laser System

The best way to describe the laser system in JUNO is to start from the technical requirements defined during the design phase and explain how each of them is concretely implemented. JUNO laser system requirements [51]:

1. **Pulsed beam with timing resolution < 1 n and dynamic range equivalent to deposited energies from hundreds of keV to a few TeV:** To satisfy both requirements, it was selected the laser model FQSS266-Q4-1k-STA, a diode-pumped, passively Q-switched solid-state laser based on a microchip with multiple frequency conversion stages. The laser pulses (width less than 1 ns) can be driven internally with a repetition rate between 1 to 1000 Hz. The laser is enclosed in

an aluminum box, and heat dissipation from the laser head is achieved via thermal conduction through a base plate. The maximum output energy is 15 $\mu$J per pulse.

2. **Isotropic light emission in all directions:** Fulfilled by attaching a Polytetrafluoroethylene (PTFE) diffuser ball to the open end of the optical fiber with a diameter of 15 mm. Measurements confirmed that the laser wavelength remains unchanged after diffusion. The best uniformity was achieved with an insertion depth of 6.5 mm. The variation in the angular distribution of the light intensity in the detection area is approximately 15%.

3. **Photon production with wavelength and time structure similar to real physical events:** To mimic real events, a laser with Ultra Violet (UV) wavelength is used (with *lambda* less than 310 nm). Its photons are rapidly absorbed in the LS and subsequently re-emitted isotropically at a blue wavelength.

4. **Sub-percent precision in relative laser intensity in the 1–8 MeV anti-neutrino energy range:** The internal power meter of the laser does not offer the required precision. As a solution, the laser beam is split: one part is sent into the detector, while the other illuminates a dedicated monitoring device (hereinafter referred as "Monitor PMT") — a 1-inch Hamamatsu R8520-406 PMT with excellent linearity and TT jitter below 0.8 ns.

5. **Deployability along the central axis of the JUNO detector:** To meet this requirement, the photons are transmitted via a shielded optical fiber deployable through a precisely controlled spool system. The fiber must transmit UV light, be thin and flexible enough to be spooled precisely, emit photons only through its open end, and be chemically compatible with the LS. Were selected custom-made multi-mode fibers with a core diameter of 200 $\mu$m and an outer diameter of 1.5 mm. The total light leakage through a 50 m fiber was measured to be less than 0.1%.

#### Reference time $t_0$ extraction

A critical timing consideration involves the synchronization between the laser trigger and the CTU clock cycle. The CTU operates with an 8 ns clock period, which serves as the fundamental timing reference for all GCU waveform recordings. Without proper offline correction, the inherent jitter between the laser trigger and CTU clock edges can introduce temporal smearing of up to 8 ns in the PMT Hit Time distributions, effectively limiting the timing resolution to the clock period. To mitigate this effect, two complementary correction methods were implemented (the synchronization challenge and correction scheme are illustrated schematically in Figure 3.9.):

(i) Event-by-event jitter extraction using the high-precision Monitor PMT positioned downstream of the laser beam splitter, with waveform stored in a dedicated GCU;

(ii) Utilization of a Calibration Interface Box (CIB) module to acquire timing information from a Transistor-Transistor Logic (TTL) signal derived from the Monitor PMT output via Nuclear Instrument Module (NIM)-to-TTL conversion through a fast discriminator.

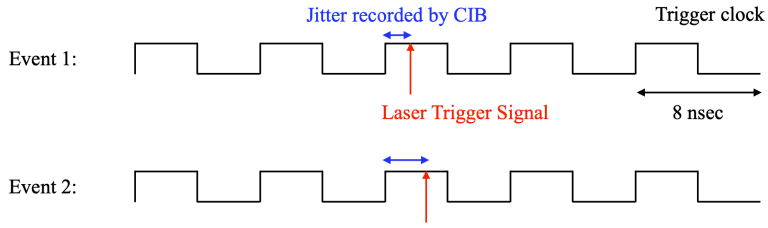


***Figure 3.9:*** *Schematic representation of the laser trigger timing not being synchronized (i.e., jitter error) with the trigger clock timing in the CTU. The Laser Trigger Signal is shown in red, the Trigger Clock in black, and the correction to the jitter error recorded by the CIB in blue.*

## 3.3 PMT TIMING MODEL AND SYNCHRONIZATION PERFORMANCES

Once the TT values are obtained event-by-event and PMT-by-PMT, the next step is to parameterize their distribution across an entire laser run to extract physically meaningful information about PMT timing synchronization and performance. A suitable model for describing the TT distribution of a single PMT is the convolution of a Gaussian with an exponential, plus a background component dependent on the number of detected events (parameterizing the Dark Noise (DN)):

$$f_{S+D}(t) = C \cdot f_S(t) + f_D(t) = C \cdot \left[ \frac{\alpha}{2\tau} \cdot e^{\frac{2\mu + \frac{\sigma^2}{\tau} - 2t}{2\tau}} \cdot \operatorname{erfc}\left( \frac{\mu + \frac{\sigma^2}{\tau} - t}{\sqrt{2}\sigma} \right) \right] + \left[ (bkg_1 - bkg_2) \cdot \left( 1 - \int_{t_{start}}^{t} f_S(t')dt' \right) + bkg_2 \right] \tag{3.22}$$

The fit parameters were extracted by maximizing the Poissonian likelihood of this model against experimental data. Figure 3.10 shows an example of the fit applied to data from a Hamamatsu Dynode PMT and an NNVT MCP PMT.

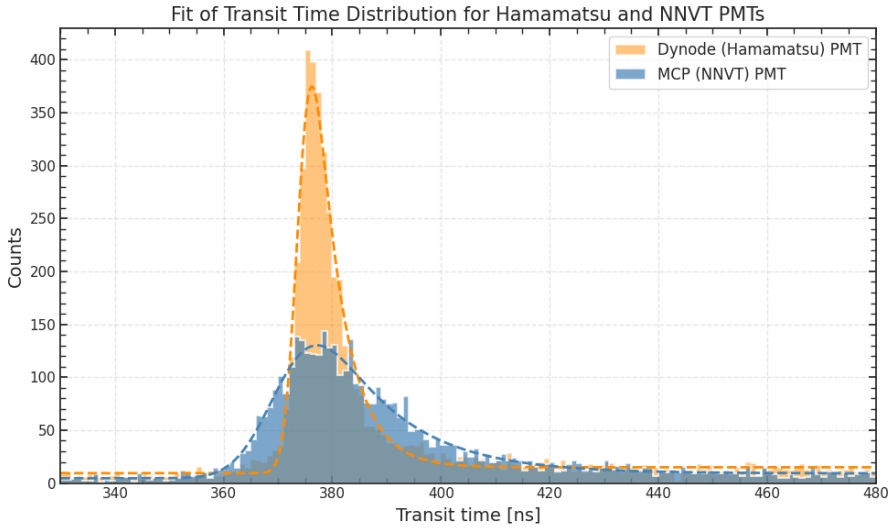


***Figure 3.10:*** *Transit time distribution for a Hamamatsu PMT (yellow) and a NNVT PMT (blue), with the fit based on the model defined by Equation 3.22 overlaid.*

A clear difference is observed in the width of the two distributions: when a photocathode is fully

illuminated with single photons, the TT of each PE pulse exhibits fluctuations, quantified as the TTS [52]. This parameter is extracted from the distributions for each PMT, and Figure 3.11 shows the TTS distributions for all PMTs (Dynode and MCP).

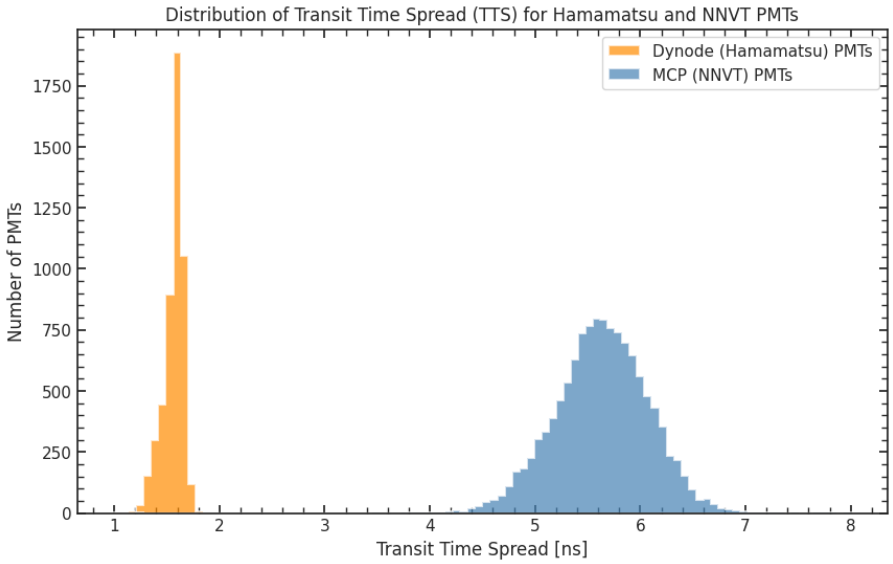


***Figure 3.11:*** *Distribution of the TTS, extracted as $\sigma_{TTS}$ from the fit using the model defined by Equation 3.22, for all PMTs, separated into Hamamatsu (yellow) and NNVT (blue).*

Concluding with an examination of the observed TTS distributions, we can focus on three distinctive features: their asymmetric shape, differing widths, and displaced centroid positions.

- The asymmetric profile arises from the non-Gaussian nature of the physical processes underlying the operation of the PMT. In particular, the exponential tail is due to late pulses [53], which consist of photoelectrons that are in-elastically backscattered from the first dynode and subsequently produce secondary electrons after being reaccelerated by the acceleration structure.
- The noticeable difference in distribution widths can be attributed to two primary factors: (i) in MCPs, electrons follow substantially longer and more randomized paths through the microchannels, and (ii) the continuous multiplication medium generates greater statistical noise compared to the discrete dynode stages found in conventional PMTs.
- The centroid displacement between the distributions depends on their propagation mechanisms. MCPs have a larger average transit time due to the fact that the electrons travel longer effective paths in the curved or irregular microchannels and secondary electrons bouncing multiple times within narrow pores before exiting. While Dynode chains are optimized for fast linear acceleration and amplification, with shorter average electron paths.

### 3.3.1 Synchronization performances

To verify timing stability over time and ensure the PTP procedure properly synchronizes GCU units, it was performed a differential analysis using three 420nm laser calibration runs with the source positioned at the CD center: Run4908 (first) and Run5060 (second) were taken weeks apart, with GCU hard-reset operations between them; Run5061 (third) was taken immediately after Run5060 following PTP synchronization. We expect to observe at least a correction in GCU timing synchronization shifts after PTP, with any residual desynchronization confined within a single clock cycle (i.e., 8ns).
Using the fit model from Eq. 3.22, we extracted the most probable TT value for each PMT per run as the distribution peak. This allows differential comparison of centroid shifts between runs at the single-channel level. Figure 3.12 shows the offset distribution between the first two runs (pre- and post-GCU hard reset).

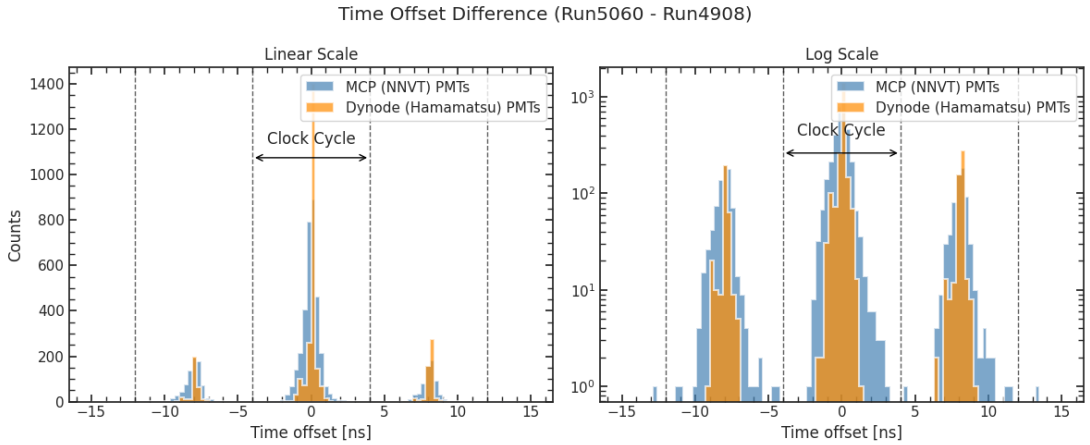


***Figure 3.12:*** *Distribution of time offsets (per PMT) between two runs following GCU hard reset, comparing Hamamatsu (yellow) and NNVT (blue) PMTs. Linear (left) and logarithmic (right) scales are shown.*

A significant population of PMTs appears at $\pm 8ns$ (desynchronized by one clock cycle). Figure 3.13 shows the equivalent comparison immediately before/after PTP synchronization.

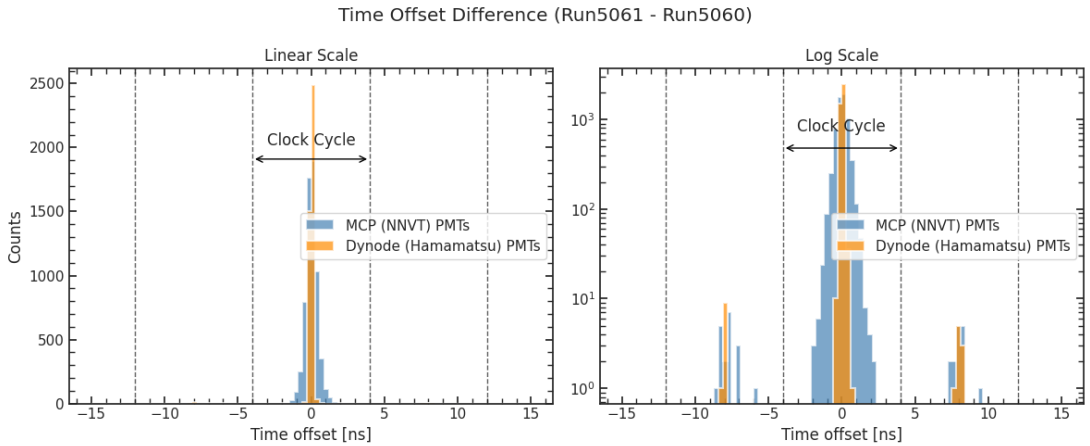


***Figure 3.13:*** *Distribution of time offsets (per PMT) between runs pre-/post-PTP, comparing Hamamatsu (yellow) and NNVT (blue) PMTs. Linear (left) and logarithmic (right) scales are shown.*

The number of asynchronized PMTs decreases dramatically. To confirm whether shifted PMT populations belonged to the same GCU, Figure 3.14 shows channel distributions for shifted PMTs in both comparisons. The uniform distribution in both cases (validated by deeper analysis) confirms GCU-level rather than channel-specific shifts. This analysis was repeated monthly during commissioning to monitor temporal synchronization, ensuring proper detector operation.

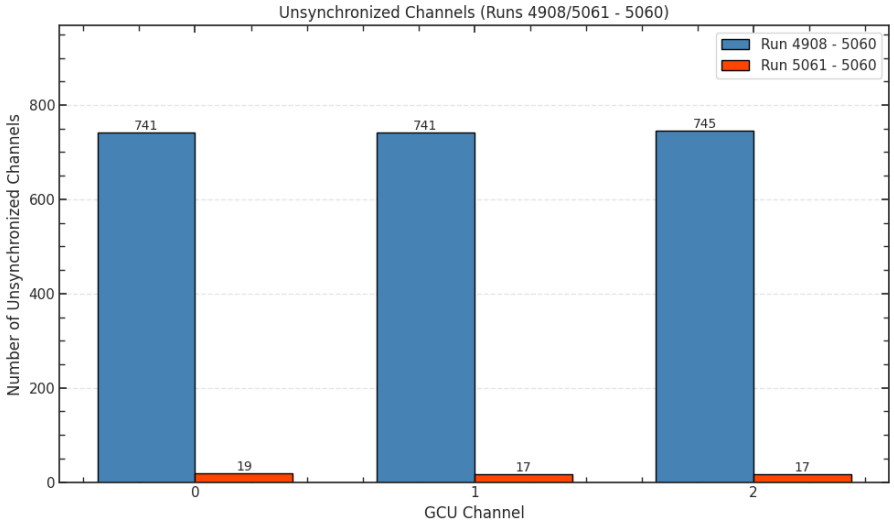


***Figure 3.14:*** *Channel distribution of unsynchronized PMTs (offset by one clock cycle) post-GCU reset (blue) and post-PTP (red).*

# 4

# Event Selection and radiopurity monitoring

As previously introduced, one of the primary goals of JUNO is to determine the NMO within the first six years of operation. To achieve this, JUNO detects electron antineutrinos emitted by eight NPP located at an average baseline of 52 km, via the IBD reaction: this reaction has a characteristic signature consisting of a prompt signal (two 511 keV photons from positron annihilation) followed by a delayed signal (a 2.22 MeV photon from neutron capture on hydrogen). The development of a reliable event selection algorithm to identify IBD correlated candidates against a background of uncorrelated events is therefore of critical importance.

In this chapter, both the expected signal and background in JUNO will be introduced, with a particular focus on backgrounds originating from natural radioactivity. An event selection algorithm will be presented, designed to optimize the balance between high efficiency (achieved through loose selection cuts) and high purity (enabled by a high-statistics background estimation) of the resulting sample. This algorithm will be applied to the tagging of fast coincidences from the $\beta$-decay of $^{214}$Bi followed by the $\alpha$-decay of $^{214}$Po, with the aim of monitoring the radiopurity of the LS used in JUNO by measuring the contamination from $^{238}$U. This isotope is one of the main internal radiogenic backgrounds that can significantly compromise JUNO's sensitivity to its physics goals. For this reason, the collaboration has set an upper limit on the $^{238}$U contamination at $10^{-15}$ g/g for IBD-level analyses, and $10^{-16}$–$10^{-17}$ g/g for solar-level analyses.

The chapter will conclude by introducing a further application of the selection algorithm, targeting another source of background: spallation neutrons produced by the passage of cosmic muons. These events are of particular physical interest, as they closely mimic delayed IBD-like signals, with a characteristic energy peak at 2.2 MeV. These events will be tagged, their energy distribution will be presented, and a preliminary estimate of the JUNO energy resolution will be provided, as part of the necessary analyses during this commissioning phase.

## 4.1 Expected signal and background in JUNO

The purpose of this section is to provide an overview of the signals observed by JUNO for the detection of reactor antineutrinos (via the IBD reaction), as well as the main background sources that may affect the measurement precision. Particular attention will be given to the background induced by natural radioactivity, which significantly impacts JUNO's sensitivity to the extraction of solar neutrino parameters.

### 4.1.1 Signal and backgrounds in JUNO

Reactor antineutrinos in JUNO are detected through the IBD reaction

$$\bar{\nu}_e + p \longrightarrow e^+ + n \tag{4.1}$$

The kinetic energy deposited by the positron via ionisation, together with its subsequent annihilation into typically two 0.511 MeV photons, forms a prompt signal. The impinging neutrino transfers most of its energy to the positron which readily annihilates. This allows the deposited visible energy of the positron to be directly and related to the antineutrino energy $E_{\bar{\nu}_e} \approx E_{e^+} + 0.8MeV$, which is the relevant metric for neutrino oscillation measurements. The neutron is captured after an average time of $\approx 220\,\mu s$, and the corresponding photon emission - correlated in space and time with the positrons - forms a delayed signal. The neutron is predominantly captured on hydrogen ($\approx 99\%$), releasing a single 2.2 MeV photon, and with lower probability on carbon ($\approx 1\%$), yielding a gamma-ray signal with 4.9 MeV of total energy. A schematic view of the IBD is shown in Figure 4.1. A more detailed description of IBD kinematics is reported in Appendix A.

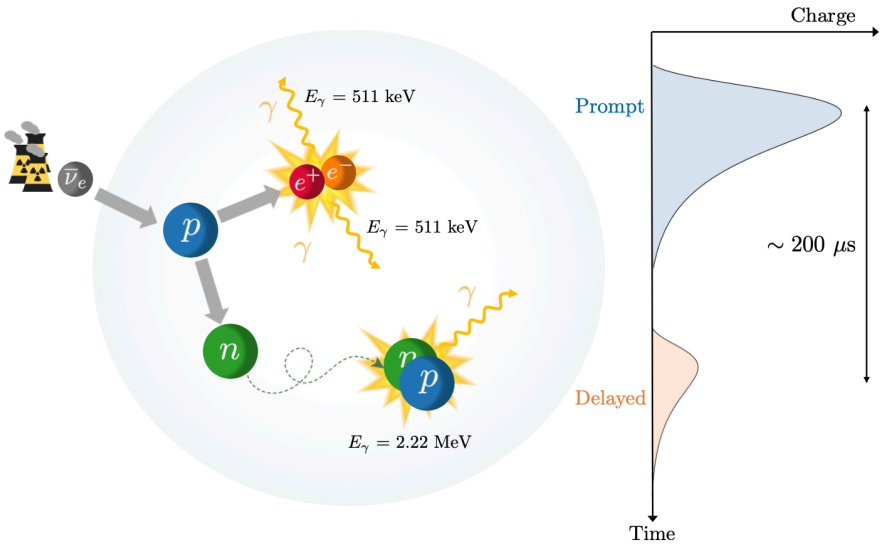


***Figure 4.1:*** *Schematic illustration of an IBD reaction in the LS. The electron antineutrino interacts with a proton (p) in the LS, creating a positron ($e^+$) and a neutron (n). The positron deposits its energy and annihilates into two 0.511 MeV photons ($\gamma$), producing a prompt signal. After a random walk, the neutron is captured mainly by a free proton in the LS, emitting a 2.22 MeV $\gamma$-ray, and giving rise to a delayed signal. The time-charge diagram is not in scale. From [54].*

The IBD prompt-delayed spatial and temporal coincidence signature can be mimicked by other events in the detector, giving rise to backgrounds. After applying the IBD selection, about 10% of the IBD candidates are background events, which can be categorized into seven groups [40]:

1. **Accidental background:** Caused by the coincidence of two uncorrelated events. The prompt-like signals primarily originate from radiogenic events (i.e., $\alpha, \beta, \gamma$ decays from natural radioactivity in the detector materials and surrounding environment), while the delayed-like signals mainly result from radiogenic events and spallation neutrons produced by cosmic muons.

2. **$^{9}$Li and $^{8}$He:** Muons passing through the detector can produce the long-lived cosmogenic isotopes $^{9}$Li and $^{8}$He, whose correlated $\beta$–n decays haave decay times and energy that can mimic the IBD signature.

3. **Fast neutrons:** Produced by energetic neutrons generated by cosmic muons. These neutrons scatter off protons (creating the prompt-like signal) and are subsequently captured (producing the delayed-like signal), thus imitating the IBD event. Due to the relatively short neutron capture time, most fast neutrons can be efficiently rejected by applying a time window after muon tagging. However, some may escape this veto if their parent muons traverse only the surrounding rock.

4. **$^{13}$C($\alpha$,n)$^{16}$O background:** Arises from interactions of $\alpha$ particles (from natural radioactivity) with $^{13}$C nuclei in the LS. Radiation from the excited $^{16}$O mimics the IBD prompt signal, while the capture of the emitted neutron reproduces the delayed signature.

5. **Atmospheric neutrinos:** Produced by interactions of primary cosmic rays with the Earth's atmosphere. These neutrinos, of all flavors, interact with nuclei in the JUNO detector via charged or neutral current processes. Refs. [55] and [56] indicate that neutral current interactions can result in final states that mimic correlated backgrounds.

6. **Electron antineutrinos from distant (>300 km) reactors:** Antineutrinos originating from reactors located more than 300 km away are effectively IBD signals but are considered background, as they do not contribute to the NMO sensitivity and determination of oscillation parameters.

7. **Geoneutrinos:** Electron antineutrinos produced by the radioactive decay chains of uranium and thorium within the Earth. As far reactors, these are true and irreducible IBD interactions.

The seven categories of backgrounds are listed in Table 4.1, along with their respective rate and spectral shape uncertainties. The reconstructed energy spectrum (for both the NO and IO scenarios), together with the various background contributions, is shown in Figure 4.2.

| **Quantity** | Rate [day$^{-1}$] | B/S [%] | Rate unc. [%] | Shape unc. [%] |
|---|---|---|---|---|
| Geoneutrinos | 1.2 | 2.5% | 30% | 5% |
| World reactors | 1.0 | 2.1% | 2% | 5% |
| Accidentals | 0.8 | 1.7% | 1% | negligible |
| $^{9}$Li/$^{8}$He | 0.8 | 1.7% | 20% | 10% |
| Atmospheric $\nu$ | 0.16 | 0.34% | 50% | 50% |
| Fast neutrons | 0.1 | 0.21% | 100% | 20% |
| $^{13}$C$(\alpha, n)^{16}$O | 0.05 | 0.01% | 50% | 50% |
| **Total backgrounds** | 4.11 | 8.7% | | |

***Table 4.1:*** *Expected background rates, background to signal ratio (B/S), and rate and shape uncertainties.*

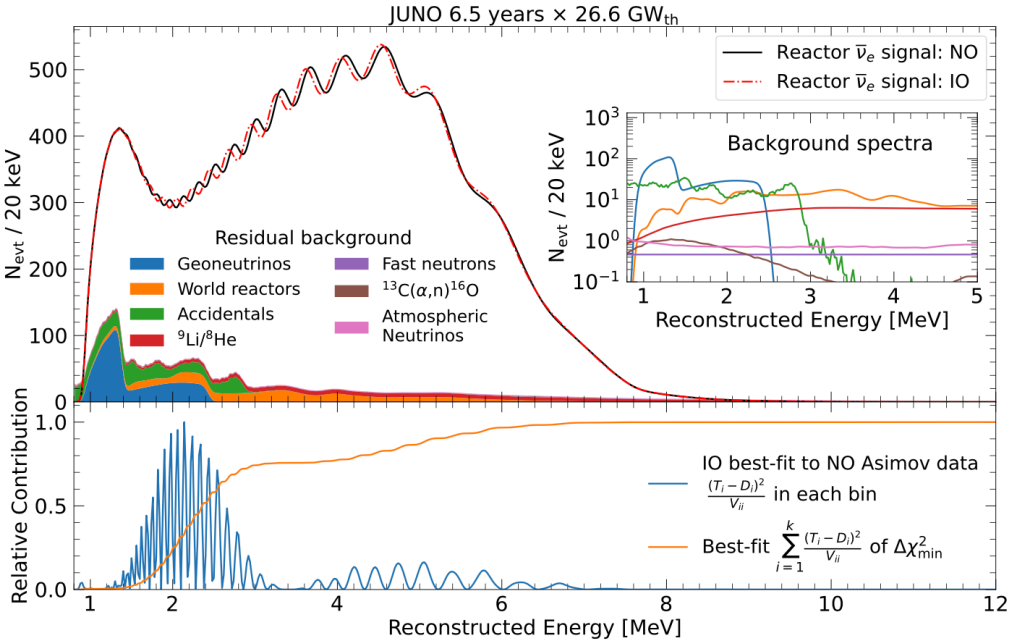


***Figure 4.2: Top:*** *Reconstructed energy spectra of JUNO in both the NO and IO scenarios without any statistical or systematic fluctuations (Asimov data). The neutrino oscillation parameters from Particle Data Group (PDG) 2020 [1] are used to calculate the oscillation probability. The background spectra in the main figure are stacked, whereas those in the inset are plotted individually.* ***Bottom:*** *Relative contribution to $\Delta\chi^2$ and cumulative $\Delta\chi^2$ obtained when fitting the IO spectrum with the NO hypothesis. The results show that the most sensitive region for JUNO's NMO determination is 1.5–3 MeV. Taken from [40].*

The unique prompt-delayed temporal and spatial coincidence signature of IBD events provides an effective handle for rejecting background events. A fiducial volume cut on the LS target is applied to further suppress backgrounds from natural radioactivity originating from the PMTs and other materials outside the LS region. In addition, cosmic muon veto cuts are used to suppress cosmogenic backgrounds induced by muons traversing the detector. As a result, the IBD selection dramatically reduces the background-to-signal ratio from the order of 150 Hz in the raw experimental data to below 0.8 counts/day in the final selected IBD candidates [38].

Accidental backgrounds from natural radioactivity can mimic IBD signatures within the same energy range and cannot be further rejected by software-based cuts. Therefore, despite the prompt-delayed coincidence correlations in energy, time, and position, maintaining an extremely low level of natural radioactivity is essential. This is achieved through a strict radiopurity control strategy during detector design and construction. The detection of solar neutrinos, by contrast, relies solely on the observation of elastic scattering off electrons in the detector medium. Only a fraction of the neutrino energy is transferred to the electron, resulting in a continuous recoil spectrum even for mono-energetic incident neutrinos. The lack of a coincidence signature in this case imposes even stricter requirements on the background levels in the sub-20 MeV energy region. More deails on solar neutrino detection can be found in Appendix B.

### 4.1.2 Natural Radioactivity

Natural radioactivity [57] is ubiquitous and can only be mitigated through stringent material screening and LS radiopurity control. The water shielding surrounding the central detector is effective not only against fast neutrons produced by muons, but also against radioactivity from the rock at the JUNO site. With deposited energies up to 5 MeV, which overlap with the IBD energy spectrum, the radioactivity of detector materials is a major source of accidental background. The main contributors are:

- Naturally occurring long-lived radionuclides: $^{238}$U and $^{232}$Th (assumed in secular equilibrium), and $^{40}$K;
- Medium-lived radionuclides such as $^{226}$Ra, $^{210}$Pb/$^{210}$Bi, and $^{210}$Po, which become significant when secular equilibrium is broken in the $^{238}$U chain;
- Gaseous radionuclide $^{222}$Rn and anthropogenic radionuclide $^{60}$Co.

All these contaminants may be present in the various materials of the JUNO detector and its LS and contribute to the singles rate in the CD via their radioactive decays. Depending on energy and timing, they may mimic either the prompt or delayed event in an IBD reaction. The expected IBD rate in the CD is about 60 events per day, while the singles rate from natural radioactivity must be reduced to below 10 counts per second, corresponding to ≈1 accidental coincidence per day under standard antineutrino selection cuts [57]. This level is comparable to that from backgrounds such as $^{8}$He/$^{9}$Li and geoneutrinos. For solar neutrino detection, where the signal consists of a single event, background requirements are far more stringent. This is addressed through tighter Fiducial Volume (FV) and timing cuts to suppress both natural and cosmogenic backgrounds. External material radioactivity can also be efficiently suppressed by applying FV and energy threshold cuts in software. It is also important to distinguish between internal and external backgrounds:

- **Internal:** In the case of internal backgrounds, radionuclides (especially from U/Th chains) release their decay energy directly within the sensitive volume, regardless of the type of emitted particles. Assuming secular equilibrium, each radionuclide contributes equally to the singles rate (neglecting energy thresholds). Thus, FV cuts are ineffective, since these backgrounds are uniformly distributed within the LS.

- **External:** For external backgrounds, only a subset of radionuclides is relevant, as $\alpha$ and $\beta$ particles have very short ranges in solid materials. Only high-energy $\gamma$-rays can penetrate into the LS and deposit energy. These predominantly originate from $^{214}$Bi (1.76 and 2.20 MeV in the $^{238}$U chain), $^{208}$Tl (2.61 MeV in the $^{232}$Th chain), $^{40}$K (1.46 MeV), and $^{60}$Co (1.17 and 1.33 MeV).

- **Both internal and external:**

  - Radon ($^{222}$Rn), a gaseous product of the $^{238}$U chain, is particularly problematic as it contributes to both internal and external backgrounds. The LS may be contaminated by radon during production, transport, or storage through exposure to air or emanation from materials. This leads to internal contamination from long-lived isotopes such as $^{210}$Pb and its decay chain $^{210}$Bi/$^{210}$Po, and potentially external contamination if progenitor $^{214}$Bi is present in the inner water pool.

  - ($\alpha$,n) reactions may also occur in the LS or surrounding materials due to U/Th impurities. However, their contribution to the singles rate is expected to be much smaller due to their relatively low cross sections.

It is therefore clear that strict upper limits must be imposed on the contamination levels of the LS by uranium and thorium chain elements [12]: $\leq 10^{-15}$ g/g for IBD-based physics analyses, and $\leq 10^{-16}$–$10^{-17}$ g/g for the solar neutrino program. The purpose of this work falls within the context of the commissioning activities, in particular during the extended phase of replacing water with LS. In next section, the monitoring of the radiopurity of the LS introduced daily into JUNO will be discussed, focusing on verifying that the concentration of $^{238}$U meets the requirements set by the collaboration.

## 4.2 Event selection algorithm and LS Radiopurity Monitoring

The aim of this section is to present the analysis carried out during the commissioning phase, focusing on the real-time monitoring of the radiopurity of the LS injected daily into JUNO. During the LS filling months, data were collected in Runs labeled with different Tags, indicating the purpose of the run (e.g., "Physics", "LS-Filling", "Calibration", etc.). The analysis presented here considers only Runs tagged as "LS-Filling" and "Physics" with a duration longer than one hour, to ensure sufficient statistics. This analysis was performed in real-time throughout the period from mid March to mid May 2025.

In a LS detector, the most sensitive direct method to determine the abundance of $^{238}$U is based on tagging the fast coincidence between the $\beta$-decay of $^{214}$Bi and the subsequent $\alpha$-decay of $^{214}$Po, hereinafter referred to as "BiPo". Due to the short lifetime of the polonium isotope ($\tau_{^{214}Po} = 237\,\mu s$), this double-event signature -very similar to the IBD interaction - allows for effective rejection of single-event backgrounds. Assuming secular equilibrium, the observed BiPo rate can be directly converted into the mass abundance of $^{238}$U. The full $^{238}$U decay chain is shown in Fig. 4.3.

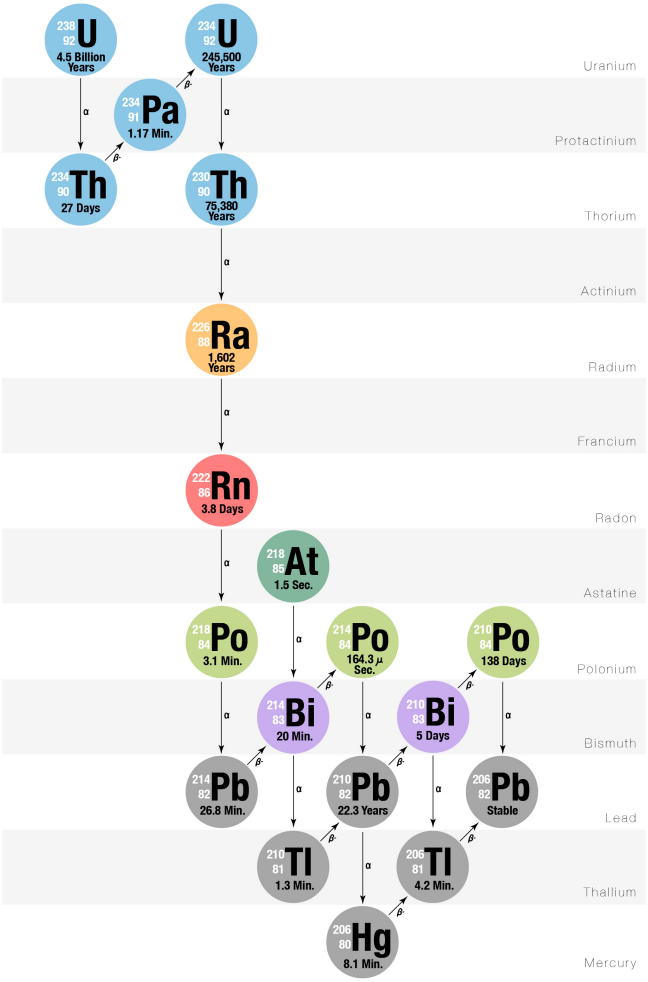


***Figure 4.3:*** *Decay chain of $^{238}U$, with the type of decay highlighted. The numbers below each label indicate the half-life of the corresponding radionuclide.*

BiPo event selection is based on a set of cuts applied to specific variables, such as the time and spatial difference between events or energy thresholds. At this stage of the experiment, not all these variables are fully reliable. The cuts considered are the following:

- **Time cut $\Delta t$:** Given the very short lifetimes of 237 $\mu$s for $^{214}$Po, most single-event backgrounds can be rejected by requiring a short delay $\Delta t$ between the prompt and delayed signals. This is a robust variable, independent of reconstruction, and is therefore used in the analysis.
- **Distance cut $\Delta R$:** Due to the low recoil energies and short time intervals, both Bi and Po decays occur nearly at the same position. However, this cut is the least robust, as it strongly depends on vertex reconstruction, yet not properlly tuned aand tested in this commissioning phase.
- **Energy selection:** Bismuth $\beta$-decays have a broad energy spectrum, while polonium $\alpha$-decays are mono-energetic. This variable is robust when expressed in terms of photoelectrons (PE), i.e., total charge, but less so in MeV due to strong dependence on energy reconstruction and lack of comprehensive calibrations. For this reason, energy is expressed in PE, assuming a linear correlation with charge.

### 4.2.1 Correlation Studies with the Off-Window Technique

Once the cut variables for BiPo selection are identified, the next step is to define their limits. Two main approaches exist:

- **Strict cuts:** Applying tight cuts to the selection variables leads to a highly pure BiPo sample, at the cost of low selection efficiency.
- **Loose cuts:** Applying broader cuts improves selection efficiency, making it more robust and independent of changes (e.g., HV fluctuations, channel drops, energy scale). However, this results in a low-purity sample with significant background contamination, which must be subtracted using independent information.

The approach adopted in this thesis is a compromise between these two extremes. The strategy is as follows:

1. **Muon veto:** To remove events from muons and subsequent cosmogenic products, a simple muon veto is applied. Muon events are identified as high-energy events ($E_\mu > 50'000$ pe), and all events within a subsequent time window $\Delta t_{veto} = 2$ ms are vetoed.
2. **On-window:** Once a $^{214}$Bi $\beta$-decay event (prompt) is identified, all subsequent events within a time window $\Delta t_{On} = 5 \cdot \tau_{^{214}Po}$ are selected. This results in a sample that contains both correlated BiPo signals and a large background of uncorrelated coincidences.
3. **Off-window:** For the same identified prompt event, the time window is shifted by an offset $t_{offset} = 20 \cdot \tau_{^{214}Po}$, and widened to $\Delta t_{Off} = k \cdot \Delta t_{On}$, with a scale factor $k = 200$. Assuming that uncorrelated background coincidences are randomly distributed in time, the background event distribution remains unchanged even after the shift. This allows for a high-statistics estimation of the background.
4. **Subtraction:** Finally, a statistical subtraction of the two samples is performed, normalized by the number of entries. This yields a clean sample of truly correlated prompt-delayed coincidences.

A schematic representation of this algorithm is shown in Fig. 4.4.

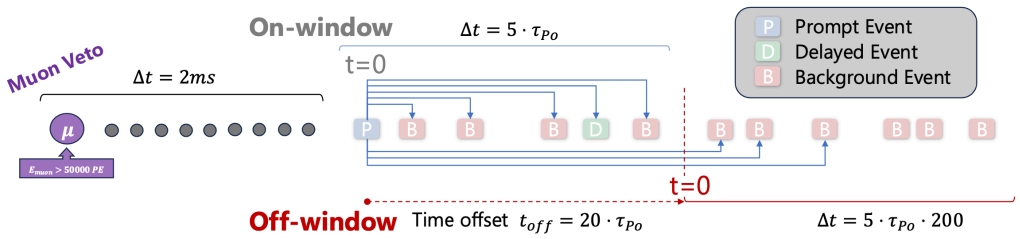


***Figure 4.4:*** *Schematic representation of the "Off-window" algorithm for identifying correlated prompt-delayed events via statistical background subtraction. A muon event (purple) is followed by cosmogenic events (gray). The prompt-tagged event is shown in blue, the delayed event in green, and uncorrelated background events in red. The offset and $\Delta t$ values shown are those used in this thesis. For a detailed explanation of each selection step, refer to the text.*

An example visualization of the energy spectra (prompt and delayed) and $\Delta t$ between events, showing the selection steps following the muon veto and reconstructed from an LS filling run, is presented in Fig. 4.5.

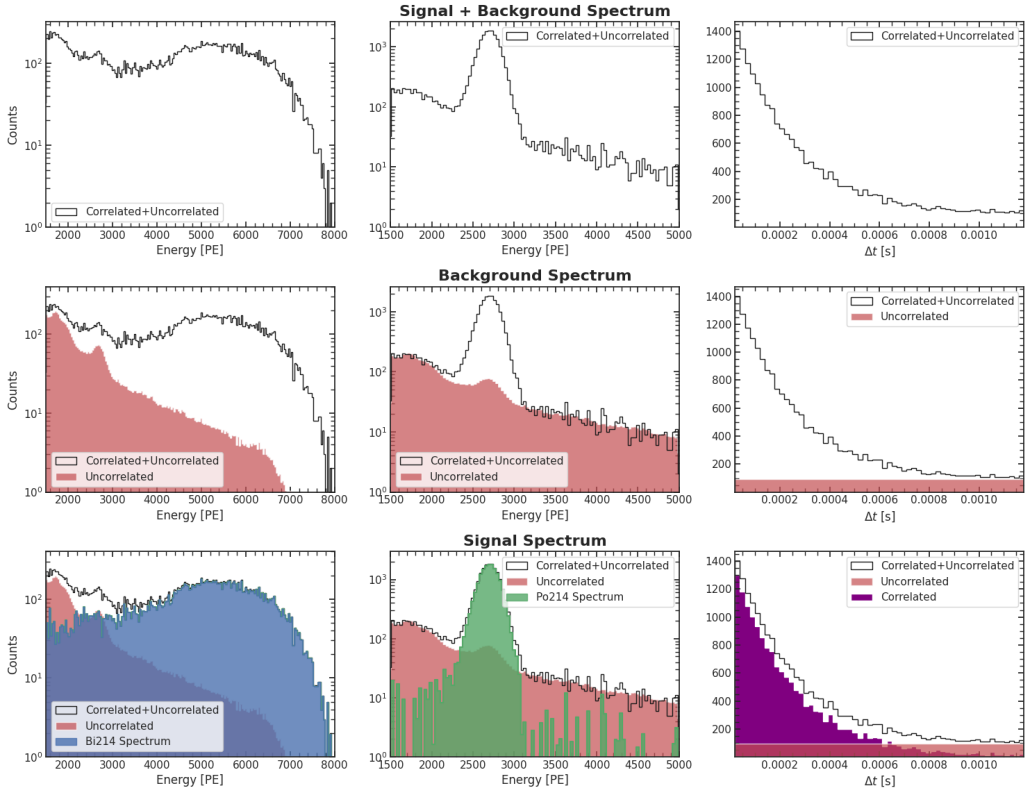


***Figure 4.5:*** *Example of BiPo event selection using the "Off-window" algorithm. The three columns show the prompt energy spectrum, delayed energy spectrum, and the $\Delta t$ between events. From top to bottom: (1) events in the "On-window" (i.e., correlated BiPo signals + uncorrelated background), (2) events in the "Off-window", normalized by the scale factor k (i.e., high-statistics estimate of the uncorrelated background), (3) events obtained from the statistical subtraction of "On-window" and "Off-window" samples. Color code: black for all events (correlated + uncorrelated), red for background-only events, blue for $^{214}$Bi $\beta$-decay spectrum, green for $^{214}$Po $\alpha$-decay spectrum, and purple for the $\Delta t$ distribution resulting from subtraction.*

The final step consists in describing the method used to estimate the selection efficiency of the algorithm. Given a specific cut, we define the cut efficiency $\varepsilon^{cut}$ as the ratio

$$\varepsilon_{cut} = \frac{N_{in}}{N_{out}} \tag{4.2}$$

where $N_{in}$ ($N_{out}$) is the number of events selected inside (outside) the cut window without the cut applied. The associated uncertainty is obtained via error propagation, assuming Poisson statistics for both $N_{in}$ and $N_{out}$. In practice, the overall selection efficiency of the algorithm is computed as the product of the efficiencies of each individual cut, under the reasonable assumption that the cuts are statistically independent. Therefore, we have:

$$\varepsilon = \varepsilon_{\Delta t} \cdot \varepsilon_{\Delta R} \cdot \varepsilon_{E_{prompt}} \cdot \varepsilon_{E_{delayed}} \tag{4.3}$$

with the total uncertainty again computed by propagating the individual contributions.
The estimation procedure for the efficiency of each cut is data-driven for the spatial and energy cuts, while it relies on the Cumulative Distribution Function (CDF) for the timing cut. In detail:

- **Timing cut:** The CDF is fixed by the exponential distribution with time constant $\tau = \tau_{^{214}\mathrm{Po}}$. The quantities $N_{in}$ and $N_{out}$ are obtained by integrating the function within (and outside) the time window defined by the cut thresholds:

$$\varepsilon_{\Delta t} = \frac{\int_0^{\Delta t_{On}} e^{-t/\tau} dt}{\int_0^{\infty} e^{-t/\tau} dt} = 1 - e^{-\Delta t_{On}/\tau}. \tag{4.4}$$

- **Spatial and Energy cuts:** (i) A run is performed with on-window/off-window selection, switching off one cut at a time (assuming independence); (ii) the values of $N_{in}$ and $N_{out}$ are extracted while keeping all other cuts active, except for the one under evaluation.

By choosing sufficiently wide cut regions, the off-window selection allows for an optimal estimation of the background, which can then be subtracted from the highly contaminated on-window sample. The average efficiency obtained with this method, across different runs and adapting the cut values to software and hardware changes implemented over time, is $\varepsilon = (81 \pm 1)\%$. An example of the various distributions, with the regions inside and outside the cut thresholds highlighted, is shown in Fig. 4.6.

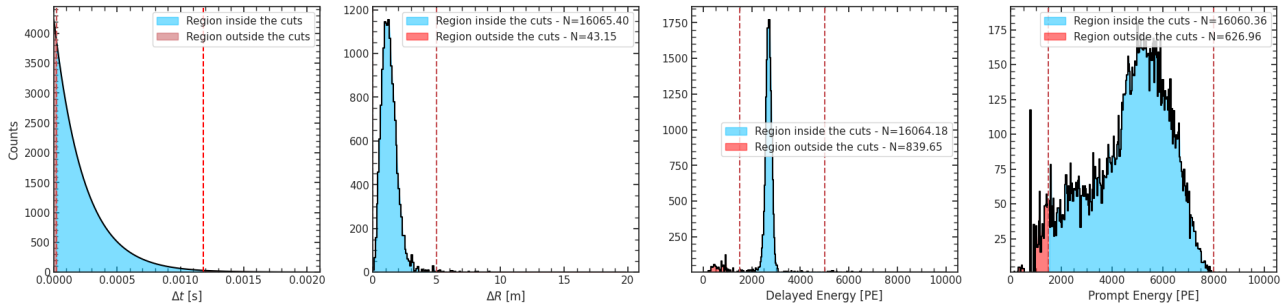


***Figure 4.6:*** *Examples of the $\Delta t$, $\Delta R$, $E_{delayed}$, and $E_{prompt}$ distributions, with regions inside (blue) and outside (red) the cut thresholds highlighted. For a more detailed description of the method, refer to the main text.*

At this stage, the algorithm is robust, achieving good selection efficiency and excellent purity thanks to background subtraction. Moreover, the algorithm is entirely data-driven—an essential feature during the commissioning phase of the detector, in which this thesis work is situated—and highly versatile, allowing for the effective selection of different classes of correlated events, not limited to those from radioactive decays considered in this analysis. For instance, this algorithm has also enabled the identification of spallation neutrons produced by muons traversing the CD (see Section 4.3). These events have also been used as a uniform and continuous calibration source for the construction of non-uniformity maps (for more details, refer to Chapter 5).

As for the radiocontamination analysis, the next step is to use the selection algorithm developed here to estimate the contamination from $^{238}$U and to monitor BiPo activity throughout the entire commissioning period.

### 4.2.2 Radiopurity Monitoring in JUNO

The strategy used to estimate the contamination of $^{238}$U from the fast coincidence BiPo tagging is based on measuring the BiPo activity to infer the activity of $^{222}$Rn and, under the assumption of secular equilibrium, the activity of $^{238}$U and hence its contamination level. A brief theoretical summary of radioactive decays is provided in Appendix C.

Once BiPo events have been identified, it is necessary to define the Activity variable accounting for selection efficiency, varying run durations, and the different volumes of LS involved, in order to allow comparisons between different runs, including those taken during the filling phase. The activity is estimated from data as:

$$\mathcal{A}\left[\frac{mBq}{m^3}\right] = \frac{N_{BiPo}}{\varepsilon \cdot T \cdot V_{LS}} \tag{4.5}$$

where $\varepsilon$ is the total selection efficiency estimated as in Eq. 4.3, $T$ is the exposure time over which the activity is calculated, $V_{LS}$ is the volume of LS at that time, and $N_{BiPo}$ is the number of BiPo candidates, estimated as the integral over the correlated coincidence region:

$$N_{BiPo} = \int_{t_{min}}^{t_{max}} A_{exp} \cdot e^{-\frac{t}{\tau_{exp}}} = A \cdot \tau_{exp} \cdot \left(e^{-\frac{t_{min}}{\tau_{exp}}} - e^{-\frac{t_{max}}{\tau_{exp}}}\right) \tag{4.6}$$

where $A_{exp}$ and $\tau_{exp}$ are the amplitude and decay constant, respectively, estimated from the time difference distribution of correlated pairs. In order to reduce uncertainties on these parameters, a specific fitting procedure is adopted: (i) the Poisson likelihood of the model $y = A \cdot e^{-\frac{\Delta t}{\tau}} + C$ is constructed; (ii) the constant term $C$ is fixed using a pull term on the background component, independently estimated from a high-statistics dataset using the off-window technique; (iii) the values of $A$ and $\tau$ are extracted by maximizing the Poisson likelihood. An example fit is shown in Fig. 4.7.

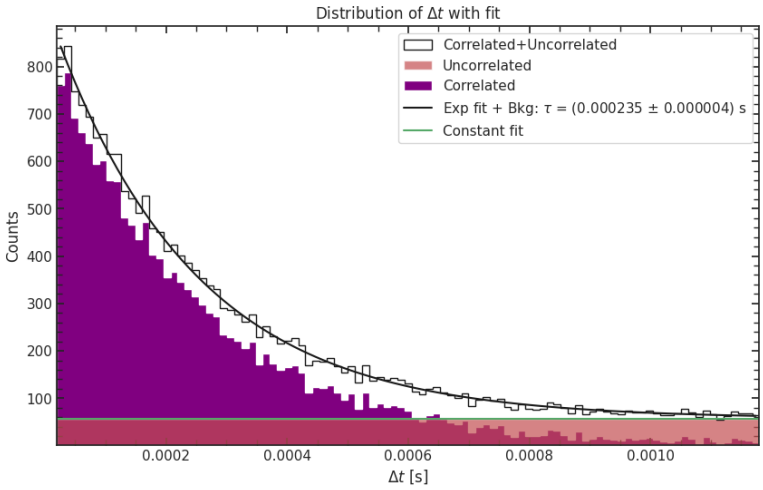


***Figure 4.7:*** *Example fit of the $\Delta t$ distribution between correlated events. Shown are: the distribution of correlated + uncorrelated coincidences in the on-window region (black empty histogram), the uncorrelated background (red) with the fitted constant background term (green), and the statistically subtracted correlated component (purple). The fitted value of $\tau$ is consistent within $1\sigma$ with the expected value ($\tau_{^{214}Po} = 237\ \mu s$).*

The algorithm described above has been applied to estimate BiPo activity in real time for each run

with the "LS-filling" or "Physics" tag and a duration longer than one hour. Each run is divided into 1-hour subsamples to increase statistics in the activity plot. The overall trend during the considered period is shown in Fig. 4.8.

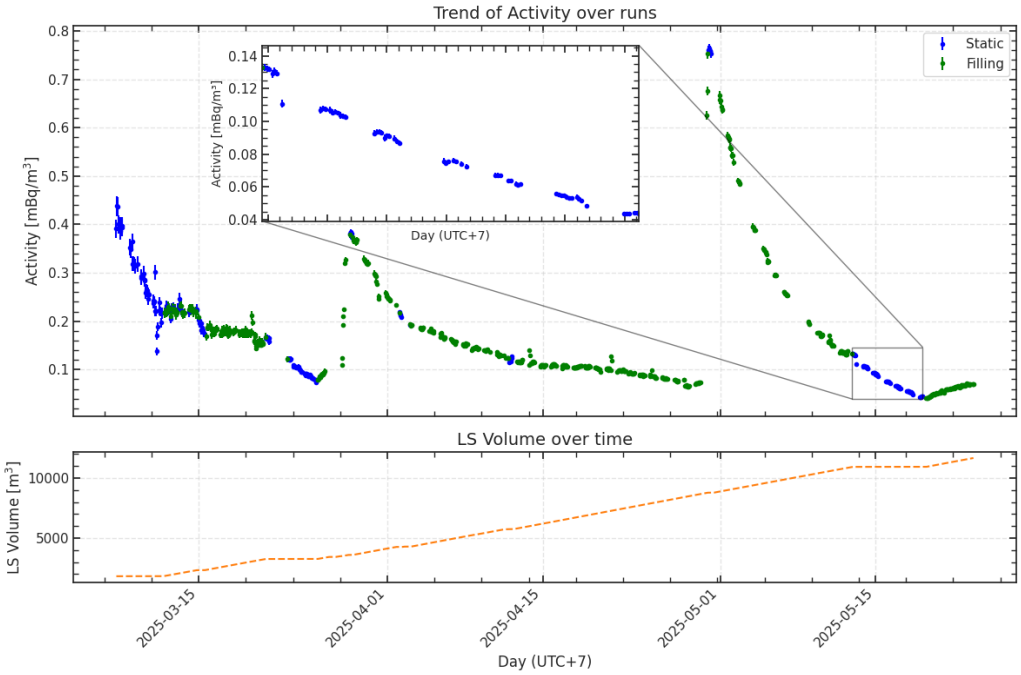


***Figure 4.8: Top:*** *Time evolution of BiPo activity (in mBq/m$^3$) during the considered period. Runs with filling paused are shown in blue, while those with active filling of new LS are shown in green. The inset highlights the activity trend during a filling stop longer than 5 days, used to estimate the $^{238}U$ concentration.* ***Bottom:*** *Volume of LS in the CD over time in m$^3$. The slope during commissioning periods corresponds to the filling rate $v = 7\, m^3/h$.*

This plot highlights two main anomalous jumps in activity, attributed to sudden and significant injections of $^{222}$Rn due to necessary hardware operations on the experiment. These increases occurred rapidly, and a subsequent decrease in activity was observed, even during LS filling periods, indicating that the externally introduced $^{222}$Rn was decaying, leaving only the residual contamination introduced by the newly added LS (whose $^{222}$Rn had yet to decay).

Focusing on the longest filling stop period (from May 13 to May 19, 2025), the activity measured during this time confirms the absence of new $^{222}$Rn leak into the detector. Thus, the observed exponential trend is attributed solely to the decay of pre-existing $^{222}$Rn in the LS. Knowing the decay constant of $^{222}$Rn is $\tau_{^{222}Rn} = 5.5$ days, this period is long enough to attempt an estimation of the residual activity of $^{222}$Rn, which—under the secular equilibrium hypothesis—corresponds to the activity of $^{238}$U.

The activity data from May 13–19, 2025 were fitted (via Poisson likelihood maximization) using the model:

$$y = A \cdot e^{-\frac{\Delta t}{\tau}} + C \tag{4.7}$$

under two conditions:

- With $\tau$ fixed to $\tau_{^{222}Rn} = 5.5$ days: the results of the fit are shown in Fig. 4.9a, and the residual

$^{238}$U activity—under secular equilibrium assumption—is given by:

$$\mathcal{A}^{\text{fixed}}_{^{238}U} = C_{\text{fixed}} = (0.0030 \pm 0.0013)\,\frac{mBq}{m^3} \tag{4.8}$$

- With $\tau$ left as a free parameter: the fit results are shown in Fig. 4.9b, and the estimated $^{238}$U activity is:

$$\mathcal{A}^{\text{not fixed}}_{^{238}U} = C_{\text{not fixed}} = (0.0017 \pm 0.0089)\,\frac{mBq}{m^3} \tag{4.9}$$

The compatibility of this value with zero will be discussed shortly.

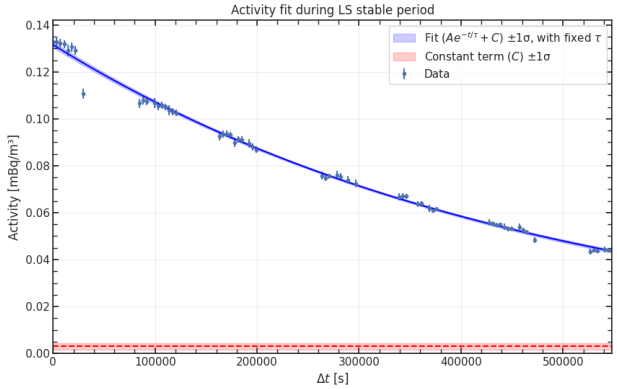


***(a)*** *Fit of BiPo activity between May 13 and May 19 (during an LS filling pause). The exponential fit with fixed $\tau = \tau_{^{222}Rn} = 5.5$ days and a constant background is shown in blue. The constant term $C_{fixed}$ is shown in red.*

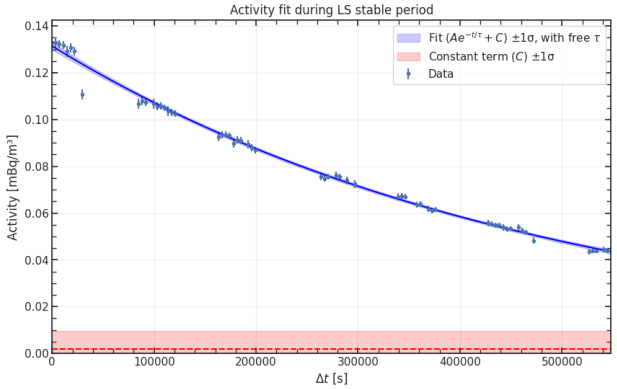


***(b)*** *Fit of BiPo activity between May 13 and May 19 (during an LS filling pause). The exponential fit with free $\tau$ and a constant background is shown in blue. The constant term $C_{not\ fixed}$ is shown in red.*

***Figure 4.9:*** *Fit of BiPo activity between May 13 and May 19 (during an LS filling pause).*

Starting from the activity estimate—regardless of the method used—the concentration of $^{238}$U can be derived through a straightforward calculation:

$$C_{^{238}U}\left[\frac{g}{g}\right] = N_{^{238}U}\cdot\frac{\mathcal{M}_{^{238}U}}{N_A} = \frac{\mathcal{A}_{^{238}U}}{\lambda_{^{238}U}}\cdot\frac{\mathcal{M}_{^{238}U}}{N_A} = \mathcal{A}_{^{238}U}\left[\frac{mBq}{m^3}\right]\cdot\left(\frac{10^{-3}}{\rho_{LS}}\right)\cdot\frac{\mathcal{M}_{^{238}U}}{\lambda_{^{238}U}\cdot N_A} \tag{4.10}$$

Here, $\mathcal{M}_{^{238}U}$ is the molar mass of $^{238}$U, $N_A$ is Avogadro's number, and $N_{^{238}U}$ represents the number density of $^{238}$U atoms per gram. Using the following numerical values:

$$\mathcal{M}_{^{238}U}\left[\frac{g}{mol}\right] = 238\ \frac{g}{mol} \tag{4.11}$$

$$\lambda_{^{238}U}\left[\frac{1}{s}\right] = \frac{\ln(2)}{T^{1/2}_{^{238}U}} = 4.916\cdot10^{-18}\frac{1}{s} \tag{4.12}$$

$$N_A\left[\frac{atoms}{mol}\right] = 6.022\cdot10^{23}\frac{atoms}{mol} \tag{4.13}$$

$$\rho_{LS}\left[\frac{g}{m^3}\right] = 8.7\cdot10^{5}\frac{g}{m^3} \tag{4.14}$$

we obtain:

$$C_{^{238}U}\left[\frac{g}{g}\right] = \left(9.24 \cdot 10^{-14}\left[\frac{m^3}{mBq}\cdot\frac{g}{g}\right]\right)\cdot \mathcal{A}_{^{238}U}\left[\frac{mBq}{m^3}\right] \tag{4.15}$$

By inserting the values of $\mathcal{A}_{^{238}U}$ obtained from the fit, we find:

$$C_{^{238}U}^{\tau_{^{222}Rn}^{\text{fixed}}} = (2.8 \pm 1.2)\cdot 10^{-16}\ \frac{g}{g} \tag{4.16}$$

$$C_{^{238}U}^{\tau_{^{222}Rn}^{\text{not fixed}}} = (1.6 \pm 8.2)\cdot 10^{-16}\ \frac{g}{g} \tag{4.17}$$

While the value of $C_{^{238}\mathrm{U}}^{\tau_{^{222}\mathrm{Rn}}^{\text{fixed}}}$ can be physically interpreted as an estimate of the $^{238}$U concentration, the same does not hold for $C_{^{238}\mathrm{U}}^{\tau_{^{222}\mathrm{Rn}}^{\text{not fixed}}}$. As shown in Fig. 4.10, which displays the $\chi^2$ distribution for the variable $C_{\text{not fixed}}$ (related to $C_{^{238}\mathrm{U}}^{\tau_{^{222}\mathrm{Rn}}^{\text{not fixed}}}$ through Eq. 4.15 under the hypothesis of Eq. 4.9), this quantity is compatible with zero within $1\sigma$, and is therefore not physically meaningful.

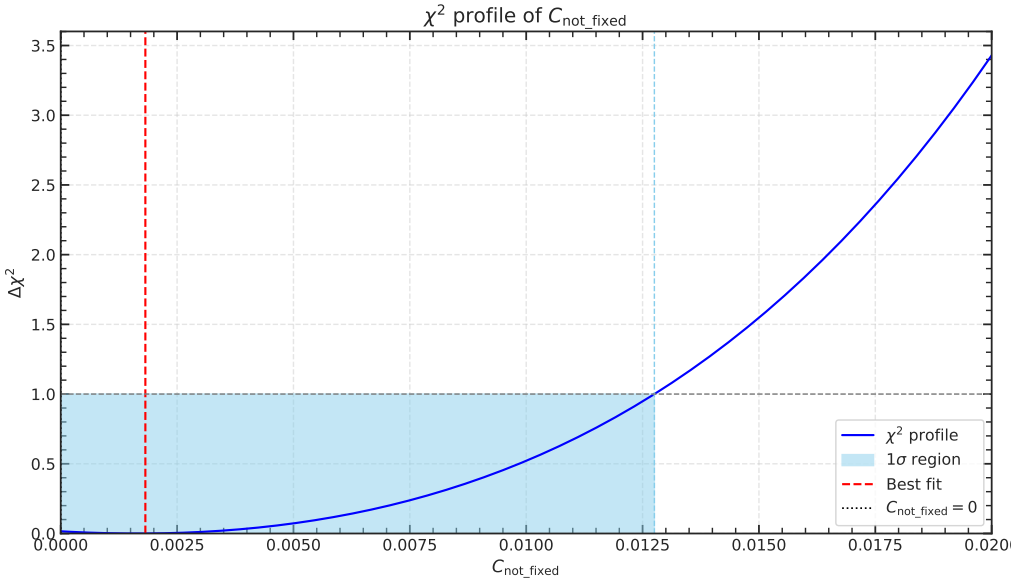


***Figure 4.10:*** *$\chi^2$ distribution for the variable $C_{not\ fixed}$, with the $1\sigma$ region highlighted.*

Nevertheless, the fit performed with $\tau$ left free still allows one to set an upper bound—interpreted in a probabilistic sense—on the $^{238}$U contamination level in the LS. Based on Bayes' theorem, the posterior probability distribution can be computed as

$$p(\boldsymbol{\theta}|\boldsymbol{x}) = \frac{p(\boldsymbol{x}|\boldsymbol{\theta})\,p(\boldsymbol{\theta})}{p(\boldsymbol{x})} \tag{4.18}$$

where $p(\boldsymbol{x}|\boldsymbol{\theta})$ is the likelihood function (in this case, a Poisson likelihood corresponding to the model in Eq. 4.7), and $p(\boldsymbol{\theta})$ is the prior probability distribution, which encodes prior knowledge about the fit parameters (here assumed to be uniform and positive over all parameters). The function $p(\boldsymbol{x})$, known as the evidence (or marginal likelihood), for parameter estimation under a fixed model, serves merely

as a normalization constant. The posterior distribution of $C_{^{238}\mathrm{U}}^{\tau_{^{222}\mathrm{Rn}}^{\text{not fixed}}}$ is shown in Fig. 4.11.

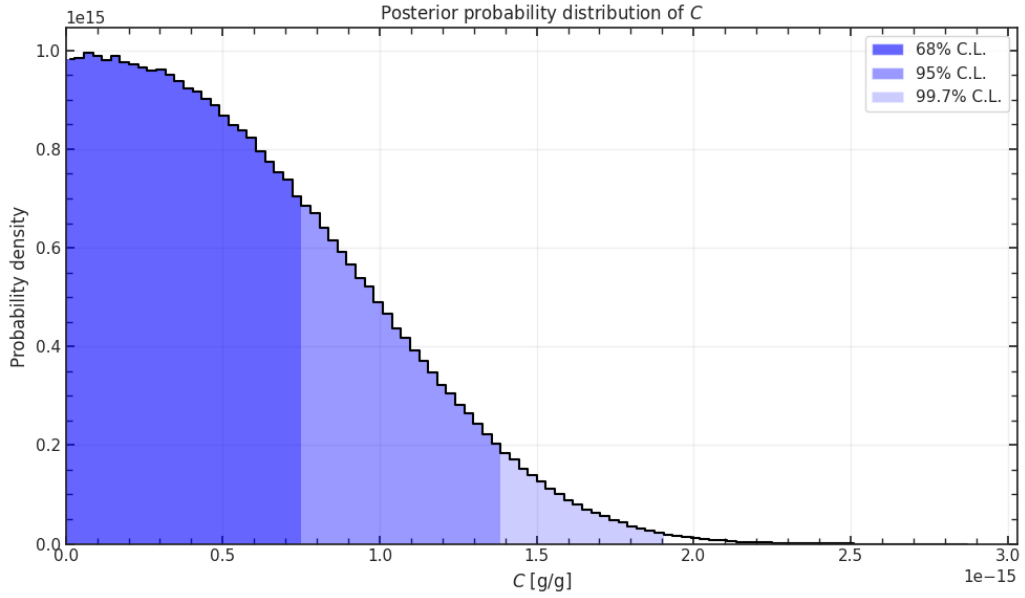


***Figure 4.11:*** *Posterior distribution of $C_{^{238}U}^{\tau_{^{222}Rn}^{not\ fixed}}$, with 68%, 95%, and 99.7% credibility intervals highlighted.*

From this distribution, it is possible to extract an upper limit value for $C_{^{238}U}^{\tau_{^{222}Rn}^{\text{not fixed}}}$ at different Credibility Interval (CI). We therefore conclude this chapter with the final concentration estimates of $C_{^{238}U}$:

$$C_{^{238}U}^{\tau_{^{222}Rn}^{\text{fixed}}} = (2.8 \pm 1.2) \cdot 10^{-16}\ \frac{g}{g} \tag{4.19}$$

$$C_{^{238}U}^{\tau_{^{222}Rn}^{\text{not fixed}}} < 7.5 \cdot 10^{-16}\ \frac{g}{g} \quad @\ 68\%\ \text{CI} \tag{4.20}$$

$$C_{^{238}U}^{\tau_{^{222}Rn}^{\text{not fixed}}} < 1.3 \cdot 10^{-15}\ \frac{g}{g} \quad @\ 95\%\ \text{CI} \tag{4.21}$$

Both 4.19 and 4.20 results lie below the required limit of $10^{-15}\frac{g}{g}$ for IBD-level analyses, and are of the same order of magnitude as the requirements for solar-level analyses. To obtain a more precise estimate, it will be necessary to wait for the completion of the filling process or for a phase in which the amount of LS remains stable for several weeks, once the $^{222}$Rn introduced with the new LS—which disrupts the secular equilibrium with $^{238}$U—has fully decayed.

## 4.3 Application of event selection algorithm: Spallation neutrons

As previously introduced, there are several other sources of correlated background that can mimic the prompt or delayed signals of IBD-like events. Among these, cosmogenic events play a particularly relevant role. Tagging $^{9}$Li and $^{8}$He events requires precise muon track reconstruction, which, during this commissioning phase with LS filling, proves especially challenging. Therefore, a dedicated treatment of this background source is deferred to future work.
Conversely, spallation neutron-induced background can be effectively tagged. As previously mentioned, these neutrons are captured by free protons in the LS, thereby emulating a delayed IBD-like signal.

To identify spallation neutrons, the same algorithm presented in Section 4.2.1 was employed, this time searching for delayed candidates within the time window following a muon passage (i.e., within the sample previously vetoed for the selection of BiPo candidates). Spallation neutrons, acting as delayed events, produce a characteristic energy peak at 2.2 MeV. An energy cut is thus applied around this region. Figure 4.12 shows an example energy spectrum around the expected neutron capture peak.

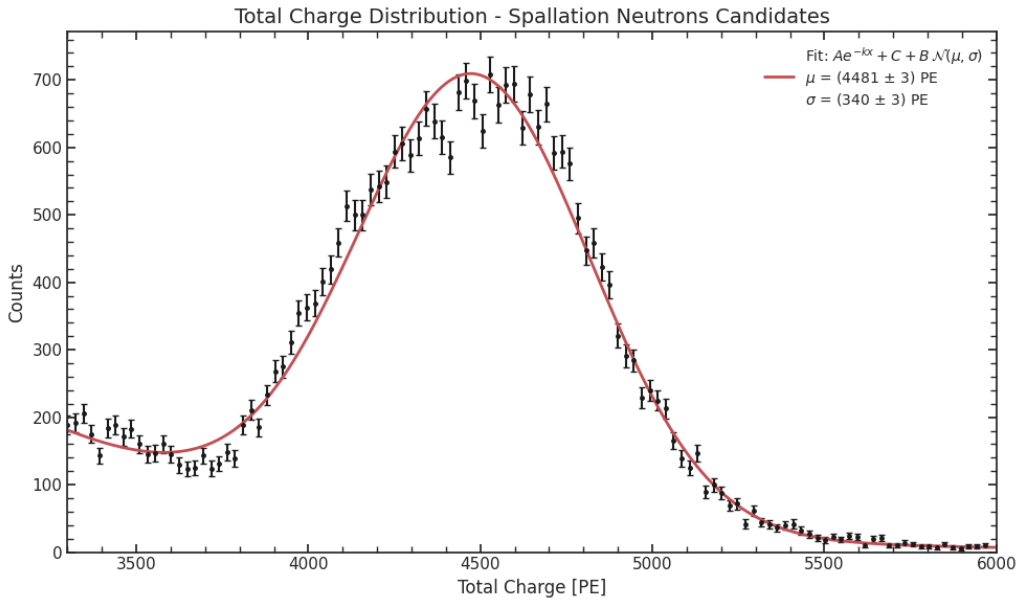


***Figure 4.12:*** *Total charge distribution for events tagged as spallation neutrons. In black: the total charge histogram; in red: the exponential plus Gaussian fit.*

By performing a Gaussian fit with an exponential background (superimposed on the histogram in Figure 4.12), a preliminary estimate of the Light Yield (LY)—i.e., the number of photoelectrons produced per MeV of energy deposited in the LS—can be extracted as

$$LY = \frac{\mu\,[\mathrm{PE}]}{2.2\,[\mathrm{MeV}]} = (2037 \pm 1)\,\frac{\mathrm{PE}}{\mathrm{MeV}}\,. \tag{4.22}$$

Based on this result, a simple energy calibration of the spectrum can be performed. The calibrated

spectrum is shown in Figure 4.13.

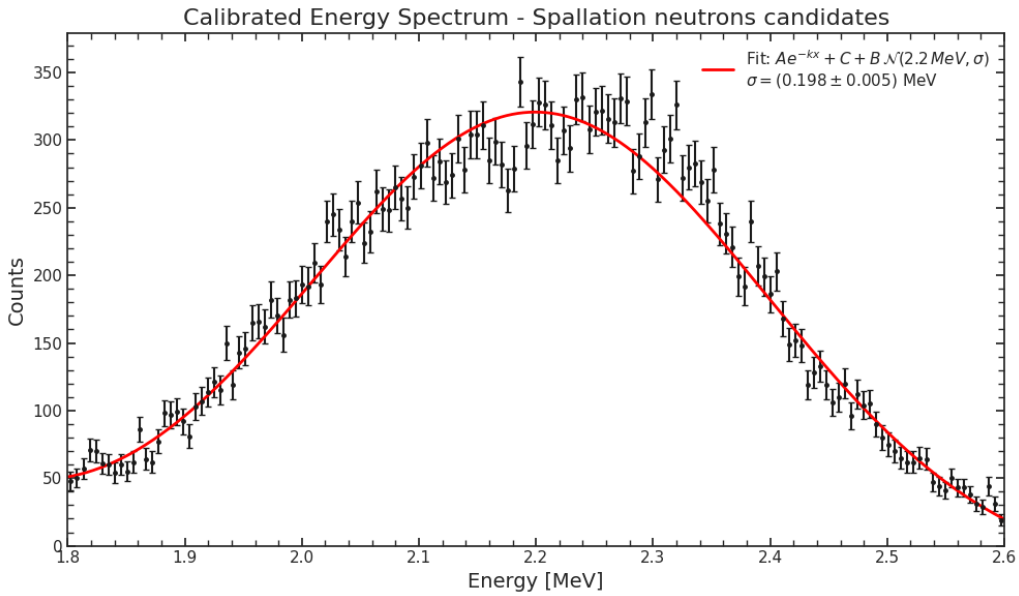


***Figure 4.13:*** *Calibrated energy distribution for events tagged as spallation neutrons. In black: the total charge histogram; in red: the exponential plus Gaussian fit.*

From the same fit, it is also possible to estimate the energy resolution as

$$\frac{\sigma_E}{E} = \frac{\sigma}{\mu} \approx (9.0 \pm 0.2)\% \,. \tag{4.23}$$

It is immediately evident that this value exceeds the resolution requirement set by the JUNO collaboration, which is $3\%$ at 1 MeV (equivalent to $2\%$ at 2.2 MeV). It is therefore necessary to investigate the factors responsible for the degradation of the energy resolution and to apply the appropriate corrections to achieve compliance with the required performance. The next chapter will focus on energy resolution, with particular attention to the issue of non-uniformity.

# 5

# Energy Resolution

JUNO aims to resolve the NMO by probing the interference effect of the two fast oscillations induced by $|\Delta m^2_{31}|$ and $|\Delta m^2_{32}|$ of reactor antineutrinos. Sufficient energy resolution is crucial to accurately measure the oscillation pattern in the antineutrino spectrum, and it directly determines the sensitivity to the NMO. In this context, the energy resolution refers to the sigma-to-mean ratio of the Gaussian function used to fit the energy distribution of positrons emitted from IBD reactions at a fixed energy. The designed energy resolution of JUNO is 3% at 1 MeV. Previous LS-based neutrino detectors, such as the Borexino and KamLAND experiments, have achieved energy resolutions of 5% and 6.5% at 1 MeV, respectively. In those experiments, statistical fluctuations dominated the energy resolution. The JUNO detector has been designed with a focus on achieving high LS light yield, high transparency, and high photon collection efficiency in order to maximize the number of detected PE and thus minimize the statistical fluctuations. However, due to the unprecedented size, employed PMTs and energy resolution requirement of JUNO, several other factors significantly contribute to the energy resolution and must be carefully evaluated. One of these is the non-uniform detector response, a phenomenon in which the number of photoelectrons detected per MeV of deposited energy (i.e., the LY) varies depending on the position within the detector. Previous simulations indicate that non-uniformity in JUNO is on the order of 20% [20].

The goal of this chapter is to investigate the energy resolution in JUNO, and it is structured as follows: Section 5.1 describes the detector response following an IBD event, examines the main processes responsible for the degradation of the energy resolution, and presents a strategy to mitigate the effects of non-uniformity. Section 5.2 introduces a time-based vertex reconstruction algorithm, aimed at identifying the spatial position of spallation neutrons already effectively tagged using the algorithm presented in Chapter 4, and exploited here as a uniform, constant, and continuous calibration source in JUNO. Finally, Section 5.3 presents the construction of the non-uniformity map in JUNO during this commissioning phase, along with a discussion of the obtained results.

## 5.1 Detector Energy Response

The purpose of this introductory section is to briefly describe the JUNO response following an IBD event, highlighting the main stages involved. In particular, it focuses on the importance of linking the energy observed by the PMTs to the energy of the incoming electron antineutrino, taking into account all relevant sources of uncertainty. Furthermore, the importance of energy resolution in JUNO will be discussed, starting from its definition and examining strategies for its improvement.

An overview of the energy deposition and signal propagation processes in JUNO is illustrated in Fig. 5.1.

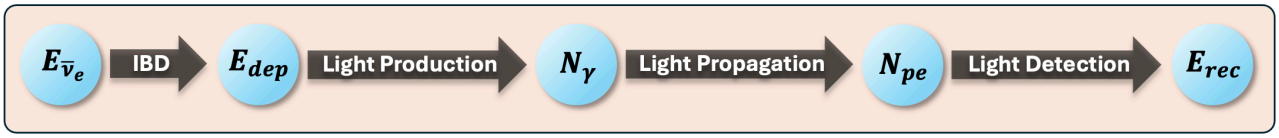


***Figure 5.1:*** *Diagram of signal propagation in JUNO, highlighting the different processes and variables involved. For a detailed explanation of each stage, see the main text.*

In more detail, starting from the interaction of an electron antineutrino with energy $E_{\bar{\nu}_e}$ in the LS, four main stages lead to the reconstructed energy $E_{rec}$, each contributing to the degradation of the energy resolution [58]:

1. **IBD:** Already extensively described in Chapter 4, the IBD mechanism is the primary interaction between reactor electron antineutrinos and free protons in the LS, resulting in a neutron and a positron (which carries away nearly all the kinetic energy of the antineutrino). As a first approximation, due to kinematic considerations, the positron energy can be related to the incident antineutrino energy via:

$$E_{dep} = E_{e^+} \approx E_{\bar{\nu}_e} - 0.8\,\text{MeV} \tag{5.1}$$

   A more detailed kinematic treatment is provided in Appendix A.

2. **Light Production:** The positron deposits energy in the scintillator ($E_{dep}$), leading to the production of photons ($N_\gamma$) through two main mechanisms:

   - **Scintillation:** Since the concentrations of PPO and bis-MSB in the LS are relatively low, the deposited energy is primarily transferred to LAB molecules. These excited molecules can then transfer energy to fluor molecules through complex molecular interactions [59]. Photon emission occurs during the de-excitation of the fluor molecules. However, the number of emitted scintillation photons is not linearly proportional to the deposited energy due to the quenching effect [60], where some excited states de-excite non-radiatively. This phenomenon is commonly described by the semi-empirical Birks formula [61]:

$$\frac{dN_{scintOP}}{dx} = LY \cdot \frac{\frac{dE}{dx}}{1 + kB\frac{dE}{dx}} \tag{5.2}$$

where $N_{ScintOP}$ is the number of scintillation photons, $LY$ is the light yield in PE/MeV (in the absence of quenching), $dE/dx$ is the stopping power, and $kB$ is the Birks coefficient, dependent on particle type.

- **Cherenkov:** When the positron and its charged secondaries travel through the LS faster than the group velocity of light in the medium, Cherenkov radiation is emitted. The Frank-Tamm formula [62] estimates the number of Cherenkov photons produced per unit path length per wavelength:

$$\frac{d^2N_{CherenOP}}{dx\,d\lambda} = \frac{2\pi\alpha z^2}{\lambda^2}\left(1 - \frac{1}{\beta^2 n(\lambda)^2}\right) \tag{5.3}$$

where $\alpha$ is the fine structure constant, $\beta$ is the particle velocity normalized to the speed of light in vacuum, and $n(\lambda)$ is the refractive index of the LS, dependent on wavelength.

3. **Light Propagation:** Both scintillation and Cherenkov photons may undergo multiple processes during their propagation, including absorption, scattering, reflection, and transmission across material boundaries. Photon transport in the LS is modeled using optical parameters such as absorption length, re-emission probability, Rayleigh scattering length, and the refractive indices of detector components. Only a fraction of the generated photons are detected by the PMTs and converted into PE. Thus, te average total number of PE, $N_{pe}$, is not directly proportional to $E_{dep}$, leading to the definition of the liquid scintillator non-linearity (LSNL):

$$f_{LSNL}(E_{dep}) = \frac{E_{vis}}{E_{dep}} \tag{5.4}$$

where $E_{vis}$ is the visible energy, defined as the expected reconstructed energy in the ideal case of perfect resolution.

4. **Light Detection:** The PMT and electronics responses introduce further fluctuations in the measured $N_{pe}$. These include the single photoelectron resolution (due to statistical fluctuations in the dynode or MCP amplification process), dark noise, afterpulses, electronics noise, and digitization effects.

### 5.1.1 Energy Resolution and Non-Uniformity

The energy resolution for a given visible energy $E_{vis}$ (in MeV) can be approximately expressed as:

$$\frac{\sigma_{E_{vis}}}{E_{vis}} = \sqrt{\left(\frac{a}{\sqrt{E_{vis}}}\right)^2 + b^2 + \left(\frac{c}{E_{vis}}\right)^2} \tag{5.5}$$

Where:

- The **a term** is the statistical term, mainly due to the Poisson fluctuations in the number of detected PEs. For a light yield of 1665 PE/MeV, the value of $a$ is about 2.7% [20].
- The **b term** is a constant term, dominated by spatial non-uniformity in detector response.

- The **c term** accounts for background noise, primarily due to PMT dark noise (DN), which contributes independently of the deposited energy. This term is estimated to be around 1.0% [20].

The impact of Eq. 5.5 on the sensitivity to the NMO has been studied in [58].

From a calibration perspective, minimizing the $b$ term is crucial for optimizing the energy resolution, especially in light of the large apparent non-uniformity. The strategy adopted to mitigate this effect is twofold: the use of radioactive sources deployed at known positions within the detector, and the use of a uniform, continuous (~1.8 evt/s [39]) and homogeneous source such as spallation neutrons produced by cosmic muons traversing the CD. In this thesis, the second approach is adopted, utilizing the already tested selection algorithm presented in Chapter 4, with the only missing element being the interaction vertex reconstruction. To this end, in the following sections, a vertex reconstruction algorithm is proposed (Section 5.2) to identify the position of tagged spallation neutron candidates. This will enable the construction of a non-uniformity map and the correction of the spallation neutron energy spectrum, thereby improving the energy resolution (Section 5.3).

## 5.2 Vertex reconstruction algorithm

For reactor neutrinos, the energy peaks around 4 MeV, and most events fall below 10 MeV [63]. The typical spatial path of positrons generated by IBD interactions in the LS before annihilating is a few centimeters, which is negligible compared to the detector's size (40-meter diameter). Therefore, the positron track can be considered as a point-like light source located at the IBD interaction vertex.

This section aims to present a vertex reconstruction algorithm based on the information provided by the PMTs: the charge and the hit time. The simplest vertex reconstruction algorithm is the Charge Barycenter Method (also referred to as Charge Center Method (CCM)), which provides an approximate estimate of the event position using only information on the charge detected by each PMT. The performance and limitations of this method are discussed in Section 5.2.1.

For the specific goals of this chapter — namely, the precise tagging of spallation neutron positions to construct a non-uniformity map — the simple CCM is insufficient. Therefore, a time-based vertex reconstruction algorithm has been implemented, combining the charge response (to provide a rough vertex guess) with the time response of individual PMTs, characterized via the residual time $t^i_{res}$ variable similar to one defined in Eq. 3.2. The studies developed in Chapter 3 are thus of crucial importance for what follows and will be referenced throughout this section. Principles and performances of time-based algorithm are discussed in Section 5.2.2.

### 5.2.1 Charge vertex reconstruction

The CCM is based on the assumption that a point-like source emits photons isotropically in the LS and the closer a PMT is to the source, the more photons it detects. In particular [64]:

1. Light pulses generated by an event are detected by multiple PMTs positioned at various locations.
2. For each PMT, a weighted position is calculated based on the detected energy (assuming linearity with the charge) and the PMT's position. This represents the "charge center" for that PMT.
3. The average charge center is calculated from the weighted contributions of all PMTs involved in the event.
4. This average is then used to estimate the event vertex via:

$$\vec{r}_0 = \frac{\sum_i q_i \vec{r}_i}{\sum_i q_i} \tag{5.6}$$

   where $\vec{r}_0$ is the reconstructed vertex, $q_i$ is the charge detected by the $i$-th PMT, and $\vec{r}_i$ its position.

An example of CCM applied to a calibration run with an AmBe source placed at $V = (x, y, z) = (0, 0, 10.5)$ is shown in Fig. 5.2.

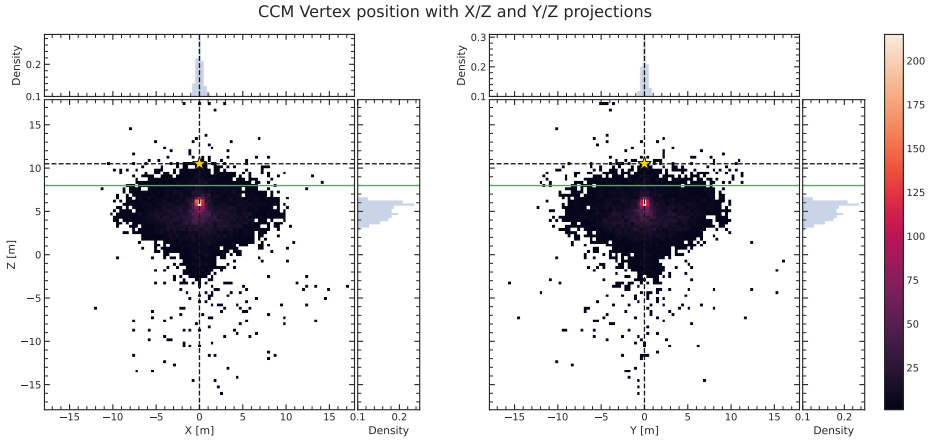


***Figure 5.2:*** *Vertex reconstruction using the CCM without bias correction, for a run with an AmBe source placed at $V = (x, y, z) = (0, 0, 10.5)$ (indicated by the black dashed line and a star-shaped marker). The water-LS interface level is shown in green.*

The reconstructed event distribution is systematically shifted by several meters from the true vertex. This bias is well known: even in an idealized model neglecting absorption and scattering, a simple geometric integral of photon hits on a spherical surface yields a reconstructed position at $2/3$ of the true position. Indeed, assuming the true vertex is at $z_0$, the expected reconstructed coordinate from the CCM is [65]:

$$
\begin{aligned}
\langle z \rangle &= \frac{1}{4\pi} \int z d\Omega = \\
&= \frac{1}{4\pi} \int_0^{2\pi} d\phi \int_0^{\pi} (z_0 + r \cdot cos\theta) sin\theta d\theta = \\
&= \frac{1}{2} \int_0^{\pi} -(z_0 + (\sqrt{R^2 - z_0^2 sin^2\theta} - z_0 cos\theta) \cdot cos\theta) dcos\theta \\
&= \frac{1}{2} \int_{-1}^{1} (z_0 + x\sqrt{R^2 - z_0^2 x^2} - z_0 x^2) dx = \\
&= \frac{2}{3} z_0
\end{aligned}
$$

Thus, multiplying the reconstructed $z$ by a factor of $3/2$ yields a better approximation of the true $z_0$. This factor is derived purely from geometry and is independent of the detector configuration or optical processes. To better adapt this correction to the real detector setup, Eq. 5.6 was modified by introducing a bias factor $a$:

$$
\vec{r}_0 = a \cdot \frac{\sum_i q_i \vec{r}_i}{\sum_i q_i} \tag{5.7}
$$

The optimal value of $a$ was determined by maximizing the agreement between the reconstructed and true vertex positions in AmBe calibration runs. The best correction factor found was $a = 1.75$, and the resulting reconstruction (applying Eq. 5.7) is shown in Fig. 5.3.

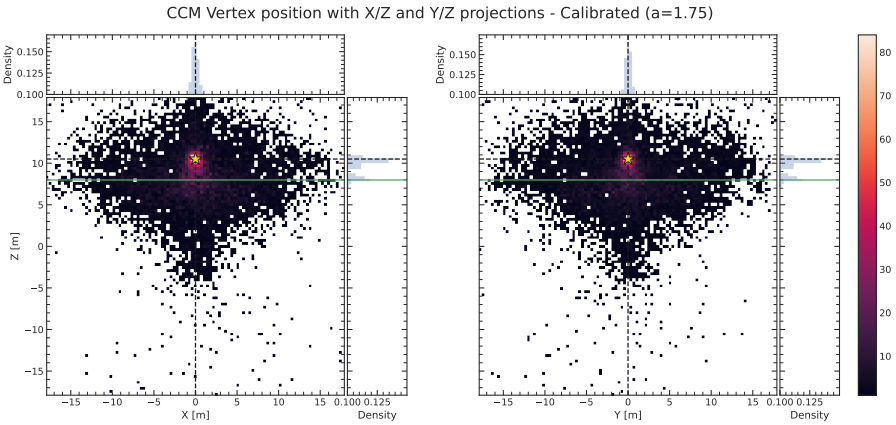


***Figure 5.3:*** *Vertex reconstruction using the CCM with bias correction ($a = 1.75$) for a run with an AmBe source at $V = (x, y, z) = (0, 0, 10.5)$ (indicated by the black dashed line and a star-shaped marker). The water-LS interface is shown in green.*

The vertex estimate from the CCM thus serves as a good initial guess for a more sophisticated algorithm that includes the temporal response of the detector, described in the next section.

### 5.2.2 Time vertex reconstruction

The core idea of the algorithm is to construct a time-based likelihood function that parametrizes the detector's full temporal response (discussed in Section 5.1), and then maximize it with respect to the event parameters to estimate the interaction time $t_0$ and vertex $\vec{r}_0$. This involves defining a variable, namely the residual time $t^i_{res}$, based on Eq. 3.2

$$t^i_{res}(\vec{r}_0, t_0) = \text{HitTime}_i - ToF_i - t_0 \tag{5.8}$$

where $t_0$ is now the unknown interaction time, which indirectly allows reconstruction of the vertex position $\vec{r}_0$. Figure 5.4 shows the experimental distribution of hit times detected by all PMTs (both submerged in LS and Water) for a single event. The goal is to reproduce this distribution by modeling the temporal response for any given vertex location.

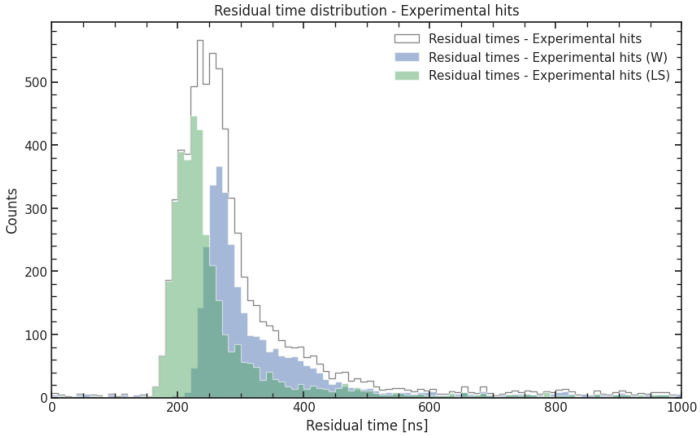


***Figure 5.4:*** *Experimental hit time distribution for a single event. In gray: all PMTs; in light blue and green: only PMTs in water and in LS, respectively.*

As anticipated, the detector's time response following a particle interaction in the LS can be divided into three main phases with a well defined Probability Density Function (PDF) $f(t^i_{res})$ of residual time for the i-th PMT (see Fig. 5.1):

- **Light Production:** The particle interaction in the LS leads to scintillation light emission, with intensity depending on the particle type and energy. The temporal response is modeled as the sum of three exponential components (slow, intermediate and fast) with characteristic decay times $\tau_i$. Since no direct measurement was conducted in this work, see [66] and [67] for further details. The PDF that parametrize this phase is

$$f_{Scint}(t_{res}) = \sum_k w_k \cdot e^{-\frac{t_{res}}{\tau_k}} \qquad \text{With:} \quad \sum_k w_k = 1 \tag{5.9}$$

- **Light Propagation:** This is modeled by a per-PMT offset called ToF, which acts as an additive delay and does not affect the distribution shape. A detailed study and the analytical form of the ToF map are presented in Chapter 3, Eq. 3.21.

- **Light Detection:** This phase accounts for the intrinsic time response of each PMT. A suitable parametrization (simplification of Eq. 3.22 in the assumption of constant background) was developed and validated using laser calibration runs. The fit parameters for each PMT (like the TTS $\sigma_{TTS}$, the average transit time $\mu$ and the DN) were tabulated as described in Chapter 3. The PDF that parametrize this phase (taking into account also DN) is

$$f_{PMT}(t_{res}) = N \cdot \left( \frac{\alpha}{2\tau} \cdot e^{\frac{2\mu + \frac{\sigma^2}{\tau} - 2t}{2\tau}} \cdot \text{erfc}\left( \frac{\mu + \frac{\sigma^2}{\tau} - t}{\sqrt{2}\sigma} \right) + DN \right) \qquad \text{With: N normalization factor} \tag{5.10}$$

Figure 5.5 shows a visualization of these light propagation phases for a single PMT observing an event at time $t_0$.

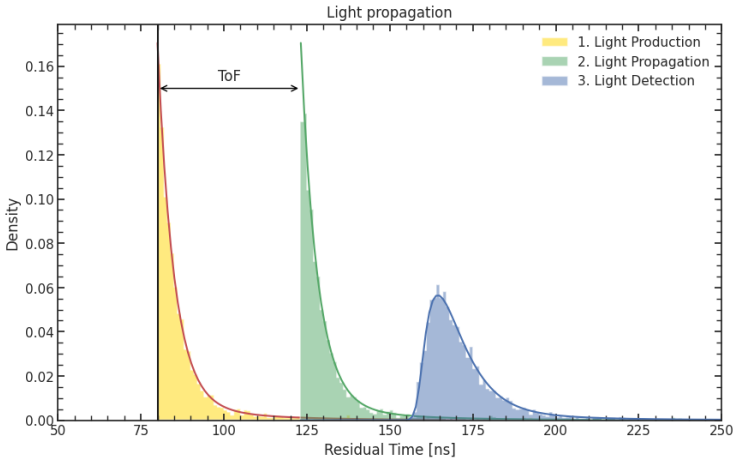


***Figure 5.5:*** *Hit times split by propagation phase: yellow (scintillation hits with red PDF), green (after adding ToF offset), and blue (after convolution with PMT response).*

Given a trial value of $t_0$, the expected hit time distribution over the whole detector can be recon-

structed. This is shown in Fig. 5.6, distinguishing between PMTs in water and in LS, for the same event depicted in Fig. 5.4.

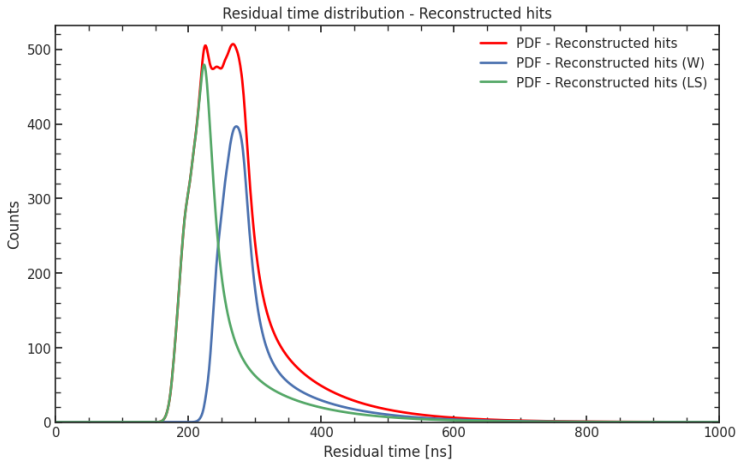


***Figure 5.6:*** *Reconstructed hit time distribution for a single event. Red: all PMTs; light blue and green: PMTs in water and in LS, respectively.*

Figure 5.7 compares the experimental hit time distribution to the one reconstructed using the parametrization described above. The peak is well-reproduced, while discrepancies in the tail highlight current limitations of the model, which are discussed in the following paragraph.

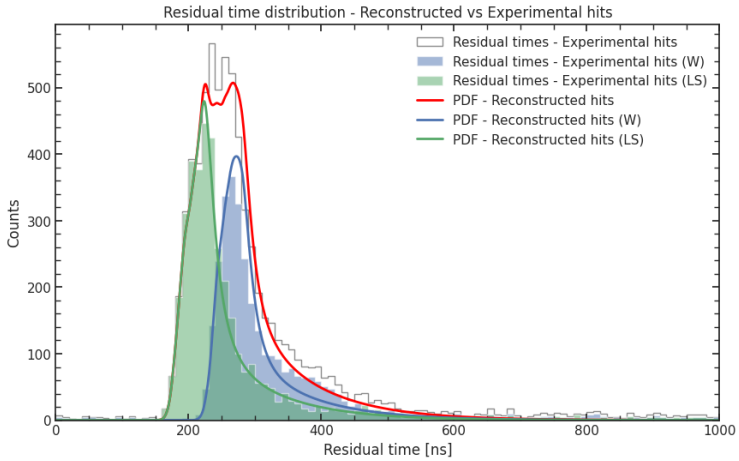


***Figure 5.7:*** *Comparison of experimental (histograms) and reconstructed (continuous lines) hit time distributions for a single event.*

After modeling the detector's full time response for a single event, the likelihood function is defined over all PMTs as:

$$\mathcal{L}(\vec{r}_0, t_0 | t^i_{res}) = \prod_i p(t^i_{res}) \tag{5.11}$$

where $p(t^i_{res})$ is the convolution of single PDF $f(t^i_{res})$ of the residual time for the $i$-th Hit. The vertex and the interaction time $t_0$ are obtained by maximizing $\mathcal{L}$, or equivalently minimizing the quantity

$-\log \mathcal{L}$ using the TMinuit package [68]. An example of the $\chi^2$ profile minimized for an event with a calibration AmBe source at $V = (x, y, z) = (0, 0, 10.5)$ - recovered within $1\sigma$ - is shown in Fig. 5.8, highlighting the best fit, the $1\sigma$ confidence region, and the true vertex.

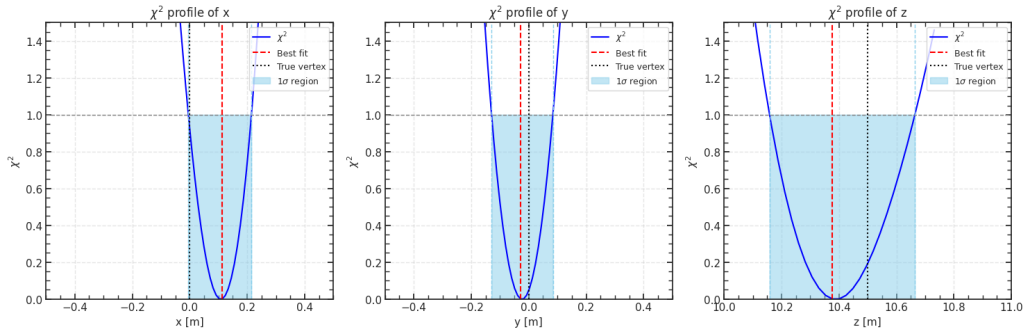


***Figure 5.8:*** *$\chi^2$ distribution for the three reconstructed vertex coordinates. The $1\sigma$ region is shown in blue, the best fit in red, and the true vertex in black.*

### 5.2.3 Algorithm performances

Before proceeding with the construction of the non-uniformity map by tagging the positions of spallation neutrons, in this section the reconstruction algorithm is applied to several runs to validate its performance.

Since Eq. 5.11 depends on three components (scintillation, ToF, and PMT response), the first check was performed using a laser source placed at the detector center, emitting isotropically at $\lambda = 420\,\text{nm}$, a wavelength not reabsorbed by the LS. This configuration "suppresses" the scintillation component in Eq. 5.11, leaving only the contributions from ToF (whose performance has been separately evaluated through comparison with MC simulations, see Fig. 3.8) and the timing response of individual PMTs. Figure 5.9 shows the reconstructed vertex distribution projected onto the (x,z) and (y,z) planes for the laser run.

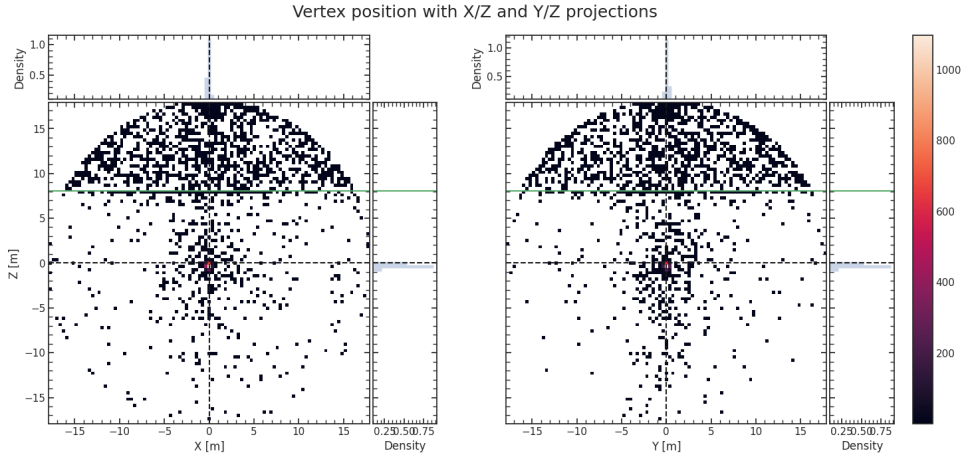


***Figure 5.9:*** *Bidimensional distribution in linear scale on the (x,z) and (y,z) planes of reconstructed vertices from a laser run with theoretical vertex (black dashed lines) at the center of the detector. The green line represents the Water-LS interface level.*

The events are well reconstructed and follow the detector shape, with the background predominantly located in the LS-filled region, as expected. A zoom around the detector center (shown in Fig. 5.10 in log scale) provides a more detailed view of the reconstruction.

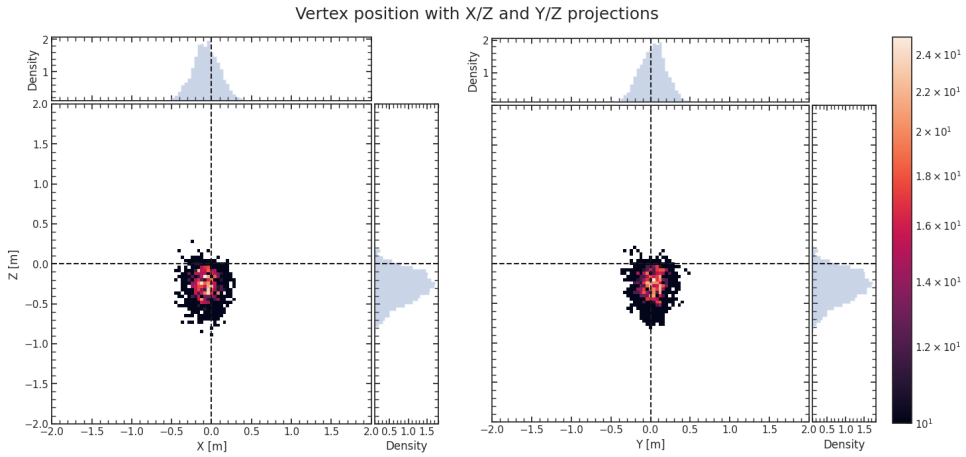


***Figure 5.10:*** *Bidimensional distribution in logarithmic scale with zoom around the true vertex, in the (x,z) and (y,z) planes of reconstructed vertices from a laser run with theoretical vertex (black dashed lines) at the detector center. The green line indicates the Water-LS interface.*

The reconstruction in the $(x, y)$ plane appears accurate, while a slight bias is observed in the $z$ direction (note that the scale is logarithmic and the zoom is on a narrow region around the origin). To quantify the spatial resolution and accuracy, Fig. 5.11 shows the distribution of the difference between reconstructed and true event vertices, with a superimposed Gaussian fit with constant background.

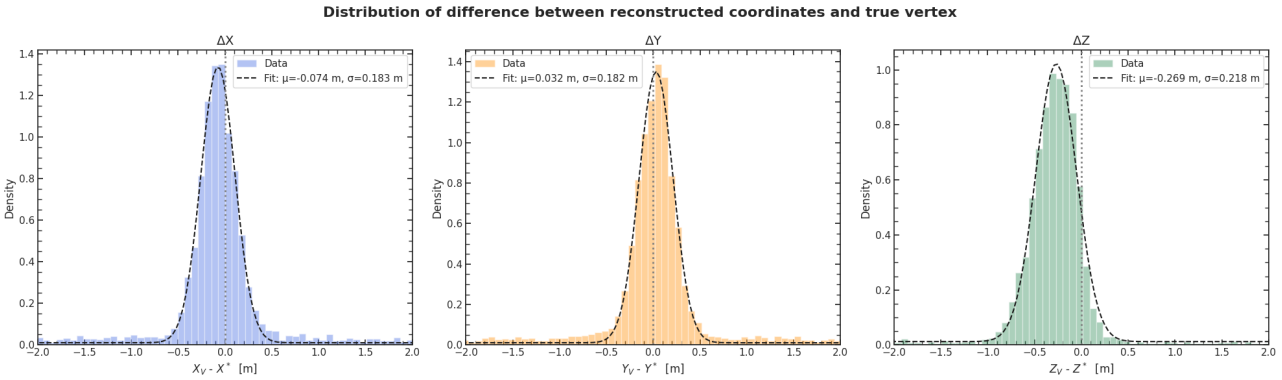


***Figure 5.11:*** *Distribution of the difference between reconstructed and true vertices for a laser run, with a Gaussian fit with constant background overlaid to estimate the centroid μ (displacement from the true value) and σ (an indicator of the reconstruction resolution).*

These fits confirm the previous observation: the bias mainly affects the $z$ coordinate, where the spatial resolution is also slightly worse ($\sigma_z = 21.8\,\text{cm}$) compared to the other two coordinates ($\sigma_x = \sigma_y = 18.2\,\text{cm}$). This bias could originate from several factors, but some indications point to the breaking of spherical symmetry. In particular, as already shown in Chapter 3, comparison with MC revealed the presence of some PMTs near the top and the interface region with ToF values deviating from ex-

pectations. This asymmetry in $z$ could contribute to the observed shift. Another possible explanation lies in the parameterization of individual PMT time responses: as discussed in Chapter 3, some GCU groups appear to be unpredictably shifted by $\pm 8$ ns, even after procedures like PTP. This could have a larger impact on the $z$ coordinate reconstruction in this hybrid detector phase, where symmetry is not yet fully achieved.

To confirm that the resolution degradation is limited to this coordinate, the same study presented for the laser run was repeated using AmBe runs with the source placed along the detector central axis ($(x, y) = (0, 0)$ m) at different $z$ positions. The values of $\mu$ (displacement from the true vertex) and $\sigma$ (spatial resolution) for the three coordinates at various source heights are shown in Fig. 5.12.

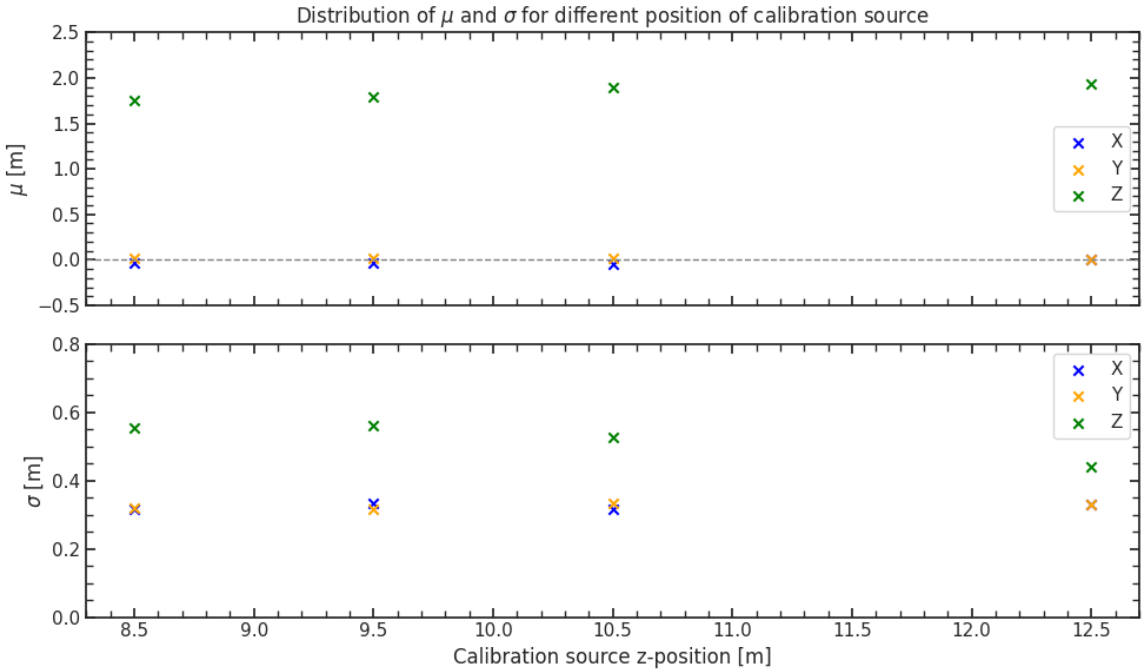


***Figure 5.12:*** *Distributions of $\mu$ (displacement from the true value) and $\sigma$ (indicator of reconstruction resolution) for AmBe runs at various $z$ positions, with constant $(x, y) = (0, 0)$.*

From Fig. 5.12 and the analysis in this section, the following conclusions can be drawn:

- The bias primarily affects the $z$ coordinate, while the reconstructed position is compatible within resolution in the $(x, y)$ plane. Given the current hybrid configuration of the detector (i.e., ongoing LS filling and coexistence of Water and LS), the breaking of spherical symmetry likely explains the observed shift in $z$, to be more carefully assessed one filling will be completed;
- The spatial resolution for the $x, y$ coordinates is approximately constant at around 30 cm for events occurring in the LS, and it remains uniform across different positions. A further improvement is expected by including information on the amount of collected charge—an approach that becomes feasible only after developing the non-uniformity map, which is the subject of Section 5.3.

Overall, the algorithm—although still under development—already shows robust performance. The

reconstruction time for a single event is on the order of 1 second (parallelized across multiple CPUs and implemented in Python) if provided with a good initial guess for the vertex (from the CCM, whose execution time is negligible) and is further reduced when disabling the numericall sollving of Snellls law for refractioon in the ToF map computation. The algorithm is also versatile, allowing the configuration of key parameters at runtime, such as: $\tau_i$, weights of the various scintillation components, $n_W$, $n_{LS}$, numerical solver and tolerance for the ToF map, as well as options to enable or disable refraction at the interface—making it ready for post-filling operation.
In the next section, the algorithm will be used to reconstruct the position of already-tagged spallation neutron events (associated with muon passage). This will enable the construction of a light yield (LY) map as a function of radial distance (i.e., non-uniformity map), which will contribute to improving the energy resolution of the detector.

## 5.3 Energy Non-Uniformity Map and Energy Resolution Improvement

At this stage, all the necessary components are available to construct a non-uniformity map during a delicate phase such as the LS filling, in which the detector configuration varies on an hourly basis and it is not possible to perform calibrations with the same frequency as during full operation. The choice of spallation neutrons as a homogeneous, constant, and isotropic calibration source solves the issue of interrupting the filling process to position calibration sources at specific locations within the detector. The event selection algorithm, based on the off-window technique developed in Chapter 4, is both validated and efficient, allowing for the tagging of events related to muon passages with high efficiency and purity. Moreover, the interaction vertex reconstruction algorithm discussed in this chapter—based solely on the detector's time response and taking into account the dynamic conditions of the commissioning phase—provides a good reconstruction of the interaction vertex.
To construct the non-uniformity map, runs taken under the same detector configuration were selected, and the detector was divided into radial shells (in a spherical coordinate system centered at the origin) with a step size of 1 m, in the range from 4 to 17.9 m. The choice to start from $R_{min} = 4\,\mathrm{m}$ was made solely due to event statistics: the number of spallation neutrons captured in a radial shell at the center of the detector (i.e., in a smaller LS volume) during a phase in which the filling has just reached the equator is significantly lower than the number of events at the edges (where spallation neutrons produced by muons crossing the WP or, more likely, the surrounding rock of the mountain above JUNO are also present). In order to avoid biases due to lack of statistics it was chosen to select events starting from $R_{min} = 4\,\mathrm{m}$ since — based on the simulations reported in [20] — the variation of the LY is less sensitive for radial shells below 4 m. Therefore, the absence of significant data points in this region does not limit the construction of an effective map to be applied for improving the detector's energy resolution. For each radial shell, spallation neutrons were identified, and a fit was applied as shown in Fig. 4.12, from which an estimate of the LY was obtained using Eq. 4.22, depending on the radial shell. The resulting non-uniformity map is shown in Fig. 5.13. It should be noted that the estimated LY (reported on the vertical axis in Fig. 5.13) also includes PEs produced by DN, which are not associated with any energy deposition in the detector. This DN contribution must be independently estimated and subtracted in order to quantify the effective LY.

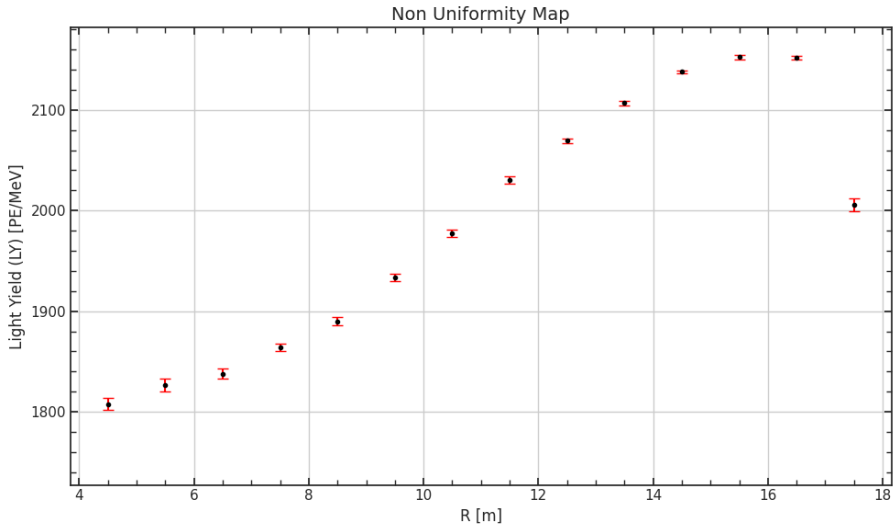


***Figure 5.13:*** *Non-uniformity map showing the trend of LY (in number of photoelectrons per MeV of deposited energy) as a function of the radial distance R from the center of the detector.*

Starting from the detector center, the gradual increase is a combined effect of variations in active photon coverage and the attenuation of optical photons [20]. The sharp decrease close to 16.5 m is due to the mismatch of the indices of refraction between the LS, acrylic and water - the closer the event to the edge, the more likely is the occurrence of total reflection and consequently, the loss of photons by absorption. Although this map represents a discrete profile, interpolation between neighboring points allows for calibration over finer radial shells than 1 m. This procedure was applied to the spallation neutron spectrum shown in Fig. 4.13: the interaction vertex of each event in the spectrum was reconstructed, and the correction introduced by the map in Fig. 5.13 was applied. The resulting corrected spectrum, along with the uncorrected one, is shown in Fig. 5.14.

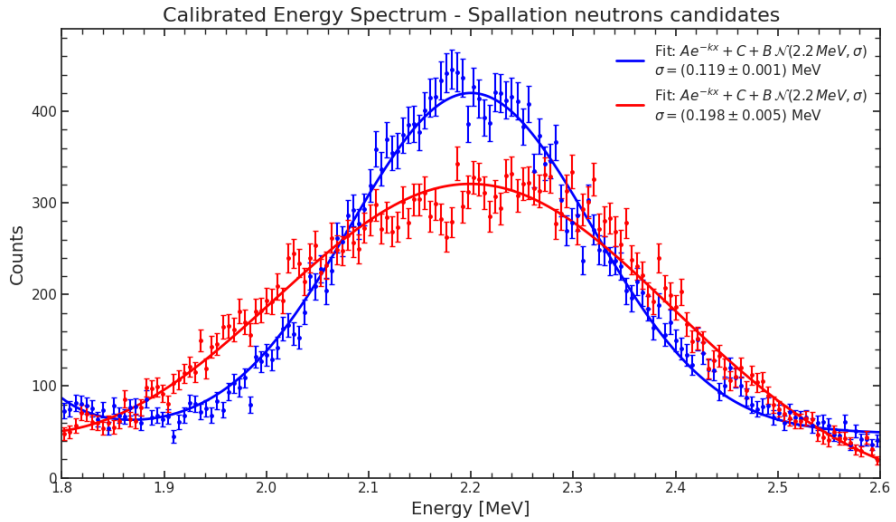


***Figure 5.14:*** *Calibrated energy spectrum of spallation neutrons before (red) and after (blue) applying the correction from the non-uniformity map. Gaussian fits are superimposed to both spectra to estimate the energy resolution.*

It can be seen that the energy resolution improves of approximately $40\%$ after applying the non-uniformity correction, going from $9\%$ before the correction to $5.4\%$ afterward. Although the improvement is significant, the resulting value is still above the requirements set by the collaboration. Possible reasons for this residual degradation include:

- The non-uniformity map was constructed in a purely radial form, thus ignoring variations in $\theta$ and $\phi$, which are expected and relevant because of the structure of the stainless steel [69]-[70]. Enhancing the map in this direction would make it more sensitive to vertex-dependent variations and allow for a more effective correction on top of the one already introduced;
- Also, the vertex reconstruction precision can significantly affect the accuracy of the non-uniformity map, leading to a deterioration of the energy resolution. The inclusion of addition information in the likelihood (e.g. information on the spatial deposition of charge) is expected to further enhance the precision of the reconstruction algorithm.

Regarding the objective of this chapter—namely, to investigate the main contributions to the degradation of the energy resolution in JUNO during the commissioning phase—the approximately 40% improvement achieved by including the non-uniformity map represents a solid starting point for future refinements. These efforts should be carried out under full operational conditions and should account for additional sources of resolution degradation, which are critical for achieving the energy precision required to resolve the NMO problem. Nonetheless, they already represent a promising step forward, demonstrating how the characterization of the detector's spatial response can bring us closer to the target resolution.

# 6

# Conclusions

This thesis work has encompassed a broad range of analyses, all carried out during JUNO's delicate and transitional commissioning phase and LS-filling. The JUNO experiment is expected to complete filling by August 2025, with full-scale data taking starting in September 2025. Among its many ambitious goals, JUNO aims to resolve the NMO within six years of operation. Already within its early months, JUNO is expected to measure several neutrino oscillation parameters with unprecedented precision, positioning the experiment as a global leader in the field of neutrino oscillation physics. To meet these ambitious scientific goals, JUNO must fulfill strict requirements, particularly regarding sufficient statistics and exceptional energy resolution.

The first of these requirements, assuming a fixed exposure, is inherently linked to the ability to efficiently select IBD candidate events. In this thesis, special attention was dedicated to the development of an event selection algorithm capable of identifying correlated events of various types with high efficiency and purity. The algorithm was validated and then used to conduct two parallel analyses: one focused on the radiopurity of the LS, and the other on spallation neutrons. The first of these analyses is particularly relevant during the filling phase, as the collaboration has set an upper limit on the contamination from $^{238}$U in the LS. The only reliable way to verify the scintillator's quality is by analyzing the experimental data recorded directly by the detector. To this end, the fast coincidence between the $\beta$-decay of $^{214}$Bi and the subsequent $\alpha$-decay of $^{214}$Po was tagged, enabling hourly monitoring of $^{222}$Rn contamination and the extraction of a contamination level for $^{238}$U. The measured values, obtained fitting with fixed (free) $\tau_{^{222}Rn}$, of $C_{^{238}U}^{\tau_{^{222}Rn}^{\text{fixed}}} = (2.8 \pm 1.2) \cdot 10^{-16} g/g$ ($C_{^{238}U}^{\tau_{^{222}Rn}^{\text{not fixed}}} < 7.5 \cdot 10^{-16} g/g$ @ 68% CI) were found to be consistent with the collaboration's requirements.

The second key requirement for JUNO is its unprecedented energy resolution target for a detector of its kind: $3\%$ at 1 MeV. This resolution depends on several parameters, one of which—spatial non-uniformity in the detector's response—can be calibrated and corrected by characterizing the spatial response of the detector. Specifically, it concerns variations in the number of PE produced per MeV

of deposited energy at different locations inside the detector. The second part of this thesis addressed precisely this aspect. The previously tagged spallation neutrons were used as a uniform, stable, and homogeneous calibration source throughout the detector volume. A vertex reconstruction algorithm was developed to determine their positions, using the timing response of 17,612 LPMTs. The detector's timing behavior was studied in detail, particularly during laser calibration campaigns carried out during commissioning. The PMTs' timing response was parametrized, and a parallel study was performed on the synchronization procedures of the GCUs. A numerical ToF map was also constructed, accounting for optical path distortions due to refraction effects in the current hybrid water-LS configuration. Together, these elements allowed modeling the detector's timing response, building a time-based likelihood, and using it to estimate the interaction vertex. Combining this vertex reconstruction with the event selection algorithm for spallation neutrons enabled the construction of a non-uniformity map, ultimately improving energy resolution by approximately $40\%$.

Several possible extensions of this work can be envisioned, including:

- Application of the event selection algorithm to tag IBD candidate events. This would be of practical interest both for oscillation analyses and for the extraction of oscillation parameters in the early data-taking phase, as well as for the complete reactor spectrum needed to resolve the NMO within the first six years of operation.
- Further development of the time-based vertex reconstruction algorithm, particularly by implementing simultaneous energy reconstruction while accounting for non-uniformity. The algorithm could also be enhanced by incorporating the detector's charge response or considering secondary light propagation effects, such as total internal reflection or multiple scattering.

# A

# Detailed IBD kinematics and cross section

The explicit expressions for IBD, namely quasielastic scattering of electron antineutrino on proton, is:

$$\bar{\nu}_e\,(p_\nu) + p\,(p_p) \longrightarrow e^+\,(p_e) + n\,(p_n) \tag{A.1}$$

Let us define

$$\Delta = m_n - m_p = 1.293\ MeV \tag{A.2}$$

$$M = \frac{m_p + m_n}{2} \approx 938.9 MeV \tag{A.3}$$

The differential cross section at **tree level** in the weak interactions, averaged (summed) over initial (final) polarizations is [71]:

$$\frac{d\sigma}{dt} = \frac{G_F^2 cos^2\theta_C}{2\pi(s - m_p^2)^2} \cdot |\mathcal{M}|^2 \tag{A.4}$$

where $G_F = 1.16637 \cdot 10^{-5}\ GeV^{-2}$ is the Fermi coupling (extracted from $\mu$-decay [72]), $cos\theta_C = (0.9746 \pm 0.0008)$ is the cosine of the Cabibbo angle [73] and $\mathcal{M}$ has the well-known current-current structure:

$$\mathcal{M} = \left[\bar{v}_{\bar{\nu}_e}\gamma^\mu(1-\gamma_5)v_e\right] \cdot \left[\bar{u}_n(f_1\gamma_\mu + g_1\gamma_\mu\gamma_5 + \frac{if_2}{2M}\sigma_{\mu\nu}q^\nu + \frac{g_2\gamma_5}{M}q_\mu)u_p\right] \tag{A.5}$$

where $q = p_\nu - p_e = p_n - p_p$. A straightforward calculation yields [71]:

$$|\mathcal{M}|^2 = A(t) - (s-u)B(t) + (s-u)^2C(t) \tag{A.6}$$

where s,t,u are the usual Mandelstam variables defined as

$$\begin{cases} s = (p_\nu + p_p)^2 \\ t = (p_\nu - p_e)^2 \\ u = (p_\nu - p_n)^2 \end{cases} \tag{A.7}$$

And

$$A(t) = \frac{1}{16}(t - m_e^2)\Bigg[4|f_1|^2(4M^2 + t + m_e^2) + 4|g_1|^2(-4M^2 + t + m_e^2) + |f_2|^2\left(\frac{t^2}{M^2} + 4t + 4m_e^2\right)$$
$$+ 4m_e^2 t\frac{|g_2|^2}{M^2} + 8\mathrm{Re}[f_1^* f_2](2t + m_e^2) + 16m_e^2\mathrm{Re}[g_1^* g_2]\Bigg]$$
$$- \Delta^2\Bigg[(4|f_1|^2 + t\frac{|f_2|^2}{M^2})(4M^2 + t - m_e^2) + 4|g_1|^2(4M^2 - t + m_e^2)$$
$$+ 4m_e^2\frac{|g_2|^2}{M^2}(t - m_e^2) + 8\mathrm{Re}[f_1^* f_2](2t - m_e^2) + 16m_e^2\mathrm{Re}[g_1 g_2]\Bigg] - 32m_e^2 M\Delta\mathrm{Re}[g_1^*(f_1 + f_2)]$$

$$B(t) = \frac{1}{16}\left[16t\mathrm{Re}[g_1^*(f_1 + f_2)] + 4m_e^2\Delta\frac{\left(|f_2|^2 + \mathrm{Re}[f_1^* f_2 + 2g_1^* g_2]\right)}{M}\right]$$

$$C(t) = \frac{1}{16}\left[4(|f_1|^2 + |g_1|^2) - t\frac{|f_2|^2}{M^2}\right]$$

The adimensional form factors $f_i, g_i$ are real functions of the transferred 4-momentum $t$ and they can be approximated by [74]

$$f_1 = \frac{1 - \frac{(1+\xi)t}{4M^2}}{(1 - \frac{t}{4M^2})(1 - \frac{t}{M_V^2})^2} \tag{A.8}$$

$$f_2 = \frac{\xi}{(1 - \frac{t}{4M^2})(1 - \frac{t}{M_V^2})^2} \tag{A.9}$$

$$g_1 = \frac{g_1(0)}{(1 - \frac{t}{M_A^2})^2} \tag{A.10}$$

$$g_2 = \frac{2M^2 g_1}{m_\pi^2 - t} \tag{A.11}$$

where $g_1(0) = (-1.270 \pm 0.003)$ [73], $M_V^2 = 0.71 GeV^2, M_A^2 \approx 1 GeV^2$. Finally $\xi = \kappa_p - \kappa_n = 1.792 - (-1.913) = 3.706$ is the difference between the proton and neutron anomalous magnetic moments in units of the nuclear magneton.

Our final expression is somewhat involved but allows to numerically compute any desired integrated cross-section. It is also useful to present some simple analytic approximation [71] that is valid at low energies (say, at supernova and reactor energies or below). In these approximation form factors are approximated with constants.

- Leading Order (LO) approximation:

$$A \approx M^2(f_1^2 - g_1^2)(t - m_e^2) - M^2\Delta^2(f_1^2 + g_1^2)$$
$$B \approx 0$$
$$C \approx \frac{f_1^2 + g_1^2}{4}$$

- Non Leading Order (NLO) approximation:

$$A \approx M^2(f_1^2 - g_1^2)(t - m_e^2) - M^2\Delta^2(f_1^2 + g_1^2) - 2m_e^2 M\Delta g_1(f_1 + f_2)$$
$$B \approx t g_1(f_1 + f_2)$$
$$C \approx \frac{f_1^2 + g_1^2}{4}$$

**Rewriting $\frac{d\sigma}{dt}$ in terms of $E_\nu, E_e$**

The cross section expressed in terms of the neutrino and electron energy in the rest frame of the proton, $E_\nu$ and $E_e$, is particularly useful [71]. Inserting

$$\begin{cases} s = 2m_p E_\nu + m_p^2 \\ u = s - 2m_p(E_\nu + E_e) - m_e^2 \\ t = m_n^2 - m_p^2 - 2m_p(E_\nu - E_e) \end{cases} \tag{A.12}$$

it is given by

$$\frac{d\sigma}{dE_e}(E_\nu, E_e) = 2m_p \frac{d\sigma}{dt} \qquad \text{If:} \qquad E_\nu \geq E_{thr} = \frac{(m_n + m_e)^2 - m_p^2}{2m_p} \tag{A.13}$$

The allowed values of $E_e$ correspond to the possible scattering angles $\theta_{CM}$ in the Center of Mass (CM) frame are:

$$E_1 = E_\nu - \frac{m_n^2 - m_p^2 - m_e^2}{2m_p} - \frac{1}{m_p}E_\nu^{CM}(E_e^{CM} - p_e^{CM}) \leq E_e \leq E_\nu - \frac{m_n^2 - m_p^2 - m_e^2}{2m_p} - \frac{1}{m_p}E_\nu^{CM}(E_e^{CM} + p_e^{CM}) = E_2 \tag{A.14}$$

where the energy and momenta in the CM have the standard expressions:

$$E_\nu^{CM} = \frac{s - m_p^2}{2\sqrt{s}} \tag{A.15}$$
$$E_e^{CM} = \frac{s - m_n^2 + m_e^2}{2\sqrt{s}} \tag{A.16}$$
$$p_e^{CM} = \frac{\sqrt{[s - (m_n - m_e)^2][s - (m_n + m_e)^2]}}{2\sqrt{s}} \tag{A.17}$$

### Corrections

We can include also two corrections:

- Radiative corrections [75]-[76]: well approximated as

$$d\sigma(E_\nu, E_e) \rightarrow d\sigma(E_\nu, E_e)\left[1 + \frac{\alpha}{\pi}\left(6 + \frac{3}{2}log\left(\frac{m_p}{2E_e}\right) + 1.2 \cdot \left(\frac{m_e}{E_e}\right)^{1.5}\right)\right] \tag{A.18}$$

  where $\alpha$ is the fine-structure constant.

- Final-state corrections: multiply $\sigma(\nu_e n \rightarrow pe)$ by the Sommerfeld factor

$$F(E_e) = \frac{\eta}{1 - e^{-\eta}} \qquad \text{With:} \qquad \eta = \frac{2\pi\alpha}{\sqrt{1 - \frac{m_e^2}{E_e^2}}} \tag{A.19}$$

Both the radiative corrections and final state interactions amount to a $\approx 2\%$ correction [71], which can be important for high statistic data samples.

### Angular distribution

We conclude with an analysis of the angular distribution [71]. The cross section differential in the angle $\theta$ between the neutrino and the positron is obtained from $\frac{d\sigma}{dt}$ after including the Jacobian coming from $t = m_e^2 - 2E_\nu(E_e - p_e cos(\theta))$:

$$\frac{d\sigma}{dcos(\theta)}(E_\nu, cos(\theta)) = \frac{p_e \frac{E_\nu}{m_p}}{1 + \frac{E_\nu}{m_p}(1 - \frac{E_e}{p_e}cos(\theta))} \cdot \frac{d\sigma}{dE_e} \tag{A.20}$$

In Eq. A.20, $E_e$ and $p_e$ are functions of $E_\nu$ and $\theta$:

$$\begin{cases} E_e &= \frac{(E_\nu - \frac{m_n^2 - m_p^2 - m_e^2}{2m_p})(1+\frac{E_\nu}{m_p}) + \frac{E_\nu}{m_p}cos(\theta)\sqrt{(E_\nu - \frac{m_n^2 - m_p^2 - m_e^2}{2m_p})^2 - m_e^2[(1+\frac{E_\nu}{m_p})^2 - (\frac{E_\nu}{m_p}cos(\theta))^2]}}{(1+\frac{E_\nu}{m_p})^2 - (\frac{E_\nu}{m_p}cos(\theta))^2} \\ p_e &= \sqrt{E_e^2 - m_e^2} \end{cases} \tag{A.21}$$

For $\bar{\nu}_e$ a non trivial allowed range of $\theta$ is obtained only in a very small region energy range just above the threshold $E_{thr}$ (given in Eq. A.13):

$$E_{thr} \leq E_\nu \leq E'_{thr} = E_{thr} + m_e \frac{[m_n - (m_p - m_e)]^2}{2m_p(m_p - m_e)} \tag{A.22}$$

For the $e$ we have $E' - E_{thr} = 1eV$. Above $E'$ all scattering angles are allowed. Therefore, we can conveniently simplify $\bar{\nu}_e$, scatterings by replacing $E_{thr}$ with $E'$ and considering the full range $\theta = [0, \pi]$. This is a very good approximation.

# B

# Solar neutrinos detection in JUNO

Solar neutrinos [77] are produced with electron flavor ($\nu_e$) in the hydrogen-to-helium fusion reactions occurring in the Sun's core. This fusion proceeds through two distinct mechanisms: the dominant proton-proton (pp) chain and the subdominant CNO cycle. In the latter process, Carbon, Nitrogen, and Oxygen act as catalysts for the fusion. The CNO cycle contributes only $\approx 1\%$ to the solar energy production, with significant uncertainty due to poor constraints on the Sun's metallicity (the abundance of elements heavier than Helium).
Solar neutrinos produced in each reaction of either the pp chain or CNO cycle exhibit characteristic energy spectra as shown in Fig. B.2.

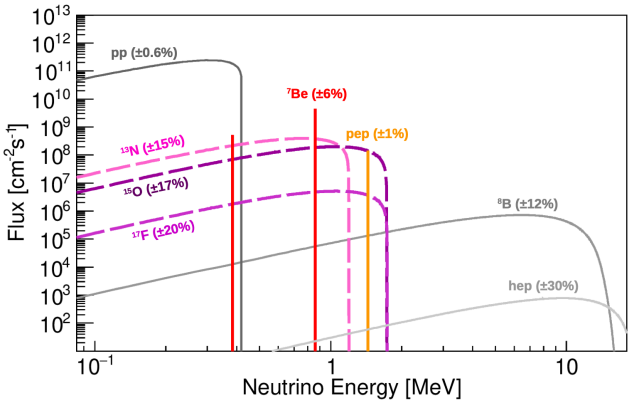


***Figure B.1:*** *Energy spectra of solar neutrinos from the pp chain (solid lines) and CNO cycle (dashed lines). The flux (vertical scale) is given in units of $cm^{-2}s^{-1}MeV^{-1}$ for continuum sources and $cm^{-2}s^{-1}$ for monoenergetic sources. Parentheses indicate the corresponding relative uncertainties of the Standard Solar Model (SSM) predictions.*

The SSM describes a one-solar-mass star in hydrostatic equilibrium. The model is calibrated to satisfy constraints from present-day solar luminosity, radius, mass, and surface metal-to-hydrogen abundance ratio (Z/X, referred to as solar metallicity). Solar neutrino fluxes are among the outputs of the SSM, along with other relevant observables such as the sound speed profiles at the Sun's surface.

Solar metal abundances can be measured through spectroscopy of the solar surface. However, over the past two decades, spectroscopic analyses have yielded controversial results - the so-called Low-Metallicity (LZ) [78]-[79] and High-Metallicity (HZ) measurements [80]-[81]. Precise measurements of solar neutrino fluxes, particularly CNO neutrinos, may help resolve this discrepancy. The HZ and LZ models predict different fluxes for 7Be, 8B, and CNO neutrinos, with differences of 8.9%, 17.6%, and 30% respectively, because metallicity affects the solar plasma opacity, which in turn influences the Sun's temperature and fusion rates. Electron-flavor solar neutrinos undergo flavor transformation during propagation through dense solar matter due to coherent forward scattering off electrons - the Mikheyev–Smirnov–Wolfenstein (MSW) effect [82]-[83]. The survival probability ($\mathcal{P}_{ee}$) is dominated by vacuum oscillations below 1 MeV ($\mathcal{P}_{ee} = 0.54$) and by matter effects above 8 MeV ($\mathcal{P}_{ee} = 0.32$), with a smooth transition at intermediate energies [84]-[85].
In JUNO, solar neutrinos of all flavors are detected through Elastic Scattering (ES) off electrons:

$$\nu_x + e^- \rightarrow \nu_x + e^- \quad \text{where } x = e, \mu, \tau \tag{B.1}$$

This process has no intrinsic energy threshold. The cross section for electron neutrinos ($\nu_e$) is approximately six times larger than for non-electron flavors ($\nu_\mu$ and $\nu_\tau$), as only $\nu_e$ can interact via both charged and neutral currents. In elastic scattering, only a fraction of the neutrino energy $E_\nu$ is transferred to the electron, which produces scintillation light proportional to its kinetic energy $E_{kin}$. Even for mono-energetic neutrino sources like $^7$Be and pep neutrinos, this results in a continuous electron recoil spectrum. Directional information is largely lost because isotropic scintillation light dominates over the sub-percent level Cherenkov light contribution.
Achieving its physics goals requires JUNO to maintain extremely high radiopurity standards. This is particularly crucial for solar neutrino analysis, where neutrino elastic scattering events cannot be distinguished from background events on an individual basis, as both produce single flashes of light without the possibility of coincidence techniques (unlike the IBD reaction used for reactor antineutrino detection). Additionally, the isotropic nature of scintillation light prevents the use of directional information for background rejection. Consequently, JUNO's sensitivity to solar neutrinos is strongly dependent on the type and amount of detector backgrounds.
The neutrino signal can be extracted by fitting the energy distribution of detected events, modeled as the sum of neutrino and background contributions. The fit requires probability density functions (PDFs) for each background and signal component, and returns their respective event counts. This strategy, successfully implemented in Borexino's solar neutrino spectroscopy [86]-[87]-[88], will be even more effective in JUNO thanks to its superior energy resolution and larger mass. An example expected spectrum, highlighting the cycles under the baseline radiopurity scenario (i.e., U/Th contamination below $10^{-16}$g/g), is shown on the right.

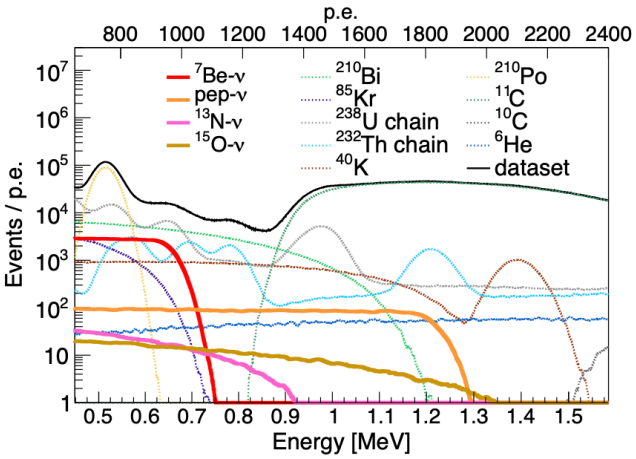


***Figure B.2:*** *Contributions from all neutrino and background species considered for the sensitivity analysis of six years of data taking in the baseline radiopurity scenario. Solar neutrino contributions are shown as solid lines respectively, while background contributions appear as dotted lines.*

Sensitivity studies [77] indicate that JUNO will measure solar neutrino rates with uncertainties competitive with current state-of-the-art measurements. Specifically, after six years of data taking (under baseline radioactivity conditions):

- For $^{7}$Be neutrinos, uncertainties will reach the percent level, while pep neutrino uncertainties will range from 3% to 17% (depending on radiopurity).
- CNO neutrino uncertainties will achieve 12% to 19% precision (radiopurity-dependent). Moreover, JUNO may perform the first individual measurements of the two main CNO flux components: $^{13}$N and $^{15}$O solar neutrinos.

# C

# Radioactive decay

This brief appendix recalls some concepts related to radioactive decay, including the definition of activity and the relations among the activities in a decay chain.

If $N$ radioactive nuclei are present at time $t$ and no new nuclei are introduced into the system, then the number $dN$ decaying in a time interval $dt$ is proportional to $N$. This leads to the definition of the decay constant $\lambda$ [89]:

$$\lambda = -\frac{\left(\frac{dN}{dt}\right)}{N} \tag{C.1}$$

Integrating Eq. C.1 yields the exponential law of radioactive decay:

$$N(t) = N_0 e^{-\lambda t} \tag{C.2}$$

where $N_0$ is the initial number of nuclei at $t = 0$. The half-life $t_{1/2}$ is the time required for half of the nuclei to decay. Setting $N = \frac{N_0}{2}$ in Eq. C.2 gives:

$$t_{1/2} = \frac{\ln(2)}{\lambda} \tag{C.3}$$

It is also useful to define the mean lifetime $\tau$, which corresponds to the average time a nucleus survives before decaying:

$$\tau = \frac{1}{\lambda} \tag{C.4}$$

Furthermore, differentiating Eq. C.2 yields:

$$\left|\frac{dN}{dt}\right| = \lambda N_0 e^{-\lambda t} \tag{C.5}$$

The activity $\mathcal{A}(t)$, defined as the number of decays per unit time, is therefore:

$$\mathcal{A}(t) = \lambda N(t) = \mathcal{A}_0 e^{-\lambda t} \tag{C.6}$$

The activity of a radioactive sample is the number of decays per unit time. Its SI unit is the Becquerel (Bq), defined as one decay per second.

A common situation arises when a radioactive decay produces a daughter nucleus that is itself radioactive. This leads to decay series or chains of the form:

$$N_1 \rightarrow N_2 \rightarrow N_3 \rightarrow \cdots \rightarrow N_k \tag{C.7}$$

The original nucleus (type 1) is referred to as the parent, while the successive generations are called daughter (type 2), granddaughter (type 3), and so on. Denoting the decay constants by $\lambda_1, \lambda_2, \ldots$, and assuming that the $N_n$ daughter is the final stable product, the number of nuclei of the $i$-th type satisfies the following differential equation:

$$\frac{dN_i}{dt} = \lambda_{i-1} N_{i-1} - \lambda_i N_i \tag{C.8}$$

This number increases due to the decay of the parent and decreases due to its own decay. A general solution of Eq. C.8 for the case in which only $N_0$ nuclei of type 1 are initially present is given by the **Bateman equations** [90], where the number of nuclei of the $i$-th element is expressed as:

$$N_i = N_1(0) \sum_{k=1}^{i} c_k e^{-\lambda_k t} = N_0 \sum_{k=1}^{i} \left( \frac{\prod_{j=1}^{i} \lambda_j}{\prod_{\substack{j=1 \\ j \neq k}}^{i} (\lambda_j - \lambda_k)} \right) e^{-\lambda_k t} \tag{C.9}$$

A relevant case for this thesis is the one with $i = 2$.

Using Eq. C.9 with $i = 2$, we obtain:

$$N_2(t) = \lambda_1 N_1(0) \frac{1}{\lambda_2 - \lambda_1} \left( e^{-\lambda_1 t} - e^{-\lambda_2 t} \right) \tag{C.10}$$

and therefore:

$$\mathcal{A}_2(t) = \mathcal{A}_1(t) \frac{\lambda_2}{\lambda_2 - \lambda_1} \left( 1 - e^{-(\lambda_2 - \lambda_1)t} \right) \tag{C.11}$$

In our case:

$$\lambda_1 = \lambda_{^{238}\mathrm{U}} = \frac{\ln(2)}{t_{1/2}^{^{238}\mathrm{U}}} = 4.92 \cdot 10^{-18}\ \mathrm{s}^{-1} \tag{C.12}$$

$$\lambda_2 = \lambda_{^{222}\mathrm{Rn}} = \frac{\ln(2)}{t_{1/2}^{^{222}\mathrm{Rn}}} = 2.10 \cdot 10^{-6}\ \mathrm{s}^{-1} \tag{C.13}$$

Since $\lambda_1 \ll \lambda_2$ (so-called Secular Equilibrium condition), Eq. C.11 simplifies to:

$$\mathcal{A}_{222_{textRn}}(t) = \mathcal{A}_{^{238}\mathrm{U}} \left( 1 - e^{-\lambda_{222_{textRn}} t} \right) \tag{C.14}$$

To this term, a component of $^{222}$Rn must be added, which does not follow the secular equilibrium and

is introduced during filling activities. Taking this component into account and adding the one given by Eq. C.11, we end up with

$$\mathcal{A}_{^{222}\mathrm{Rn}}(t) = \mathcal{A}^{\text{Out of Equilibrium}}_{^{222}\mathrm{Rn}}(t) + \mathcal{A}^{\text{Secolar Equilibrium}}_{^{222}\mathrm{Rn}} = A \cdot e^{-\frac{t}{\tau_{^{222}\mathrm{Rn}}}} + \mathcal{A}_{^{238}\mathrm{U}} \tag{C.15}$$

Therefore, by fitting the time evolution of $\mathcal{A}_{^{222}\mathrm{Rn}}(t)$ (as shown in Fig. 4.9), it is possible to extract the value of $\mathcal{A}_{^{238}\mathrm{U}}$ as the plateau of the distribution.

# List of Acronyms

**A-Link** Asynchronous Link

**ACU** Automatic Calibration Unit

**ADC** Analog to Digital Converter

**AV** Acrylic Vessel

**BE** Back-End

**BEC** Back-End Card

**BEE** Back-End Electronics

**bis-MSB** 1,4-bis(2-methylstyryl)benzene

**CC** Charged Current

**CD** Central Detector

**CCM** Charge Center Method

**CDF** Cumulative Distribution Function

**CERN** Conseil européen pour la recherche nucléaire (*European Organization for Nuclear Research*)

**CFD** Constant Fraction Discriminator

**CIB** Calibration Interface Box

**CI** Credibility Interval

**CKM** Cabibbo-Kobayashi-Maskawa

**CLS** Cable Loop Systems

**CM** Center of Mass

**CTU** Central Trigger Unit

**DAQ** Data Acquisition

**DN** Dark Noise

**ES** Elastic Scattering

**FADC** Flash Analog-to-Digital Converter

**FE** Front-End

**FEC** Front-End Chip

**FEE** Front-end Electronics

**FV** Fiducial Volume

**FOC** Filling, Overflow, and Circulation

**FPGA** Field Programmable Gate Array

**GCU** Global Control Unit

**GSI** Gesellschaft für Schwerionenforschung (*Centre for Heavy Ion Research*)

**GT** Guide Tube

**HV** High Voltage

**HVU** High Voltage Unit

**HZ** High-Metallicity

**IBD** Inverse Beta Decay

**IO** Inverted Ordering

**JUNO** Jiangmen Underground Neutrino Observatory

**LAB** Linear Alkyl Benzene

**LPMT** Large-PMT

**LS** Liquid Scintillator

**LY** Light Yield

**LZ** Low-Metallicity

**MC** Monte Carlo

**MCP** Micro Channel Plate

**MSW** Mikheyev–Smirnov–Wolfenstein

**NC** Neutral Current

**NIM** Nuclear Instrument Module

**NMO** Neutrino Mass Ordering

**NNVT** North Night Vision Technology

**NO** Normal Ordering

**NPP** Nuclear Power Plant

**OEC** Online Event Classification

**OSIRIS** Online Scintillator Internal Radioactivity Investigation System

**PDG** Particle Data Group

**PDF** Probability Density Function

**PE** Photoelectron

**PMNS** Pontecorvo-Maki-Nakagawa-Sakata

**PMT** Photomultiplier Tubes

**PPO** 2,5-diphenyloxazole

**PTFE** Polytetrafluoroethylene

**PTP** Precision Time Protocol

**QE** Quantum Efficiency

**RMU** Reorganize and Multiplex Units

**ROV** Remotely Operated Vehicle

**S-Link** Synchronous Link

**SM** Standard Model

**SN** Supernovae

**SNO** Sudbury Neutrino Observatory

**sPMT** Small-PMT

**SSM** Standard Solar Model

**SyncE** Synchronous Ethernet

**ToF** Time of Flight

**TT** Transit Time

**TTIM** Trigger and Time Interface Mezzanine

**TTS** Transit Time Spread

**TTL** Transistor-Transistor Logic

**UV** Ultra Violet

**UWBox** Under Water Box

**WP** Water Pool

**WR** White Rabbit

# List of Figures


1.1 The two possible hierarchical neutrino mass scenarios with graphical representation of the neutrino flavor content of each of the neutrino mass eigenstates given the current preferred values of the oscillation parameters [4]. The precise value of the CP-violating phase in the leptonic sector remains unknown; consequently, it is varied $\delta$ within its entire CP range, ranging from $0$ to $2\pi$. Inspired by [6]. . . . . 6

1.2 Electron antineutrino survival probability $P_{ee}$ as a function of $L/E$. Left: effect of individual oscillation parameters. Right: comparison between NO and IO spectrum at maximum shift. . . . . 7

2.1 Location of the JUNO site. . . . . 10

2.2 Schematic view of the JUNO detector. Taken from [8]. . . . . 11

2.3 Flowchart of the liquid scintillator processing system. Taken from [12]. . . . . 12

2.4 Functional diagram of the types of LPMT present in JUNO. . . . . 14

2.5 JUNO LPMT readout electronics scheme. A description of the different parts is given in the text. Figure taken from [17]. . . . . 15

2.6 Overview of the calibration system (not to scale), including the ACU, two CLS, the GT, and the ROV. The red points represent a source assembly. The AURORA is an auxiliary laser diode system to monitor the attenuation and scattering length of the LS. . . . . 17

2.7 The expected antineutrino energy spectrum weighted by IBD cross-section with (grey, blue and red) and without (black) oscillation at the JUNO experiment for normal ordering (blue) and inverted (red) ordering assuming 6 years of data-taking. Dependence on the four oscillation parameters is shown. . . . . 19

2.8 Relative precision of the oscillation parameters as a function of JUNO data taking time. The markers and vertical lines stand for 100 days, 6 years, and 20 years of data taking. The horizontal gray dashed line stands for 1% relative precision. The green dotted and red dotted lines are on top of each other since the statistical-only precision is essentially identical for the $\Delta m^2_{31}$ and $\Delta m^2_{21}$ parameters. Taken from [38]. . . . . 20

2.9 Contours of $\Delta\chi^2_{\text{min}}$ as a function of exposure and energy resolution at 1 MeV under the assumption of NO. The resolution is scanned by varying a and fixing $b = 0.64 \times 10^2$, $c = 1.20 \times 10^2$ MeV. The black, gray, and green contour lines denote $3\sigma$, $4\sigma$, and $5\sigma$ significance levels, respectively. The top panel shows the time evolution of the $\Delta\chi^2_{\text{min}}$ for the energy resolution of 2.8%, 2.9%, and 3.0% at 1 MeV. The right panel shows the required energy resolution to $\Delta\chi^2_{\text{min}}$ under the JUNO exposure of 6.5 years ×26.6 GWth (data-taking time of 7.1 years with a reactor duty cycle of 11/12). Taken from [40]. . . 21

3.1 JUNO synchronization scheme overview. . . . . 24

3.2 IEEE 1588 PTP offset measurement. Taken from [44]. . . . . 26

3.3 Characteristic waveform with annotated features: signal (blue), baseline (black), threshold region (gray), HitTime (yellow), Rise-Time (purple), and charge integration interval (light blue). The inset demonstrates baseline calculation from the initial 200 ns distribution. Threshold is set at $V_{\text{baseline}} - 5\sigma_V^{\text{noise}}$ where $\sigma_V^{\text{noise}}$ is the baseline standard deviation. 28

3.4 CFD signal synthesis methodology . . . . . 29

3.5 Threshold region comparison: Leading-Edge (blue) versus CFD (black) with 1 ns sampling intervals . . . . . 29

3.6 Diagram (not to scale) of the propagation of a photon from a vertex at coordinates $(x_v, y_v, z_v)$ to the PMT at coordinates $(x_p, y_p, z_p)$, with the variables of interest highlighted. . . . . 30

3.7 Numerically computed ToF maps for two different interaction vertex positions. . . . . 34

3.8 Comparison between MC-simulated and numerically computed ToF values. . . . . 35

3.9 Schematic representation of the laser trigger timing not being synchronized (i.e., jitter error) with the trigger clock timing in the CTU. The Laser Trigger Signal is shown in red, the Trigger Clock in black, and the correction to the jitter error recorded by the CIB in blue. . . . . 37

3.10 Transit time distribution for a Hamamatsu PMT (yellow) and a NNVT PMT (blue), with the fit based on the model defined by *Equation* 3.22 overlaid. . . . . 37

3.11 Distribution of the TTS, extracted as $\sigma_{TTS}$ from the fit using the model defined by *Equation* 3.22, for all PMTs, separated into Hamamatsu (yellow) and NNVT (blue). . . . . 38

3.12 Distribution of time offsets (per PMT) between two runs following GCU hard reset, comparing Hamamatsu (yellow) and NNVT (blue) PMTs. Linear (left) and logarithmic (right) scales are shown. . . . . 39

3.13 Distribution of time offsets (per PMT) between runs pre-/post-PTP, comparing Hamamatsu (yellow) and NNVT (blue) PMTs. Linear (left) and logarithmic (right) scales are shown. . . . . 39

3.14 Channel distribution of unsynchronized PMTs (offset by one clock cycle) post-GCU reset (blue) and post-PTP (red). . . . . 40

4.1 Schematic illustration of an IBD reaction in the LS. The electron antineutrino interacts with a proton (p) in the LS, creating a positron ($e^+$) and a neutron (n). The positron deposits its energy and annihilates into two 0.511 MeV photons ($\gamma$), producing a prompt signal. After a random walk, the neutron is captured mainly by a free proton in the LS, emitting a 2.22 MeV $\gamma$-ray, and giving rise to a delayed signal. The time-charge diagram is not in scale. From [54]. . . . . 42

4.2 **Top:** Reconstructed energy spectra of JUNO in both the NO and IO scenarios without any statistical or systematic fluctuations (Asimov data). The neutrino oscillation parameters from PDG 2020 [1] are used to calculate the oscillation probability. The background spectra in the main figure are stacked, whereas those in the inset are plotted individually. **Bottom:** Relative contribution to $\Delta\chi^2$ and cumulative $\Delta\chi^2$ obtained when fitting the IO spectrum with the NO hypothesis. The results show that the most sensitive region for JUNO's NMO determination is 1.5–3 MeV. Taken from [40]. . . . . 44

4.3 Decay chain of $^{238}$U, with the type of decay highlighted. The numbers below each label indicate the half-life of the corresponding radionuclide. . . . . 47

4.4 Schematic representation of the "Off-window" algorithm for identifying correlated prompt-delayed events via statistical background subtraction. A muon event (purple) is followed by cosmogenic events (gray). The prompt-tagged event is shown in blue, the delayed event in green, and uncorrelated background events in red. The offset and $\Delta t$ values shown are those used in this thesis. For a detailed explanation of each selection step, refer to the text. . . . . 48

4.5 Example of BiPo event selection using the "Off-window" algorithm. The three columns show the prompt energy spectrum, delayed energy spectrum, and the $\Delta t$ between events. From top to bottom: (1) events in the "On-window" (i.e., correlated BiPo signals + uncorrelated background), (2) events in the "Off-window", normalized by the scale factor $k$ (i.e., high-statistics estimate of the uncorrelated background), (3) events obtained from the statistical subtraction of "On-window" and "Off-window" samples. Color code: black for all events (correlated + uncorrelated), red for background-only events, blue for $^{214}$Bi $\beta$-decay spectrum, green for $^{214}$Po $\alpha$-decay spectrum, and purple for the $\Delta t$ distribution resulting from subtraction. . . . . 49

4.6 Examples of the $\Delta t$, $\Delta R$, $E_{delayed}$, and $E_{prompt}$ distributions, with regions inside (blue) and outside (red) the cut thresholds highlighted. For a more detailed description of the method, refer to the main text. . . . . 50

4.7 Example fit of the $\Delta t$ distribution between correlated events. Shown are: the distribution of correlated + uncorrelated coincidences in the on-window region (black empty histogram), the uncorrelated background (red) with the fitted constant background term (green), and the statistically subtracted correlated component (purple). The fitted value of $\tau$ is consistent within $1\sigma$ with the expected value ($\tau_{^{214}Po} = 237\,\mu s$). . . . . 51

4.8 **Top:** Time evolution of BiPo activity (in mBq/$m^3$) during the considered period. Runs with filling paused are shown in blue, while those with active filling of new LS are shown in green. The inset highlights the activity trend during a filling stop longer than 5 days, used to estimate the $^{238}$U concentration. **Bottom:** Volume of LS in the CD over time in $m^3$. The slope during commissioning periods corresponds to the filling rate $v = 7\,m^3/h$. . . . . 52
4.9 Fit of BiPo activity between May 13 and May 19 (during an LS filling pause). . . . . 53
4.10 $\chi^2$ distribution for the variable $C_{\text{not fixed}}$, with the $1\sigma$ region highlighted. . . . . 54
4.11 Posterior distribution of $C_{^{238}U}^{\tau_{^{222}Rn}^{\text{not fixed}}}$ , with 68%, 95%, and 99.7% credibility intervals highlighted. . . . . 55
4.12 Total charge distribution for events tagged as spallation neutrons. In black: the total charge histogram; in red: the exponential plus Gaussian fit. . . . . 56
4.13 Calibrated energy distribution for events tagged as spallation neutrons. In black: the total charge histogram; in red: the exponential plus Gaussian fit. . . . . 57

5.1 Diagram of signal propagation in JUNO, highlighting the different processes and variables involved. For a detailed explanation of each stage, see the main text. . . . . 60
5.2 Vertex reconstruction using the CCM without bias correction, for a run with an AmBe source placed at $V = (x, y, z) = (0, 0, 10.5)$ (indicated by the black dashed line and a star-shaped marker). The water-LS interface level is shown in green. . . . . 64
5.3 Vertex reconstruction using the CCM with bias correction ($a = 1.75$) for a run with an AmBe source at $V = (x, y, z) = (0, 0, 10.5)$ (indicated by the black dashed line and a star-shaped marker). The water-LS interface is shown in green. . . . . 65
5.4 Experimental hit time distribution for a single event. In gray: all PMTs; in light blue and green: only PMTs in water and in LS, respectively. . . . . 65
5.5 Hit times split by propagation phase: yellow (scintillation hits with red PDF), green (after adding ToF offset), and blue (after convolution with PMT response). . . . . 66
5.6 Reconstructed hit time distribution for a single event. Red: all PMTs; light blue and green: PMTs in water and in LS, respectively. . . . . 67
5.7 Comparison of experimental (histograms) and reconstructed (continuous lines) hit time distributions for a single event. . . . . 67
5.8 $\chi^2$ distribution for the three reconstructed vertex coordinates. The $1\sigma$ region is shown in blue, the best fit in red, and the true vertex in black. . . . . 68
5.9 Bidimensional distribution in linear scale on the (x,z) and (y,z) planes of reconstructed vertices from a laser run with theoretical vertex (black dashed lines) at the center of the detector. The green line represents the Water-LS interface level. . . . . 68
5.10 Bidimensional distribution in logarithmic scale with zoom around the true vertex, in the (x,z) and (y,z) planes of reconstructed vertices from a laser run with theoretical vertex (black dashed lines) at the detector center. The green line indicates the Water-LS interface. . . . . 69

5.11 Distribution of the difference between reconstructed and true vertices for a laser run, with a Gaussian fit with constant background overlaid to estimate the centroid $\mu$ (displacement from the true value) and $\sigma$ (an indicator of the reconstruction resolution). . 69
5.12 Distributions of $\mu$ (displacement from the true value) and $\sigma$ (indicator of reconstruction resolution) for AmBe runs at various $z$ positions, with constant $(x, y) = (0, 0)$. . . . . 70
5.13 Non-uniformity map showing the trend of LY (in number of photoelectrons per MeV of deposited energy) as a function of the radial distance $R$ from the center of the detector. 72
5.14 Calibrated energy spectrum of spallation neutrons before (red) and after (blue) applying the correction from the non-uniformity map. Gaussian fits are superimposed to both spectra to estimate the energy resolution. . . . . 72

B.1 Energy spectra of solar neutrinos from the pp chain (solid lines) and CNO cycle (dashed lines). The flux (vertical scale) is given in units of $cm^{-2}s^{-1}MeV^{-1}$ for continuum sources and $cm^{-2}s^{-1}$ for monoenergetic sources. Parentheses indicate the corresponding relative uncertainties of the SSM predictions. . . . . 81
B.2 Contributions from all neutrino and background species considered for the sensitivity analysis of six years of data taking in the baseline radiopurity scenario. Solar neutrino contributions are shown as solid lines respectively, while background contributions appear as dotted lines. . . . . 83

# List of Tables

1.1 Summary of reactor neutrino experiments. . . . . 7

2.1 Summary of the thermal power and baseline to the JUNO detector for the Yangjiang (YJ) and Taishan (TS) reactor cores, as well as the remote reactors of Daya Bay (DYB) and Huizhou (HZ). Taken from [7]. . . . . 10

2.2 A baseline plan of a comprehensive/weekly/monthly calibration (adapted from [20]). 18

3.1 Comparative analysis of nonlinear system solution methods, highlighting computational characteristics and convergence properties. . . . . 32

4.1 Expected background rates, background to signal ratio (B/S), and rate and shape uncertainties. . . . . 44

# References


[1] P. Zyla et al. “Particle Data Group”. In: *Review of Particle Physics, PTEP, 083C01* (2020).

[2] B. Potecorvo. “Neutrino Experiments and the Problem of Conservation of Leptonic Charge”. In: *Zh.Eksp.Teor.Fiz. 53* (1967).

[3] V. N. Gribov and B. Pontecorvo. “Neutrino astronomy and lepton charge”. In: *Phys.Lett.B 28 493* (1969).

[4] De Salas P. et al. “Status of neutrino oscillations 2018: 3 $\sigma$ hint for normal mass ordering and improved CP sensitivity.” In: *Phys. Lett. B782, 633–640* (2018).

[5] S. T. Petcov and M. Piai. “The LMA MSW Solution of the Solar Neutrino Problem, Inverted Neutrino Mass Hierarchy and Reactor Neutrino Experiments”. In: *Phys. Lett. B 533 94–106* (2002).

[6] Mena O. and Parke S. J. “Unified graphical summary of neutrino mixing parameters”. In: *Phys. Rev. D 69:117301* (2004).

[7] A. Abusleme et al. (JUNO Collaboration). “JUNO physics and detector”. In: *Progress in Particle and Nuclear Physics 123 103927* (2022).

[8] A. Giaz et al. “Status and perspectives of the JUNO experiment”. In: *arXiv:1804.03575v1* (2018).

[9] T. Adam et al. “The OPERA experiment Target Tracker”. In: *Nuclear Instruments and Methods in Physics Research A 577 523–539* (2007).

[10] A. Abusleme et al. “The JUNO experiment Top Tracker”. In: *Nucl. Instr. Meth. A 1057 168 680* (2023).

[11] A. Abusleme et al. (JUNO Collaboration). “Optimization of the JUNO liquid scintillator composition using a Daya Bay antineutrino detector”. In: *Nuclear Inst. and Methods in Physics Research, A 988 164823* (2021).

[12] A. Abusleme et al. “The design and sensitivity of JUNO’s scintillator radiopurity sub-detector OSIRIS”. In: *Eur. Phys. J. C81 973* (2021).

[13] A. Abusleme et al. “Mass testing and characterization of 20-inch PMTs for JUNO”. In: *Eur. Phys. J. C82 1168* (2022).

[14] H. Hertz. “Ueber einen Einfluss des ultravioletten Lichtes auf die electrische Entladung”. In: *Annalen der Physik 267.8, pp. 983–1000* (1887).

[15] C. Genster. “Software and hardware development for the next-generation liquid scintillator detectors JUNO and OSIRIS”. PhD thesis. RWTH Aachen University, 2019.

[16] Filippo Marini. "Development and Testing of the large PMTs Front-End Electronics for the JUNO Experiment". PhD thesis. University of Padova, 2021.

[17] V. Cerrone et al. "Validation and integration tests of the JUNO 20-inch PMT readout electronics". In: *Nucl. Instr. Meth. A1053 168322* (2023).

[18] A. Coppi et al. "Mass testing of the JUNO experiment 20-inch PMT readout electronics". In: *Nuclear Inst. and Methods in Physics Research, A 1052 168255* (2023).

[19] C. Liu et al. "Check on the features of potted 20-inch PMTs with 1F3 electronics prototype at Pan-Asia". In: *JINST18 P02003* (2023).

[20] A. Abusleme et al. (JUNO collaboration). "Calibration Strategy of the JUNO Experiment". In: *arXiv:2011.06405 [physics.ins-det]* (2021).

[21] Feiyang Zhang et al. "The background of the JUNO calibration system". In: *Manuscript in preparation* (.).

[22] J. Liu et al. "Neutron Calibration Sources in the Daya Bay Experiment". In: *Nucl. Instrum. Meth. A 750 19.* (2014).

[23] Igor Ostrovskiy et al. "Double Chooz Calibration". In: *Nuclear Physics B (Proc. Suppl.) 229-232 431* (2012).

[24] Jeremy S. Cushman et al. "First results from the CUORE experiment". In: *Nucl. Instrum. Meth. A 844 32-44* (2017).

[25] Yuhang Guo et al. "Design of the Guide Tube Calibration System for the JUNO experiment". In: *JINST 14 T09005* (2019).

[26] J. Boger et al. "The Sudbury neutrino observatory". In: *Nucl. Instrum. Meth. A 449 172-207* (2000).

[27] B E Berger el al. (KamLAND Collaboration). "The KamLAND full-volume calibration system". In: *JINST 4 P04017* (2009).

[28] B. Caccianiga and A. C. Re. "The calibration system for the Borexino experiment". In: *Int. J. Mod. Phys. A 29 1442010* (2014).

[29] K. Feng et al. "A novel remotely operated vehicle as the calibration system in JUNO". In: *JINST 13 T12001* (2018).

[30] J. F. Amsbaugh et al. "An array of low-background 3He proportional counters for the Sudbury Neutrino Observatory". In: *Nucl. Instrum. Meth. A 579 1054-1080* (2007).

[31] G. L. Zhu et al. "Ultrasonic positioning system for the calibration of central detector". In: *Nucl. Sci. Tech. 30 5.* (2019).

[32] D.S. Ayres et al. (NOvA collaboration). "NOvA Proposal to Build a 30 Kiloton Off-Axis Detector to Study Neutrino Oscillations in the Fermilab NuMI Beamline". In: *arXiv:hep-ex/0503053* (2004).

[33] C. Adams et al. (LBNE Collaboration). "Snowmass 2013: Workshop on Energy Frontier". In: *arXiv:1307.7335* (2013).

[34] S. Ahmed et al. (ICAL Collaboration). "Physics Potential of the ICAL detector at the India-based Neutrino Observatory (INO)". In: *arXiv:1505.07380* (2017).

[35] M. Aartsen et al. (IceCube PINGU Collaboration). "Letter of intent: The precision IceCube next generation upgrade (PINGU)". In: *arXiv:1401.2046* (2014).

[36] V. Van Elewyck (KM3NeT collaboration). "ORCA: measuring the neutrino mass hierarchy with atmospheric neutrinos in the Mediterranean". In: *J. Phys. Conf. Ser. 598 (1) 012033* (2015).

[37] K. Abe et al. (Hyper-K Collaboration). "Letter of intent: The hyper-Kamiokande experiment — Detector design and physics potential". In: *arXiv:1109.3262* (2011).

[38] A. Abusleme et al. (JUNO Collaboration). "Sub-percent precision measurement of neutrino oscillation parameters with JUNO". In: *Chinese Phys. C 46 123001* (2022).

[39] F. An et al. "Neutrino Physics with JUNO". In: *Phys. G: Nucl. Part. Phys. 44 030401* (2016).

[40] A. Abusleme et al. (JUNO Collaboration). "Potential to identify neutrino mass ordering with reactor antineutrinos at JUNO". In: *arXiv:2405.18008v2 [hep-ex]* (2025).

[41] M Blennow and T. Schwetz. "Determination of the neutrino mass ordering by combining PINGU and Daya Bay II". In: *J. High Energy Phys. 09 089* (2013).

[42] M. Lipinski et al. "White rabbit: a PTP application for robust sub-nanosecond synchronization". In: *2011 IEEE International Symposium on Precision Clock Synchronization for Measurement, Control and Communication. DOI: 10.1109/ISPCS.2011.6070148* (2011).

[43] "IEEE Standard for a Precision Clock Synchronization Protocol for Networked Measurement and Control Systems". In: *IEEE Std 1588-2008 (Revision of IEEE Std 1588-2002), pp. 1–269. DOI: 10.1109/IEEESTD.2008.4579760.* (2008).

[44] D. Pedretti et al. "Nanoseconds Timing System Based on IEEE 1588 FPGA Implementation". In: *IEEE TRANSACTIONS ON NUCLEAR SCIENCE, VOL. 66, NO. 7,* (2019).

[45] *Principles and Applications of Timing Spectroscopy*. ORTEC.

[46] J. D. Faires R. L. Burden. *Numerical Analysis*. CENGAGE Learning, 2010.

[47] K. Levenberg. "A method for the solution of certain non-linear problems in least squares". In: Brown University, 1944. Chap. pp. 164-168.

[48] D. W. Marquardt. "An Algorithm for Least-Squares Estimation of Nonlinear Parameters". In: Society for Industrial and Applied Mathematics, 1963. Chap. pp. 431-441.

[49] C. G. Broyden. "A Class of Methods for Solving Nonlinear Simultaneous Equations". In: American Mathematical Society, 1965. Chap. pp. 577-593.

[50] H. S. Zhang et al. "Refractive index in the JUNO liquid scintillator". In: *Nuclear Inst. and Methods in Physics Research, A* (2024).

[51] Y. Zhang et al. "Laser calibration system in JUNO". In: *JINST 14 P01009* (2019).

[52] *Photomultiplier Tubes, principles and applications*.

[53] F. Kaether and C. Langbrandtner. "Transit Time and Charge Correlations of Single Photoelectron Events in R7081 Photomultiplier Tubes". In: *arXiv:1207.0378v2* (2012).

[54] V. Cerrone. "Probing the atmospheric mass splitting $\Delta m^2_{31}$ with reactor antineutrino oscillations at JUNO". In: *Master Thesis, University of Padova* (2023).

[55] J. Cheng et al. "Neutral-current background induced by atmospheric neutrinos at large liquid-scintillator detectors: I. model predictions". In: *Phys. Rev. D 103, 053001, arXiv:2008.04633.* (2021).

[56] J. Cheng et al. "Neutral-current background induced by atmospheric neutrinos at large liquid-scintillator detectors: III. Quantitative calculations for reactor neutrinos". In: *arXiv:2404.07429.* (2024).

[57] A. Abusleme et al. (JUNO Collaboration). "Radioactivity control strategy for the JUNO detector". In: *JHEP11 102* (2021).

[58] A. Abusleme et al. "Prediction of Energy Resolution in the JUNO experiment". In: *arXiv:2405.17860v2* (2025).

[59] B. Valeur and M. N. Berberan-Santos. "Molecular Fluorescence: Principles and Applications". In: *John Wiley & Sons, Ltd, chap. 8, pp. 213–261* (2012).

[60] J. B. Birks. "The theory and practice of scintillation counting". In: (1964).

[61] J. B. Birks. "Scintillations from Organic Crystals: Specific Fluorescence and Relative Response to Different Radiations". In: *Proc. Phys. Soc. A 64, 874* (1951).

[62] I. M. Frank and I. E. Tamm. "Coherent visible radiation of fast electrons passing through matter". In: *Compt. Rend. Acad. Sci. URSS 14, 109* (1937).

[63] Q. Liu et al. "A vertex reconstruction algorithm in the central detector of JUNO". In: *arXiv:1803.09394v3 [physics.ins-det]* (2018).

[64] L. V. D'Auria. "Commissioning of the JUNO sub-detector OSIRIS readout electronics". In: *Bachelor Thesis, University of Padova* (2023).

[65] Zi Yuan et al. "Event vertex and time reconstruction in large-volume liquid scintillator detector". In: *Nucl Sci Tech 32 49* (2021).

[66] M. Beretta et al. "Fluorescence emission of the JUNO liquid scintillator". In: *arXiv:2501.09988v4 [physics.ins-det]* (2025).

[67] L. Ludhova et al. "Particle Identification at MeV Energies in JUNO". In: *arXiv:2007.02687v3 [physics.ins-det]* (2020).

[68] F. James. "MINUIT Function Minimization and Error Analysis". In: *Reference Manual Version 94 1* (1994).

[69] A. Gavrikov et al. "Interpretable machine learning approach for electron antineutrino selection in a large liquid scintillator detector". In: *Phys. Lett. B 860 139141* (2025).

[70] A. Abusleme et al. (JUNO Collaboration). "The Design and Technology Development of the JUNO Central Detector". In: *arXiv:2311.17314v2* (2024).

[71] A. Sturmia and F. Vissani. "Precise quasielastic neutrino/nucleon cross section". In: *arXiv:astro-ph/0302055v2* (2003).

[72] Timo van Ritbergen and Robin G. Stuart. "On the precise determination of the Fermi coupling constant from the muon lifetime". In: *Nuclear Physics B 564. 343–390* (2000).

[73] V. Cirigliano et al. "Status of Vus and Vud". In: *Proceedings of the first CKM workshop, CERN.* (2002).

[74] C.H. Llewellyn-Smith. "Neutrino reactions at accelerator energies". In: *Phys. Rept. 3 261* (1972).

[75] S. Towner. "Radiative corrections in neutrino-deuterium scattering". In: *hys. Rev. C 58 1288* (1998).

[76] A. Kurylov, M.J. Ramsey-Musolf, and P. Vogel. "Radiative corrections to low energy neutrino reactions". In: *hep- ph/0211306* (2002).

[77] A. Abusleme et al. "JUNO sensitivity to 7Be, pep, and CNO solar neutrinos". In: *arXiv:2303.03910v1 [hep-ex]* (2023).

[78] E. Caffau et al. "Solar Chemical Abundances Determined with a CO5BOLD 3D Model Atmosphere". In: *Solar Physics 268 255.* (2010).

[79] M. Asplund et al. "The Chemical Composition of the Sun". In: *Annu. Rev. Astron. Astrophys. 47 481.* (2009).

[80] E. Magg et al. "Observational constraints on the origin of the elements - IV. Standard composition of the Sun". In: *Astron. Astrophys. 661 A140.* (2022).

[81] N. Grevesse and A. Sauval. "Standard Solar Composition". In: *Space Science Reviews 85 161.* (1998).

[82] L. Wolfenstein. "Neutrino oscillations in matter". In: *Phys. Rev. D 17 2369.* (1978).

[83] S.P. Mikheyev and A.Y. Smirnov. "Resonance Amplification of Oscillations in Matter and Spectroscopy of Solar Neutrinos". In: *Sov. J. Nucl. Phys. 42 913.* (1985).

[84] I. Esteban et al. "Updated fit to three neutrino mixing: exploring the accelerator-reactor complementarity". In: *J. High Energ. Phys. 01 087* (2017).

[85] P. de Holanda, W. Liao, and A. Smirnov. "Toward precision measurements in solar neutrinos". In: *Nuclear Physics B 702 307–332.* (2004).

[86] Borexino collaboration. "Comprehensive measurement of pp-chain solar neutrinos". In: *Nature 562 505.* (2018).

[87] Borexino collaboration. "Experimental evidence of neutrinos produced in the CNO fusion cycle in the Sun". In: *Nature 587 577.* (2020).

[88] Borexino collaboration. "Final results of Borexino Phase-I on low energy solar neutrino spectroscopy". In: *Phys. Rev. D 89 112007* (2014).

[89] K. S. Krane. *Introductory Nuclear Physics*. John Wiley & Sons, 1988.

[90] H. Bateman. *The solution of a system of differential equations occurring in the theory of radioactive transformations*. Proc. Cambridge Philos. Soc (Vol. 15, No. pt V, pp. 423–427, 1910.